

Atomic Hydrogen Gas in Dark-Matter Minihalos and the Compact High Velocity Clouds

Amiel Sternberg

*School of Physics and Astronomy and the Wise Observatory, The Beverly and Raymond Sackler Faculty of Exact Sciences, Tel Aviv University, Tel Aviv 69978, Israel;
amiel@wise.tau.ac.il*

Christopher F. McKee

Physics Department, and Astronomy Department, University of California at Berkeley, Berkeley, CA 94720

and

Mark G. Wolfire

Astronomy Department, University of Maryland, College Park, MD 20742

ABSTRACT

We calculate the coupled hydrostatic and ionization structures of spherically symmetric, pressure-supported gas clouds that are confined by gravitationally dominant dark-matter (DM) mini-halos and by an external bounding pressure provided by a hot medium. We focus on clouds that are photoionized and heated by the present-day background metagalactic field and determine the conditions for the formation of warm (WNM), and multi-phased (CNM/WNM) neutral atomic hydrogen (HI) cores in the DM-dominated clouds.

We consider Λ CDM dark-matter halos with cuspy (NFW) and constant density (Burkert) cores. We compute models for a wide range of halo masses, total cloud gas masses, and external bounding pressures.

We present models for the pressure-supported HI structures observed in the Local Group dwarf irregular galaxies Leo A and Sag DIG. We find that the hydrogen gas becomes neutral for projected HI column densities exceeding 10^{19} cm^{-2} . We identify the HI cloud boundaries observed in Leo A and Sag DIG with the ionization fronts, and we derive an upper limit of $P_{\text{HIM}}/k \lesssim 100 \text{ cm}^{-3} \text{ K}$ for the ambient pressure of the intergalactic medium in the Local Group. The observed HI gas scale heights in Leo A and Sag DIG imply characteristic DM densities of

1.2 amu cm^{-3} (or $0.03M_{\odot} \text{ pc}^{-3}$), consistent with the DM densities previously inferred via HI rotation curve studies of dwarf and low-surface brightness galaxies. Leo A and Sag DIG obey the scaling correlations that are expected for typical (median) DM halos in a Λ CDM cosmology, provided the halos contain constant density cores, as suggested by Burkert.

We construct explicit “mini-halo” models for the multi-phased (and low-metallicity) compact high-velocity HI clouds (CHVCs). If the CHVC halos are drawn from the same family of halos that successfully reproduce the dwarf galaxy observations, then the CHVCs must be “circumgalactic” objects, with characteristic distances of 150 kpc. For such systems we find that multi-phased behavior occurs for peak WNM HI column densities between 2×10^{19} and $1 \times 10^{20} \text{ cm}^{-2}$, consistent with observations. In contrast, if the CHVCs are “extragalactic” objects with distances $\gtrsim 750$ kpc, then their associated halos must be very “underconcentrated”, with characteristic DM densities $\lesssim 0.08 \text{ cm}^{-3}$, much smaller than expected for their mass, and significantly smaller than observed in the dwarf galaxies. Furthermore, multi-phased cores then require higher shielding columns. We favor the circumgalactic hypothesis. If the large population of CHVCs represent “missing low-mass DM satellites” of the Galaxy, then these HI clouds must be pressure-confined to keep the gas neutral. For an implied CHVC mini-halo scale velocity of $v_s = 12 \text{ km s}^{-1}$, the confining pressure must exceed $\sim 50 \text{ cm}^{-3} \text{ K}$. A hot ($\sim 2 \times 10^6 \text{ K}$) Galactic corona could provide the required pressure at 150 kpc.

Our static mini-halo models are able to account for many properties of the CHVCs, including their observed peak HI columns, core sizes, and multi-phased behavior. However, important difficulties remain, including the presence in some objects of extended low column density HI wings, and $\text{H}\alpha$ emission line fluxes in several CHVCs that are significantly larger than expected.

Subject headings: Galaxy: general, formation, evolution – Galaxies: Local Group – ISM: high velocity clouds, intergalactic medium – Cosmology: dark matter

1. Introduction

High velocity clouds (HVCs) are atomic hydrogen (HI) clouds with radial velocities inconsistent with gas in differential circular rotation in the Galactic disk. Since their discovery via 21 cm observations by Muller, Oort & Raimond (1963) the HVCs have been observed, surveyed, and catalogued in ever increasing detail (Bajaja et al. 1987; Hulsbosch & Wakker

1988; Wakker & van Woerden 1991; Hartmann & Burton 1997; Braun & Burton 2000; Brüns et al. 2000; Burton, Braun & Chengalur 2001; Putman et al. 2002; Lockman et al. 2002; de Heij, Braun & Burton 2002a). However, the nature and origin of the HVCs have remained the subject of considerable and unresolved debate (Oort 1966; Wakker & van Woerden 1997; Blitz et al. 1999; Wakker, van Woerden & Gibson 1999; Gibson et al. 2002; Sembach 2002).

The HVCs consist of several hundred compact, kinematically distinct, clouds with typical angular diameters of $\sim 1 - 2^\circ$ (Braun & Burton 2000; Putman et al. 2002), as well as several large (diffuse) and kinematically continuous complexes (e.g., the “A, B, C, H, & M” clouds) that extend over ~ 100 square degrees. The HVCs appear to be devoid of any stellar counterparts. The radial velocities of the HVCs identified in the Wakker & van Woerden (1991) catalogue range from -464 to $+297$ km s^{-1} relative to the local standard of rest. de Heij, Braun & Burton (2002b) identified 67 distinct compact high velocity clouds (CHVCs) in the single-dish “Leiden/Dwingeloo” HI survey (Hartmann & Burton 1997). Putman et al. (2002) identified an additional 179 CHVCs in the (more sensitive) southern-hemisphere “HI Parkes All Sky Survey” (HIPASS). Most of the CHVCs are infalling. The “Leiden/Dwingeloo” survey, carried out with angular and velocity resolutions of 0.5 and 1 km s^{-1} respectively, shows that the typical (one-dimensional) velocity dispersions of the CHVCs are ~ 14 km s^{-1} with little scatter about this value (Blitz et al. 1999). The velocity dispersions imply gas temperatures $\sim 10^4$ K, consistent with a warm medium (WM) possibly consisting of a mixture of a warm neutral (WNM) and ionized (WIM) gas. Typically, $N_{\text{HI}} \sim 5 \times 10^{18}$ cm^{-2} averaged over the extents of the CHVCs. However, the CHVCs are barely resolved with the (25-meter) Dwingeloo and (64-meter) Parkes telescopes. More recently Burton et al. (2001) were able to resolve the spatial structures of ten CHVCs in higher resolution (3.5×3.7 arcmin) observations with the (305-meter) Arecibo telescope. They found that the typical observed (projected) $1/e$ exponential scale-lengths of the HI distributions equal 690 arcsec, with central HI columns ranging from 2×10^{19} to 2×10^{20} cm^{-2} . In some objects, gas was detected out to $\sim 1^\circ$ from the cloud centers down to column densities of $\sim 2 \times 10^{17}$ cm^{-2} . The line widths are slightly narrower in the Arecibo data set compared to the Leiden/Dwingeloo observations, with corresponding velocity dispersions of ~ 11 km s^{-1} . The velocity gradients across the clouds are relatively small, ~ 10 km s^{-1} degree^{-1} , and the WNM cloud dynamics are controlled primarily by thermal motions.

In another important development Braun & Burton (2000) and de Heij, Braun & Burton (2002c) carried out high resolution Westerbork interferometric observations (with ~ 1 arcmin synthesized beams) and found that at least some CHVCs contain high column density (up to $\sim 10^{21}$ cm^{-2}) cores, with typical radii ~ 10 arcmin, and line profiles as narrow as 2 km s^{-1} . The narrow line widths imply HI gas in a cold neutral medium (CNM; $T \lesssim 100$ K). Previous to this work CNM cores were known to exist only in the extended A, H, and M complexes

(Wakker & Schwarz 1991). The recent single-dish and interferometric observations reveal that “core/envelope” CNM/WNM structures may be a common feature of the CHVCs.

The distance is the critical unknown for the HVCs. The large complexes are plausibly nearby objects, and stellar absorption-line observations in the large M and A clouds (Danly, Albert & Kuntz 1993; van Woerden et al. 1999) constrain their distances to within 5 and 10 kpc respectively. However, no direct distance determinations are yet available for the large population of CHVCs.

Many theories for the origin of the HVCs have been proposed over the years (Wakker & van Woerden 1997). Oort (e.g. 1966; 1970) recognized that if the HVCs are gravitationally bound objects with masses dominated mainly by the observed HI gas they must be distant, with distances $d \gtrsim \Delta v^2 f / \pi G m_{\text{H}} N_{\text{HI}} \theta$, where Δv is the observed velocity dispersion, N_{HI} is the mean HI column within angular radius θ , and f is the fraction of the total dynamical mass present as HI gas. If the clouds are bound, then the required value of f is proportional to the assumed distance d , since the HI mass varies as d^2 , whereas the dynamical mass $M_{\text{dyn}} \equiv \Delta v^2 d \theta / G \propto d$. For $f = 1$ the observations imply implausibly large “binding distances” $d \gtrsim 10$ Mpc, and HI masses $M_{\text{HI}} \equiv \pi d^2 \theta^2 m_{\text{H}} N_{\text{HI}} \gtrsim 10^9 M_{\odot}$. Oort’s preferred interpretation was that the HVCs are transient “circumgalactic” ($\lesssim 100$ kpc) primordial gas clouds that have recently condensed out of the intergalactic medium, and are only now being accreted onto the disk in the end-stages of the Galaxy formation process. Shapiro & Field (1976) introduced the idea of the Galactic fountain (see also Bregman 1996) in which hot gas ejected from the disk cools and condenses into neutral clouds that fall back onto the Galaxy in a continuing cycle. Giovanelli (1981) suggested that the HVCs are scattered fragments of the Magellanic Stream.¹ A Local Group² (LG) origin for the HVCs was also proposed and discussed by various authors in the years immediately following their discovery (Oort 1966; Verschuur 1969; Einasto et al. 1974; Eichler 1976). In this picture the HVCs are genuine extragalactic objects associated with the LG system, and are at typical distances of ~ 1

¹The “Magellanic Stream” (Mathewson, Cleary & Murray 1974) is an example of extended HVC gas that is relatively well understood. It consists of a narrow trail of HI gas that emanates from the Magellanic Clouds, and stretches over 100° across the sky. The stream is almost certainly gas that has been tidally (Gardiner & Noguchi 1996) or ram-pressure stripped (Moore & Davis 1994) from the Magellanic Clouds as these satellite galaxies orbit the Milky Way.

²We recall that the LG is a dynamically bound system of galaxies consisting of the Milky Way and its two largest neighbors M31 and M33, and 40 or more smaller and fainter dwarf galaxies (Mateo 1998). The LG is typical of the many small groups and clusters of galaxies situated along the outer boundary of the Virgo supercluster (van den Bergh 1999). The LG radius defined as the zero-velocity surface relative to the Hubble flow is ~ 1.5 Mpc, and the characteristic velocity dispersion is ~ 60 km s⁻¹ (Sandage 1986). The mass of the LG is dominated by the Milky Way and M31, and equals about $3.3 \times 10^{12} M_{\odot}$.

Mpc, rather than being a structural feature of the Galaxy and its immediate surroundings.

The distances to the clouds may be constrained via observations of optical H α recombination line emission that provides a measure of the ionizing radiation field incident on the clouds (Weiner & Williams 1996; Bland-Hawthorn et al. 1998; Tufte et al. 1998; Weiner, Vogel & Williams 2001). At sufficiently large distances from the Galaxy, the dominant radiation field becomes the weak metagalactic background and the clouds should be weak H α emitters. Nearby clouds might be ionized by more intense “leakage radiation” from the Galactic disk, and could be more intense H α sources. Sensitive optical Fabry-Perot H α observations have been reported and compiled by Weiner et al. (2001) for several HVC complexes and one isolated CHVC. Tufte et al. (2002) have reported H α observations in five CHVCs. For the complexes Weiner et al. find that the measured H α surface brightnesses range from 41 to 1680 milli-Rayleighs³ (mR), implying photoionizing Lyman continuum (Lyc) intensities of 1.5×10^4 to 6.0×10^5 photons cm⁻² s⁻¹ sr⁻¹. Weiner et al. detected an H α intensity of 48 mR in CHVC 230+61+165 (an object included in the Burton et al. [2001] Arecibo data set). Tufte et al. (2002) report H α intensities in the range of 20 to 140 mR in four CHVCs, and an upper limit of 20 mR in an additional CHVC. The detected fluxes are larger than the (2σ) upper limit of 20 mR set by Vogel et al. (1995) for the H α intensity of the isolated extragalactic Giovanelli & Haynes (1989) cloud that Vogel et al. argue is probing the metagalactic field (see also Madsen et al. 2001; Weymann et al. 2001). Tufte et al. argue that the relatively large CHVC H α fluxes imply that the CHVCs are located within the Galactic halo. However, the distance estimates are uncertain due to uncertainties in the actual strength of the metagalactic field, the Galactic radiation escape fraction, and the role of collisional ionization.

The metallicity and dust content are additional potentially important clues to the origin of the HVCs. Thermal ($\sim 100 \mu\text{m}$) emission signatures of dust grains have been searched for but not detected (Wakker & Boulanger 1986). However, a few metallicity measurements are available, mainly via ultraviolet absorption line studies toward background quasars and Seyfert galaxies. Significantly subsolar (though not purely primordial) metal abundances are indicated, primarily via observations of gas phase sulfur⁴. Low metallicities would appear to be inconsistent with a Galactic fountain, and favor models in which the gas originates

³1 Rayleigh = $10^6/4\pi$ photons cm⁻² s⁻¹ sr⁻¹. For case-B recombination at a temperature of 10^4 K, a surface brightness of 1 Rayleigh is produced by a slab with emission measure $EM = 2.8 \text{ cm}^{-6} \text{ pc}$, which for two-sided illumination in ionization equilibrium, is produced by a Lyman continuum photon intensity $J^* = 3.6 \times 10^5$ photons cm⁻² s⁻¹ sr⁻¹.

⁴Sulfur is generally considered to be robust probe of the intrinsic metallicity since S remains undepleted in diffuse gas (Jenkins et al. 1987).

outside the Galaxy. Lu et al. (1998) observed HVC 287+22+240 using the Goddard High Resolution Spectrograph (GHRS) on board *Hubble Space Telescope* (HST) and detected several SII and FeII absorption lines. Lu et al. derived $S/H=0.25\pm 0.07$, $Fe/H=0.033\pm 0.006$, and $S/Fe=7.6\pm 2.2$ (relative to solar abundances). They interpreted the supersolar S/Fe ratio as being due to significant iron depletion and therefore evidence for the presence of dust grains. In view of similar abundances observed in the Magellanic Clouds, as well as the proximity of 287+22+240 to these objects, Lu et al. concluded that this HVC is a “leading arm” component of the Magellanic stream. Wakker et al. (1999) carried out GHRS spectroscopy of HVC gas in complex C and inferred $S/H=0.089\pm 0.024$. They favor the Oort hypothesis, and interpret complex C as infalling primordial gas that has been “contaminated” by metals as it interacts with the Galactic halo. Braun & Burton (2000) derived a similar low metallicity for one of the CHVCs in their sample (125+41-207). They combined their HI observations together with MgII absorption measurements reported by Bowen & Blades (1993), and inferred a Mg/H abundance in the range of 0.04 to 0.07 relative to solar.

Recently, Murphy et al. (2000) and Sembach et al. (2000) carried out *Far Ultraviolet Spectroscopic Explorer* (FUSE) absorption-line studies of several HVCs. In complex C Murphy et al. found $Fe/H \sim 0.5$ (relative to solar) that may indicate undepleted iron and hence a very low dust content. Sembach et al. (2002) set a metallicity limit of $O/H < 0.46$ in CHVC 224-83-197 via the detection of OI absorption. An important result of the FUSE observations was the detection of OVI absorption tracing highly ionized gas in several HVCs. These observations complement earlier GHRS observations of CIV, SiIV and NV absorption in high velocity gas that Sembach et al. (1999) suggested is produced in the ionized envelopes of neutral hydrogen HVCs (as the ionized clouds do not appear to be 21 cm sources). Sembach et al. (1999) argued that the observed C^{+3} , Si^{+3} and N^{+4} abundances are consistent with low pressure ($P/k \sim 2 \text{ cm}^{-3} \text{ K}$) gas photoionized by an assumed Lyc flux at a level plausibly consistent with the metagalactic background. They concluded that the CIV, SiIV and NV absorbers are located at large distances and are Local Group objects. The OVI abundances are too large to be compatible with photoionization, and may be produced collisionally at the interfaces between the HVCs and a tenuous Galactic corona or Local Group medium through which they are moving (Sembach et al. 2000). We note that collisional ionization (in gas with pressures considerably larger than $2 \text{ cm}^{-3} \text{ K}$) may also contribute to the production of the C^{+3} , Si^{+3} and N^{+4} ions.

Evidence of an ambient medium in which the CHVCs may be embedded could also provide clues to their origin. Brüns, Kerp & Pagels (2001) mapped one of the CHVCs (125+41-207) in the Burton et al. sample with the 100m Effelsberg telescope. They found that the WNM component is asymmetric with a “cometary” appearance. The head-tail morphology suggests that gas is being stripped off of the main body of the cloud as it moves

through an enveloping medium.

The Local Group hypothesis for the HVCs, particularly the CHVCs, has received renewed interest recently for additional observational and theoretical reasons. Bajaja et al. (1987) noted that asymmetries in the “position-velocity” diagram of the HVC ensemble could be understood if the HVCs are moving within the LG as a whole. More recently Blitz et al. (1999) and Braun & Burton (1999) demonstrated that the dispersion in CHVC velocities is minimized if the cloud velocities are measured relative to the LG barycenter (see however, Gibson et al. 2000). Furthermore, Blitz et al. presented a simulation of the LG dynamics that shows that “test particles” interacting with the Milky Way, M31, and the distant Virgo cluster, are (during a Hubble time) drawn into an elongated filamentary structure that reproduces the observed distribution and velocities of HVCs in the directions of the LG barycenter and anti-barycenter (see however Moore & Putman 2001; de Heij et al. 2002a). These kinematic considerations are strong evidence for a LG origin, although the cloud distances are not very well constrained. Blitz et al. concluded that the typical distances of the CHVCs are $d \gtrsim 750$ kpc. For $d = 750$ kpc, a characteristic radius of ~ 2.5 kpc and a central gas density of $\sim 6 \times 10^{-3} \text{ cm}^{-3}$ are implied by the Burton et al. (2001) observations. The HI mass in each cloud is $\sim 1 \times 10^7 M_\odot$, and the total HI mass in the system of CHVCs is $\gtrsim 10^9 M_\odot$. Such large masses may be in conflict with the apparent lack of similar objects around other galaxies and groups (Zwaan & Briggs 2000; Rosenberg & Schneider 2002). If the CHVCs are long-lived, gravitationally bound objects as conjectured by Blitz et al., then the measured velocity dispersions imply total dynamical masses $M_{\text{dyn}} \approx 5 \times 10^8 M_\odot$, comparable to dwarf galaxy masses. In this picture the HI mass is a fraction $f = 0.02$ of the total dynamical mass, and the 3.4 kpc radius corresponds to the “scale height” $\sim GM_{\text{dyn}}/\Delta v^2$ of the gravitationally confined gas. Blitz et al. suggested that the dynamical mass is dominated by dark-matter and that the CHVCs are tracing individual dark-matter “halos”.

The notion that the CHVCs represent dark-matter halos is motivated by the cosmological theory of hierarchical structure formation. In this theory, bound systems (“halos”) of non-baryonic, dark matter evolve in a hierarchical collapse, initiated by small gravitationally unstable primordial density fluctuations (Gunn & Gott 1972; Press & Schechter 1974; Blumenthal et al. 1984; Navarro, Frenk & White 1997; Bullock et al. 2001). Low-mass halos virialize first, and then merge into progressively more massive systems. Galaxies form as gas accumulates, cools, and collapses inside the virialized DM halos (White & Rees 1978). Detailed numerical simulations of the evolving collapse of dissipationless cold (non-relativistic) dark matter (CDM) have been carried out by several investigators (e.g. Navarro et al. 1997; hereafter NFW). The simulations predict the existence of many more low-mass halos than observed at the faint-end (i.e. dwarf galaxy scale) of the galaxy luminosity function. Various

suggestions have been made to account for this discrepancy, including: blow out of gas by winds and supernovae produced in small initial starbursts (Dekel & Silk 1986; Tegmark, Silk & Evrard 1993); photoionization heating of the baryonic component by the metagalactic radiation field, that inhibits the collapse of gas into the low-mass halos (Efstathiou 1992; Thoul & Weinberg 1996; Kepner, Babul & Spergel 1997; Kitayama & Ikeuchi 2000; Bullock Kravtsov & Weinberg 2000) and expulsion of gas trapped within the low-mass halos during the epoch of “reionization” (Barkana & Loeb 1999). In all of these scenarios the low-mass halos (or “mini-halos” as coined by Rees 1986) continue to exist, but because star-formation has been inhibited in them, they are not observable as galaxies.

In two recent studies, Klypin et al. (1999) and Moore et al. (1999) presented high-resolution simulations of the evolution of dark matter halos at the mass and size scales of the Milky Way and M31 galaxies that dominate the LG. They found that many low-mass sub-halos survive and continue to accrete into each of the dominating galaxy halos to the present day. In particular, the predicted number of low-mass satellite halos appears to exceed the number of observed satellite dwarf galaxies within ~ 300 kpc of the Milky Way. Klypin et al. suggested that the CHVCs are in fact the “missing DM satellites” that appear in their simulations. In this picture the CHVCs are “circumgalactic” mini-halos associated with the Milky Way, as opposed to “extragalactic” objects associated with the LG as proposed by Blitz et al. The presence of DM substructure may be detectable via the gravitational lensing of background quasars (Mao & Schneider 1998; Metcalf & Madau 2001; Dalal & Kochanek 2002).

The CNM/WNM structures observed in the CHVCs are in many ways similar to the multi-phased HI distributions observed in gas-rich dwarf irregular (dIrrs) galaxies ⁵. As summarized by Mateo et al. (1998), the observed HI masses in the dIrrs range from 0.1 to 0.5 of the total galaxy mass (including the dark matter). The HI gas is generally much more extended than the “Holmberg radii” (0.1–1 kpc) of the stellar components as traced in the optical. Young & Lo (1996; 1997) carried out detailed *Very Large Array* (VLA) interferometric studies of the dIrrs Leo A and Sag DIG and found that the observed HI line profiles can be separated into broad and narrow components. The broad (WNM) components appear as “envelopes” throughout the mapped regions of the galaxies, whereas the narrow (CNM) components are associated with small clumps or cores located near star-forming regions. The WNM envelopes appear to be pressure supported as opposed to rotationally supported. In these respects the HI structures in the dwarfs are similar to those observed in the CHVCs. However, there are important differences (in addition to the fact that star

⁵Blitz & Robishaw (2000) have recently shown that some dwarf spheroidals (dSphs) may also be gas-rich, with the gas being present at large offsets from the optical stellar light.

forming regions are absent in the CHVCs). First, the peak HI column densities of the WNM gas in the dwarfs (up to a few 10^{21} cm^{-2}) are significantly larger than in the CHVCs (up to $\sim 10^{20} \text{ cm}^{-2}$). Second, the angular scale sizes of the HI distributions are smaller in the dwarfs, ~ 70 arcsec in Sag DIG, and ~ 160 in Leo A, compared to the CHVCs where the characteristic size is ~ 690 arcsec. These facts will be important in our analysis of the CHVCs and dwarf galaxies as possibly related objects. Another key difference is that the distances to the dwarfs are well determined (via stellar photometry) whereas the distances to the CHVCs are unknown.

In this paper we quantitatively examine the hypothesis that the CHVCs are stable HI clouds confined by the gravitational potentials of dark-matter halos. We wish to determine whether viable “mini-halo” models for the CHVCs can be constructed as either “circumgalactic” ($d \sim 100$ kpc) or “extragalactic” ($d \sim 1$ Mpc) LG objects. Such clouds will be exposed to the background metagalactic radiation field that ionizes and heats the gas. The dark-matter confined clouds may also be subjected to bounding pressures, provided for example, by a hot circumgalactic Galactic corona, or by an intergalactic medium filling the Local Group.

We address several questions. Given the observed HI column densities and distributions what are the halo virial masses and characteristic dark matter densities required to confine the gas clouds? Are the required halo properties consistent with those expected from cosmological structure formation simulations? Under the assumption of photoionization by the metagalactic field, what are the minimum gas masses and column densities required for the formation of neutral hydrogen cores within the dark-matter halos? Are the observed HI distributions consistent with photoionization by the metagalactic field? Under what conditions do the cloud cores become multi-phased? Can halo models be constructed for the pressure supported HI clouds in the Local Group dwarf galaxies? If the CHVCs are the starless “cousins” of the dwarf galaxies, and the CHVC and dwarf galaxy halos are similar, what are the implied distances to the CHVCs?

We construct general purpose models in which we compute the gas density distributions and ionization structures of pressure supported hydrostatic hydrogen gas clouds that are trapped in the potential wells of DM halos, are simultaneously heated and photoionized by an external radiation field, and are subjected to specified bounding pressures. Computations along these lines have been presented in the literature (with varying degrees of sophistication) mainly in the context of the mini-halo model for the intergalactic Ly α clouds (e.g. Rees 1986; Murakami & Ikeuchi 1990; Miralda-Escude & Rees 1993; Kepner et al. 1997). Of most relevance here are the computations presented by Kepner et al. (see also Corbelli & Salpeter 1993) who studied the phase transitions (ionized/neutral/molecular) of hydrogen gas clouds

in DM halos. Their main focus was to show that low-mass halos form shielded neutral gas cores (a precondition for star-formation) only at late ($z \lesssim 1$) cosmic times when the metagalactic photoionizing radiation field has become sufficiently diluted (Efstathiou 1992). However, Kepner et al. made several simplifying assumptions that make it difficult to apply their models to either the CHVCs or the LG dwarf galaxies. These included assuming a fixed relation between the halo mass and the characteristic DM density (see §2), adopting an arbitrary functional relationship between the total gas mass and halo mass, and the neglect of external pressure. In our analysis we relax all of these assumptions.

In addition, we determine the conditions required for the formation of thermally unstable multi-phased cores. To do this we employ and extend the methods presented by Wolfire et al. (1995a) in their study of the multi-phased Galactic disk, and calculate the thermal equilibrium properties of low metallicity HI gas heated by the metagalactic field. We then incorporate the results of these computations into our dark-matter halo models. We note that Wolfire et al. (1995b) (see also Ferrara & Field 1994) carried out an explicit analysis of the HVC complexes observed by Wakker & Schwarz (1991). In particular, the cloud distances were constrained by arguing that the CNM detected by Wakker & Schwarz is possible only when the ambient gas pressure, exceeds a well defined minimum P_{\min} . In this analysis the gas pressure is provided by a Galactic X-ray corona. However, Wolfire et al. did not consider dark-matter dominated clouds. In such systems the central cloud pressures can become much larger than the ambient pressures. The transition from the WNM to the CNM phase then becomes possible in the cloud cores even when the ambient pressure is much smaller than P_{\min} .

We first discuss in §2 the basic parameters and properties of the dark-matter halos we consider in our study, including also a discussion of the relevant cosmological scaling relations. In §3 we then describe our model clouds and discuss the methods we use to compute the cloud hydrostatics, radiative transfer, and HI phase structure. In §4 we discuss our representation of the metagalactic background field. In §5 we derive several useful analytic formulae for the gas distributions in DM halos. In §6 we present the results of our numerical computations. In §7 we model the HI gas structures in the dwarf galaxies Leo A and Sag DIG. In §8 we consider models of the CHVCs as either circumgalactic or extragalactic mini-halos. A summary is presented in §9.

2. Dark Matter Halos

The analytic theory (Gunn & Gott 1972) of non-linear (“spherical top-hat”) gravitational collapse shows that individual DM halos are most simply characterized by two inde-

pendent parameters (e.g. the characteristic density and halo radius). Numerical simulations of the dissipationless collapse of cold dark matter (NFW; Bullock et al. 2001) show that the DM distributions within the halos can be well represented by a spherically symmetric universal density profile (the “NFW profile”) over a wide range of mass scales. The simulations also show that for any particular cosmological model the two halo parameters are highly correlated. The correlation exists because a given mass-scale is associated with a particular virialization red-shift, with narrow dispersion.

An important feature of the NFW profiles is that they are cuspy with diverging central DM densities. Central cusps in CDM halos are a predicted theoretical result of the dissipationless collapse. However, HI rotation curves in dark-matter dominated dwarfs and in several low surface brightness galaxies imply the presence of constant density cores (Moore 1994; Burkert 1995; Blais-Ouellette, Amram & Carignan 2001; Firmani et al. 2001), although this conclusion may be hampered by beam smearing effects (van den Bosch & Swaters 2001; van den Bosch et al. 2000). In view of the HI rotation curves, Burkert (1995) introduced a semi-empirical profile (the “Burkert profile”) in which the cuspy NFW core is replaced with a uniform density core. In our analysis we consider both NFW and Burkert profiles.

Realistic dark matter halos may be complex triaxial structures, containing embedded clumps (sub-halos) and elongated filaments. In our analysis we represent the halos assuming they are spherically symmetric and smooth. We begin by defining the basic halo parameters for spherically symmetric systems, and we then discuss the cosmological correlation relation between the halo scale parameters.

2.1. Halo Parameters

For spherically symmetric halos, the dark-matter density distribution may be written as

$$\rho_d = \rho_{ds} f_\rho(x) \tag{1}$$

where ρ_{ds} is the characteristic “scale density” of the halo, f_ρ is the density profile, and $x \equiv r/r_s$ is the dimensionless radial coordinate, where r is the distance from the halo center and r_s is the “scale radius” of the DM distribution. For realistic density profiles, the DM density is large for $x < 1$ and becomes small when $x \gg 1$.

The enclosed DM mass at any radius is then

$$M_d = M_{ds} f_M(x) \quad , \tag{2}$$

where

$$f_M(x) = 3 \int_0^x f_\rho(x') x'^2 dx' \quad , \quad (3)$$

and

$$M_{ds} \equiv \frac{4\pi}{3} \rho_{ds} r_s^3 \quad , \quad (4)$$

is the characteristic or “scale mass” of the halo.

The gravitational potential of the halo may be written as

$$\varphi = v_s^2 f_\varphi(x) \quad (5)$$

where

$$f_\varphi(x) = \int_0^x \frac{f_M(x')}{x'^2} dx' \quad , \quad (6)$$

and where we define the “scale (circular) velocity”

$$v_s^2 \equiv \frac{GM_{ds}}{r_s} = \frac{4\pi G}{3} \rho_{ds} r_s^2 \quad , \quad (7)$$

where G is the gravitational constant.

The circular velocity at any distance from the halo center is

$$v = v_s f_v(x) \quad (8)$$

where

$$f_v(x) = \left[\frac{f_M(x)}{x} \right]^{1/2} \quad . \quad (9)$$

It is evident from equations (1)-(3) that for an assumed density profile f_ρ the physical scales of a halo are fixed by two independent structural parameters. These may be chosen as two out of the four mutually dependent parameters ρ_{ds} , r_s , v_s or M_{ds} . E.g., a halo may be defined by the scale density and radius, ρ_{ds} and r_s (using eq. [1]), or by the scale velocity and radius, v_s and r_s (using eq. [5]). The functions f_ρ , f_M , and f_φ for NFW and Burkert halos are listed in Table 5 in Appendix A.

2.2. Cosmological Relations

In cosmological studies the two independent halo scale parameters are often given in terms of the virial radius, r_{vir} (or the virial mass M_{vir}), and the “concentration parameter,” $x_{\text{vir}} \equiv r_{\text{vir}}/r_s$ (often denoted by “ C ”). The virial radius is defined as the radius within which

the mean dark-matter density of the halo exceeds the background matter density of the universe, ρ_u , by a factor $\Delta \sim 200$, corresponding to the overdensities expected in collapsed and virialized objects (Gunn & Gott 1972). The virial mass,

$$M_{\text{vir}} \equiv \frac{4\pi}{3} \Delta \rho_u r_{\text{vir}}^3 \quad (10)$$

is the DM mass enclosed within the virial radius. Thus, $M_{\text{vir}} = M_{ds} f_M(x_{\text{vir}})$.

With these definitions it follows that

$$\rho_{ds} = \Delta \rho_u \frac{x_{\text{vir}}^3}{f_M(x_{\text{vir}})} \quad , \quad (11)$$

$$r_s = \left(\frac{3}{4\pi \Delta \rho_u} \right)^{1/3} M_{\text{vir}}^{1/3} \frac{1}{x_{\text{vir}}} \quad , \quad (12)$$

and

$$v_s = \left(\frac{4\pi}{3} G^3 \Delta \rho_u \right)^{1/6} M_{\text{vir}}^{1/3} \left[\frac{x_{\text{vir}}}{f_M(x_{\text{vir}})} \right]^{1/2} \quad . \quad (13)$$

In these expressions, the matter density ρ_u and the overdensity factor Δ are fixed by the underlying cosmological model. The halo scale parameters ρ_s , r_s , and v_s , are then determined by a choice of M_{vir} and x_{vir} .

An important feature of the CDM collapse simulations is the finding that at any cosmic epoch the two independent halo scale parameters are correlated, over a wide range of halo masses (Navarro, Frenk & White 1996, 1997; Bullock et al. 2001). The correlation can be expressed in several ways, e.g., as a relation, $x_{\text{vir}}(M_{\text{vir}})$, between the concentration parameter and the virial mass, or as a relation, $r_s(\rho_{ds})$, between the scale radius and scale density. The correlation exists because a given mass scale (as defined for example by r_s and ρ_{ds}) is associated with a narrow range of virialization redshifts, while the halo scale density ρ_{ds} is effectively determined by the value of the cosmic matter density at the epoch of virialization. The numerical simulations show that for any assumed cosmological model the correlation is well approximated by a simple power-law relation $x_{\text{vir}} \sim M_{\text{vir}}^\alpha$, where for low masses the index α is a weak function of the mass. For a given virial mass a dispersion of concentrations is found, with increasing departures from the typical concentration being less likely.

We adopt the results of Bullock et al. (2001) for simulations carried out assuming the “concordance” Λ CDM cosmological model (Bahcall et al. 1999). In this model the matter and vacuum density parameters $\Omega_m = 0.3$ and $\Omega_\Lambda = 0.7$, the Hubble constant $H_0 = 70 \text{ km s}^{-1} \text{ Mpc}^{-1}$, the root-mean-square (rms) amplitude of mass fluctuations in spheres of radius $8h^{-1} \text{ Mpc}$ $\sigma_8 = 1$, and the present day matter density of the universe is $\rho_u = 2.76 \times 10^{-30}$

$\text{g cm}^{-3} = 1.66 \times 10^{-6} \text{ amu cm}^{-3}$.⁶ For this model the overdensity factor Δ for virialized halos equals 340 (Bryan & Norman 1997). The fraction of matter contained in baryons is $\Omega_b/\Omega_m = 0.088$ (assuming $\Omega_b h^2 = 0.013$).

We are interested in the predicted halo properties at the current epoch ($z = 0$). Bullock et al. carried out numerical simulations for halos with present-day virial masses ranging from $10^{14} M_\odot$ down to $10^{11} M_\odot$. They also presented a “toy model” for the halo evolution that accurately reproduces the relation between concentration parameter and virial mass found in the collapse simulations. The numerical results show that the dispersion in concentrations (for a given halos mass) is well approximated by a log-normal distribution in which σ standard deviations correspond to departures $\Delta(\log x_{\text{vir}}) = 0.14\sigma$ from the median concentration⁷. For halos between 10^{11} and $10^{14} M_\odot$, Bullock et al. find that the expression

$$x_{\text{vir}} = 10.3 \times 10^{0.14\sigma} \left(\frac{M_{\text{vir}}}{10^{13} M_\odot} \right)^{-0.13} \quad (14)$$

provides an accurate fit to the results of their numerical simulation and associated toy model.

In our study we are interested in low-mass halos with virial masses in the range $\sim 10^8$ to $10^{10} M_\odot$, at and somewhat below the “dwarf galaxy” mass scale. This mass range is well below the resolution of the numerical simulations presented by Bullock et al. We therefore use their Λ CDM toy model (Bullock priv. comm.) to compute the concentrations for low-mass halos. In Figure 1 we plot the computed concentrations for median ($\sigma = 0$) halos with virial masses equal to 10^8 , 10^9 , 10^{10} and $10^{11} M_\odot$. We find that the fit

$$x_{\text{vir}} = 27 \times 10^{0.14\sigma} \left(\frac{M_{\text{vir}}}{10^9 M_\odot} \right)^{-0.08} \quad (15)$$

is accurate to within 3% of the toy-model computations for median halos. In this expression we have also assumed that, as for the high-mass halos, one-sigma deviations correspond to $\Delta(\log x_{\text{vir}}) = 0.14$ departures from median halos. In Figure 2 we plot the $x_{\text{vir}}(M_{\text{vir}})$ relation, as given by equation (15) for families of $+3\sigma$ overconcentrated, median, and -3σ underconcentrated halos. The weak mass dependence, and the slight flattening of the power-index, from $\alpha = -0.13$ in equation (14) to $\alpha = -0.08$ in equation (15), is consistent with the behavior of the (post-recombination) cold dark matter fluctuation spectrum, which remains flat at low masses (Peebles 1982; Blumenthal et al. 1984; Eke, Navarro & Steinmetz 2001).

⁶A density of 1 amu cm^{-3} equals $1.66 \times 10^{-24} \text{ g cm}^{-3} = 0.93 \text{ GeV cm}^{-3} = 2.45 \times 10^{-2} M_\odot \text{ pc}^{-3}$.

⁷Due to a typographical error the 1σ deviations are incorrectly given as $\Delta(\log x_{\text{vir}}) = 0.18$ in Bullock et al. (2001) (Bullock priv. comm.).

For a given value of σ , equation (15) together with equations (11), (12), and (13) may be used to compute all of the halo properties as functions of a single halo parameter. As is indicated by these equations, the resulting scale parameters depend on the enclosed mass function $f_M(x)$. We find that virtually identical results are obtained for NFW halos and Burkert halos. In Figure 2 we plot the halo concentration, x_{vir} , the virial mass, M_{vir} , the scale density, $n_{ds} \equiv \rho_{ds}/m_{\text{H}}$ (amu cm $^{-3}$), and the halo scale radius, r_s (kpc), as functions of the halo and scale velocity, v_s (km s $^{-1}$)⁸. We display these quantities for $+3\sigma$, median, and -3σ halos. For median halos, the scale radius r_s ranges from 0.29 to 6.4 kpc, for v_s between 10 and 100 km s $^{-1}$. The scale density increases with decreasing v_s , reflecting the earlier collapse epoch of lower mass halos. However, as expected, the density dependence is weak. For median halos, n_{ds} decreases from 2.7 to 0.55 amu cm $^{-3}$ for v_s between 10 and 100 km s $^{-1}$. For a narrow range of scale velocities, large changes in the characteristic DM densities are possible only by varying σ , i.e., by moving to over-concentrated or underconcentrated halos.

In his study of rotationally supported dwarf galaxies, Burkert (1995) found that the radii of the inferred (constant density) DM halo cores are correlated with the magnitudes of the observed circular velocities, as expected theoretically. In Figure 2 we plot the observed⁹ correlation between r_s and v_s for the four low-mass dwarf spiral galaxies (DDO 154, DDO 170 NGC 3109, and DDO 105) in Burkert’s sample (see his Fig. 2). It is evident that these objects lie precisely on the expected relation for median ($\sigma = 0$) halos. The dwarf galaxy rotation curve data thus provide empirical support for the theoretically derived correlation relation given by equation (15).

Convenient analytic scaling relations for the various halo parameters as functions of v_s , may be developed by setting $f_M(x) \simeq 1.40x^{1/2}$ in equations (11) and (13). This approximation for f_M is accurate to within 12%, for both Burkert and NFW halos, for $4.5 < x < 50$. It then follows that

$$x_{\text{vir}} = 32.1 \times 10^{0.149\sigma} v_{s6}^{-0.225} \quad , \quad (16)$$

$$M_{\text{vir}} = 5.55 \times 10^7 \times 10^{-0.112\sigma} v_{s6}^{3.191} \text{ M}_{\odot} \quad , \quad (17)$$

$$n_{ds} = 2.71 \times 10^{0.373\sigma} v_{s6}^{-0.638} \text{ amu cm}^{-3} \quad , \quad (18)$$

⁸In cosmological studies, halos are often parameterized by the circular velocity at the virial radius, $v_{\text{vir}} \equiv v_s[f_M(x_{\text{vir}})/x_{\text{vir}}]^{1/2}$, or the maximum circular velocity $v_{\text{max}} = 0.8v_s$ (for NFW and Burkert potentials). We prefer to use v_s as it directly fixes the potential-well depth (see eq. [5]).

⁹Burkert (1995) actually plotted the correlation between r_s and the observed circular velocity at r_s . We have transformed the observed velocities to scale velocities using equation (8) and Burkert’s profile. This gives $v(r_s) = 0.618v_s$.

and

$$r_s = 0.29 \times 10^{-0.186\sigma} v_{s6}^{1.319} \text{ kpc} \quad , \quad (19)$$

where $v_{s6} \equiv v_s/10 \text{ km s}^{-1}$. These expressions are plotted as the dashed lines in Figure 2. They provide excellent analytic representations (to within 1% accuracy) of the halo scalings for median and underconcentrated halos, and are less accurate ($\sim 30\%$) for over-concentrated halos.

In our computations we adopt the $x_{\text{vir}}(M_{\text{vir}})$ correlation relation as given by expression (15), and the resulting halo parameters displayed in Figures 1 and 2, as theoretically motivated guides to the properties of “median” low-mass halos. In our study, we also explicitly consider halos that are substantially “over-concentrated” or “under-concentrated” with respect to the median halos.

3. Clouds

We are interested in determining the structural properties of hydrostatic gas clouds that are confined by gravitationally dominant dark-matter halos, and are in ionization and thermal equilibrium with an external source of Lyman continuum (Lyc) and far-ultraviolet (FUV) radiation. We focus on ionization and heating by the metagalactic field. We envision clouds consisting of a “warm medium” (WM) with up to three components; (a) an outer layer of warm photoionized gas (WIM), that serves as a shielding layer for (b) a neutral core of warm HI gas (WNM), and possibly (c) a still smaller region within which the HI can exist as a multi-phased (WNM/CNM) mixture of warm and cold gas. When ionizing radiation is present, the WIM component will always be present. However, the WNM and WNM/CNM components will not always exist, and one of our goals is to determine the specific conditions required for their formation.

We consider the possibility that the halo-cloud systems are embedded within a low-density hot ionized medium (HIM), provided for example by a Galactic X-ray corona in the circumgalactic environment, or an intergalactic medium in the Local Group environment. The HIM exerts a bounding pressure, P_{HIM} , on the outer surface of the WM cloud and serves to further confine the WM gas, particularly in the limit of weak DM halo potentials. We assume that the HIM is sufficiently hot such that it is completely unbound to any of the halos we consider. We also assume that the HIM is optically thin to the background radiation field.

We wish to address several questions. For a given dark-matter halo and a total mass of warm gas, what are the radial extents and associated column densities of the HI gas

distributions? For small gas masses we expect the WM clouds to be photoionized throughout. In such WIM dominated clouds, any HI is present as a small neutral fraction within the ionized gas. As the gas mass is increased the WIM component can be expected to become optically thick to the ionizing radiation, leading to the formation of a neutral hydrogen WNM core. For an assumed halo and background field, what is the minimum WM mass required for the formation of a neutral WNM core? When WNM cores exist, how large are they? How do the core sizes and associated HI column densities depend on the halo scale parameters? If the hydrostatic pressure gradients are sufficiently large the central gas pressures may become large enough to allow a multi-phased WNM/CNM medium (or a complete conversion to CNM) in the neutral cores. For clouds in which the ionization and heating is dominated by the metagalactic field, when is multi-phased behavior possible in the neutral cores?

To address these questions, we first construct models in which we solve the coupled equations of hydrostatic equilibrium and radiative transfer for *warm* spherically symmetric clouds that are (a) confined by gravitationally dominant halos, (b) subjected to a bounding pressure, and (c) exposed to an external source of Lyc and FUV radiation that ionizes the gas. We focus on irradiation by the metagalactic field. Because the temperatures of the warm components are expected to lie in a narrow range ($\sim 10^4$ K) we specify the gas temperatures for the WIM and WNM components in advance in these computations. Given the resulting radial profiles for the hydrostatic gas pressures, densities, and fractional ionizations, we compute various quantities of observational interest including the HI gas masses and column densities, gas scale heights, locations of the ionization fronts (if present), cloud emission measures, H α surface brightnesses, and other quantities of interest. Our treatment of the cloud hydrostatics and radiative transfer is described in §3.1.

We then determine the phase states of the HI gas in the neutral cores (when such cores exist). The thermal phase state of the neutral gas at each cloud radius is determined by comparing the local value of the hydrostatic pressure $P(x)$ to the local values of two critical pressures $P_{\min}(x)$ and $P_{\max}(x)$. At low pressures $P < P_{\min}$ the gas is WNM, at intermediate pressures $P_{\min} < P < P_{\max}$ the gas is multi-phased, and at high pressures $P > P_{\max}$ the gas must convert to CNM.¹⁰

¹⁰The fact that interstellar HI gas can exist as WNM and CNM has been the subject of many theoretical investigations (e.g., Field, Goldsmith & Habing 1969; Zeldovich & Pikelner 1969; McKee & Ostriker 1977; de Jong 1977; Draine 1978; Ferriere, Zweibel & Shull 1988; see also the reviews by Field 1975, and Kulkarni & Heiles 1987, 1988). Recent comprehensive theoretical studies have been presented by Wolfire et al. (1995a; 2002). The two distinct phases are possible because the gas heating rates are generally proportional to the gas density, n_{H} , whereas the gas cooling rates are proportional to n_{H}^2 . Thus, at low densities cooling becomes inefficient, and the temperature is driven to maximal (WNM) values of $\sim 10^4$ K set by Ly α cooling.

As we discuss in §3.2 for a given incident radiation field the critical pressures P_{\min} and P_{\max} for shielded HI gas can be expressed as functions of the primary ionization rate ζ_p , independent of the cloud geometry (e.g. spherical vs. plane parallel). In §3.2 we present the results of thermal equilibrium computations which yield the required $P_{\min}(\zeta_p)$ and $P_{\max}(\zeta_p)$.

Given $P_{\min}(\zeta_p)$ and $P_{\max}(\zeta_p)$ we determine the phase states of the HI gas in our halo-cloud models. In these models the local hydrostatic pressure depends on the depth of the halo potential well and the value of the bounding pressure, and increases from the surface to the core. Conversely, P_{\min} and P_{\max} decrease from the surface to the core as the ionization rate ζ_p decreases with increasing cloud depth and opacity. Thus, any neutral gas may be expected to be pure WNM at large radii where $P < P_{\min}$, but may become multi-phased or fully converted to CNM at small radii where $P_{\min} < P < P_{\max}$ or $P > P_{\max}$. For sufficiently deep halo potentials the conversion to CNM may occur even if the ambient bounding pressure is negligibly small.

We determine the conditions for which $P_{\min}(0) < P_0 < P_{\max}(0)$ where P_0 is the central pressure. In such clouds the multi-phased cores will extend out to a radius x where $P(x) = P_{\min}(x)$. We assume that in the multiphased zones the CNM occupies negligible volume but remains uniformly mixed with the WNM. When $P_0 > P_{\max}(0)$ the HI in the cores will be driven entirely into the CNM phase. When this happens, thermal support is lost, and our hydrostatic solution in which warm gas is assumed to be present from the cloud center to the surface, becomes inconsistent with gas heating by the external field. Either additional (internal) heat sources must be postulated, or the cloud must collapse. Thus, in our computations we find the maximum masses, M_{WNMmax} , of warm gas that can be maintained by the external field within a given halo and an assumed bounding pressure. The total mass of CNM is unconstrained in our models, except that we assume it cannot dominate the gravitational potential.

At high densities, cooling by fine structure line emission, primarily $158\mu\text{m}$ [CII] emission, becomes much more effective and the gas can cool to CNM temperatures $\lesssim 100$ K. At intermediate densities a thermal instability occurs as the dominant cooling mechanism switches from $\text{Ly}\alpha$ to [CII] emission. The instability and multiphased behavior occurs within a range of pressures – P_{\min} to P_{\max} – that depend on the detailed heating and cooling rates. For pressures less than P_{\min} only the warm phase is possible, and for pressures greater than P_{\max} only the cold phase is possible.

3.1. Hydrostatics and Radiative Transfer

In hydrostatic equilibrium

$$dP = -\rho d\varphi \quad , \quad (20)$$

where P is the gas pressure, ρ is the gas density, and φ is the gravitational potential. The pressure $P = \rho c_g^2$, where $c_g^2 \equiv kT/\langle m \rangle$ is the isothermal sound speed of the gas, T is the gas temperature, and $\langle m \rangle$ is the mean mass per gas particle. We assume that the potential is dominated by the dark-matter halo so that $\varphi = v_s^2 f_\varphi(x)$, where v_s is the halo scale velocity and f_φ is the dimensionless potential for either NFW or Burkert halos. It follows that the gas pressure $P(x)$ is given by

$$P(x) = P_0 \exp \left[- \int_0^x \frac{v_s^2}{c_g^2} \frac{f_M(x')}{x'^2} dx' \right] \quad (21)$$

where $f_M(x)$ is the (dimensionless) DM mass distribution function, and P_0 is the central gas pressure. It is evident that the hydrostatic structure is controlled by the ratio, v_s/c_g , of the halo scale velocity to the gas sound speed. The hydrostatic and ionization structures of the cloud are coupled since the sound speed c_g depends on T and $\langle m \rangle$, which vary with the ionization state.

In ionization equilibrium

$$\zeta n(\text{H}^0) = \alpha_B n(\text{H}^+) n(e), \quad (22)$$

where ζ is the total local photoionization rate, and $n(\text{H}^0)$, $n(\text{H}^+)$ and $n(e)$ are the atomic hydrogen, proton and electron densities respectively. We assume a case-B recombination coefficient α_B . The local primary photoionization rate is

$$\zeta_p(x) = 4\pi \int_{\nu_0}^{\infty} \sigma_\nu J^*(\nu, x) d\nu \quad (23)$$

where ν_0 is the Lyman limit frequency, σ_ν is the photoabsorption cross section, and $J^*(\nu, x)$ is the local mean photon intensity

$$J^*(\nu, x) \equiv \frac{1}{2} J_0^*(\nu) \int_{-1}^1 \exp \left[-\sigma_\nu N_{\text{HI}}(x, \mu) \right] d\mu, \quad (24)$$

where $J_0^*(\nu)$ is the unattenuated isotropic radiation field (in units of photons $\text{cm}^{-2} \text{s}^{-1} \text{Hz}^{-1} \text{sr}^{-1}$), $N_{\text{HI}}(x, \mu)$ is the HI absorbing column from the cloud surface to x along a ray that is inclined by an angle θ relative to the outward radial direction, and where $\mu \equiv \cos\theta$.

For the range of hydrogen gas columns (up to $\sim 10^{22} \text{ cm}^{-2}$) that we consider in our computations, the gas opacity is dominated by a combination of hydrogen and helium photoabsorptions. We assume a primordial helium abundance $n_{\text{He}}/n_{\text{H}} = 1/12$ (Olive & Steigman

1995; Ballantyne, Ferland & Martin 2000) where n_{H} and n_{He} are the total hydrogen and helium particle densities respectively. Photoabsorptions by heavier “metals” may be neglected for the low metallicities ($Z \lesssim 0.1$) we assume (Morrison & McCammon 1983; Balucinska-Church & McCammon 1992). In our treatment of the radiative transfer we make the simplifying approximation that the hydrogen and helium ionization fractions are equal at all locations. We also assume that every helium recombination photon is absorbed in a hydrogen ionization. With these assumptions $\sigma_{\nu} = \sigma_{\nu,\text{H}} + (1/12)\sigma_{\nu,\text{He}}$. We adopt the Balucinska-Church & McCammon expressions for $\sigma_{\nu,\text{H}}$ and $\sigma_{\nu,\text{He}}$. In computing the total ionization rate we also include the contributions of the secondary collisional ionizations produced by the primary photoelectrons (Shull & van Steenberg 1985).

We construct models assuming that the background metagalactic field is the dominant source of radiation impinging on the clouds. Our representation of this field is displayed in Figure 3 in a νJ_{ν} plot. We discuss our fit to the metagalactic field in Appendix B. For our assumed field $4\pi J^* = 1.28 \times 10^4 \text{ photons s}^{-1} \text{ cm}^{-2}$, where the Ly α integral

$$4\pi J^* \equiv \int d\Omega \int_{\nu_0}^{\infty} d\nu \frac{I_{\nu}}{h\nu} \quad . \quad (25)$$

Most (93%) of the photons are emitted between 1 and 4 ryd. The unattenuated primary hydrogen ionization rate is $\zeta_{\text{p},0} = 4 \times 10^{-14} \text{ s}^{-1}$.

For our assumed helium abundance,

$$P = \frac{13}{12}(1 + x_p)n_{\text{H}}kT \quad (26)$$

where $x_p \equiv n(H^+)/n_{\text{H}}$ is the proton fraction. The electron fraction $x_e \equiv n(e)/n_{\text{H}} = \frac{13}{12}x_p$. The mean mass per gas particle is

$$\langle m \rangle = \frac{16}{13} \frac{1}{1 + x_p} m_{\text{H}} \quad (27)$$

where m_{H} is the atomic hydrogen mass.

In our computations we assume $T = 10^4 \text{ K}$ for both the WNM and the WIM. To verify this assumption for the WIM we have computed the gas temperature of low-metallicity photoionized gas using CLOUDY (version C90.04, Ferland et al. 1998)¹¹ assuming an ionizing field as given by our representation of the metagalactic field discussed in Appendix B. We find that the gas temperature of the ionized gas ranges from 8.0×10^3 to $1.2 \times 10^4 \text{ K}$ for gas

¹¹See www.pa.uky.edu/~gary/cloudy/

densities in the range 10^{-3} to 0.1 cm^{-3} . The HI thermal phase computations we discuss in §3.2 show that the WNM gas temperature is close to 10^4 K . For 10^4 K gas, the associated gas sound speeds are $c_{g,\text{WNM}} = 8.19 \text{ km s}^{-1}$ for the WNM, and $c_{g,\text{WIM}} = 11.6 \text{ km s}^{-1}$ for the WIM.

The local gas pressure, fractional ionization, and gas temperature, determine the local density of hydrogen nuclei n_{H} via equation (26). We define the hydrogen gas (ionized plus neutral) density distribution f_{gas} such that

$$n_{\text{H}} = n_{\text{H},0} f_{\text{gas}}(x) \quad (28)$$

where $n_{\text{H},0}$ is the central density. We define the outer edge of the WM cloud as the radius $x_{\text{W/H}}$ at which the cloud pressure is equal to the pressure P_{HIM} of the enveloping hot ionized medium. Thus, $x_{\text{W/H}}$ is located at the interface between the WIM and the HIM. The total (hydrogen) cloud mass is then

$$M_{\text{WM}} = 4\pi r_s^3 m_{\text{H}} n_{\text{H},0} \int_0^{x_{\text{W/H}}} f_{\text{gas}}(x) x^2 dx \quad . \quad (29)$$

For a given halo potential and background field, a cloud model is selected by choosing a value for the total mass M_{WM} given an assumed value for P_{HIM} , or equivalently, setting the boundary condition that the pressure at a selected value of $x_{\text{W/H}}$ equals P_{HIM} .

We have constructed a code to solve the coupled hydrostatic and ionization equilibrium equations. In our numerical solution we specify P_{HIM} and $x_{\text{W/H}}$, and then adopt an iterative procedure. First, we assume an ionization and opacity structure for the gas (initially by setting $x_e = 1$ everywhere, and assuming that the cloud is optically thin). We then integrate equation (21) subject to the boundary condition $P(x_{\text{W/H}}) = P_{\text{HIM}}$. This yields a hydrostatic pressure distribution $P(x)$, and a value for the central pressure. $P(x)$ and the assumed ionization structure determine the local values for the hydrogen gas densities. We then compute the local photoionization rates given the absorbing columns and opacities to the cloud surface. Given the ionization rates and the hydrogen gas densities we solve the equation of ionization equilibrium and find new values for the ionization fractions x_e and cloud opacities. The local gas sound speeds are then updated, and the hydrostatic structure is recomputed etc. We iterate until the local ionization fractions have converged to within 1%.

Given the solutions to the hydrostatic and ionization structures, several quantities of interest may be computed, including the total gas column densities, the HI masses and columns, the cloud emission measures and $\text{H}\alpha$ surface brightnesses, the gas scale heights, and the location of the ionization fronts.

The total column density of hydrogen nuclei along a line-of-sight with impact parameter x from the cloud center is

$$N_{\text{WM}}(x) \equiv 2n_{\text{H},0}r_s \int_x^{x_{\text{W/H}}} f_{\text{gas}}(x') \frac{x'}{[x'^2 - x^2]^{1/2}} dx' \quad , \quad (30)$$

and the HI column density along a line-of-sight a distance x from the cloud center is

$$N_{\text{HI}}(x) \equiv 2n_{\text{H},0}r_s \int_x^{x_{\text{W/H}}} (1 - x_p) f_{\text{gas}}(x') \frac{x'}{[x'^2 - x^2]^{1/2}} dx' \quad , \quad (31)$$

where x_p is the local proton fraction.

The emission measure along a line-of-sight with impact parameter x is

$$EM(x) = 2n_{\text{H},0}^2 r_s \int_x^{x_{\text{W/H}}} x_e x_p f_{\text{gas}}^2(x') \frac{x'}{[x'^2 - x^2]^{1/2}} dx' \quad (32)$$

where x_e and x_p are the local electron and proton fractions. The associated $\text{H}\alpha$ surface brightness in milli-Rayleighs may be written as

$$I_{\text{H}\alpha}^*(x) = 10^9 \alpha_{\text{eff}} EM = 364 EM_{\text{pc}} \quad \text{mR}, \quad (33)$$

where $\alpha_{\text{eff}} = 8.7 \times 10^{-14} \text{ cm}^3 \text{ s}^{-1}$ is the $\text{H}\alpha$ effective recombination coefficient (Osterbrock 1989) and EM_{pc} is the emission measure in $\text{cm}^{-6} \text{ pc}$.

While formal solutions may be found for all values of P_{HIM} and x_{HIM} , several additional conditions must be satisfied for physically realizable solutions. First, while the halos formally extend to infinite radius, we assume that effective physical boundaries exist beyond which both the baryons and dark-matter particles are subjected to external forces that readily detach them from the halo systems. As a plausible limit we assume that the radii of the halos and trapped clouds cannot exceed the virial radius. Thus, we require that $x_{\text{W/H}} < x_{\text{vir}}$ (where x_{vir} is the halo concentration parameter). If the halos are tidally truncated within the virial radius, then the limit becomes $x_{\text{W/H}} < r_t/r_s$, where r_t is the tidal radius.

Second, self-consistent solutions require that the DM mass dominates the gas mass at all radii, otherwise the assumption that the halo gravity dominates is violated. Self-consistent solutions must necessarily satisfy the condition $M_{\text{WM}} < M_{\text{DM}}(x_{\text{W/H}})$, where $M_{\text{DM}}(x_{\text{W/H}})$ is the dark-matter mass enclosed within the entire WM cloud.

Third, the WM gas must be well bound to the halos. Otherwise, mass loss (especially from the outer WIM layers) will occur. We define bound WM clouds as those that satisfy the condition

$$\frac{\mathcal{W}}{\mathcal{T}} \equiv \frac{v_s^2 [f_\varphi(x_{\text{W/H}}) - f_\varphi(\infty)]}{\frac{3}{2} c_{\text{WIM}}^2} > 1 \quad (34)$$

where \mathcal{W} is the gravitational potential energy per particle at $x_{\text{W/H}}$, and $\mathcal{T} = (3/2)c_{\text{WIM}}^2$ is the mean thermal energy per particle in the outer WIM layer¹².

We conclude this section by making an important distinction between *pressure-confined* and *gravitationally-confined* clouds. Because the depths of the halo potential wells we are considering are finite (as $x \rightarrow \infty$, $f_\varphi \rightarrow 3$ for NFW halos, and $f_\varphi \rightarrow 3\pi/4$ for Burkert halos, see Appendix A) a maximum possible pressure (density) contrast between large and small radii exists for a given value of v_s/c_g . When v_s/c_g is small the maximum pressure (density) contrast is small, and the gas extends to large halo radii $x \gg 1$. In this limit a cloud of finite mass must be pressure-confined, and the halo gravity provides just a small pressure enhancement towards the cloud center. In pressure-confined clouds, properties such as the total cloud mass, or the internal gas pressure, are determined by conditions at the cloud surface via the bounding pressure P_{HIM} . Pressure-confined clouds will tend to become unbound as the confining pressure becomes small.

When v_s/c_g is large the pressure contrast becomes large, and the gas is effectively restricted to small halo radii $x \ll 1$. In this limit, which we refer to as the “small- x ” limit, the cloud is gravitationally confined, and for any plausible value of the central pressure (or density), the total gas mass remains finite for arbitrarily small bounding pressures. Clouds may be assumed to be in the small- x limit when $v_s/c_g \gtrsim 1.5$ (see Appendix A). In gravitationally confined clouds, properties such as the total mass or internal gas pressure are determined by the central gas pressure, that is, by conditions at the cloud centers. Gravitationally confined clouds become increasingly bound as v_s/c_g becomes large and the potential wells deepen. When the observable gas is in the small- x limit, the implied dynamical mass $M_{\text{dyn}} = c_g^2 r_{\text{gas}}/G$ (where r_{gas} is the observed gas scale height) is a small fraction of the halo scale mass, and an even smaller fraction of the virial mass. In gravitationally confined clouds, much more dark-matter must exist beyond the observed gas structures, unless the halos are truncated at radii much less than their virial radii.

In Appendix A we present simple analytic expressions for the gas scale heights, gas masses, and column densities, for clouds in the small- x limit, and we derive an analytic condition for the transition from fully ionized clouds to clouds containing neutral cores. These analytic results (for both NFW and Burkert halos) are summarized in Table 6, and may be used as guides to understanding the numerical model results we present in §4, §5, and §6.

¹²A similar condition was adopted by Barkana & Loeb (1998) in their study of the photoevaporation of gas in low-mass halos at the reionization epoch.

3.2. P_{\min} and P_{\max}

We employ the methods described in Wolfire et al. (1995a, 2002) to compute P vs. n_H “thermal phase diagrams” for low-metallicity HI gas heated by metagalactic radiation for a wide range of assumed HI shielding columns. We use the results of these computations to determine the critical pressures P_{\min} and P_{\max} as functions of the shielding column and associated primary ionization rate ζ_p .

In our phase diagram computations the equations of thermal balance and of ionization and chemical equilibrium are solved self-consistently. In these computations we adopt a plane parallel geometry in treating the radiative transfer through the absorbing columns, and we assume an incident flux equal to $2\pi J_\nu^*$ where J_ν is the mean intensity assumed in our spherically symmetric halo cloud models¹³. We calculate the hydrogen ionization rates using the same approximations for the Ly α absorption and opacity that we use in computing the ionization structure of the spherical halo clouds.

The three major heating processes included in our HI phase computations are UV and X-ray ionization, FUV photoelectric emission, and molecular hydrogen (H_2) photodissociation. Their relative importance depends on the Ly α vs. FUV intensities, on the dust-to-gas mass ratio D/G , and the metallicity Z . The metallicity also controls the gas cooling efficiencies. In view of the generally low (but non-negligible) metal abundances observed in the HVCs and CHVCs we assume $Z = 0.1$, where $Z = 1$ corresponds to the Galactic (gas-phase) abundances of $n_O/n_H = 3.2 \times 10^{-4}$ for oxygen (Meyer, Jura & Cardelli 1998) and $n_C/n_H = 1.4 \times 10^{-4}$ for carbon (Cardelli et al. 1996). The dust content and grain properties of the CHVCs are unknown, and we assume that the dust-to-gas ratio is proportional to the metallicity, and set $D/G = 0.1$. Following Wolfire et al. (2002) we adopt a slightly modified form of the Bakes & Tielens (1994) photoelectric heating efficiencies. The FUV field, that leads to photoelectric emission, produces the C^+ cooling ions and photodissociates H_2 , is attenuated by dust absorption. For $D/G = 0.1$ a photoelectric heating FUV optical depth of 1 occurs at an HI column density of $1.1 \times 10^{22} \text{ cm}^{-2}$ (Roberge, Dalgarno & Flannery 1981). We assume that H_2 forms on grain surfaces with a rate coefficient $R = 3 \times 10^{-17} Z \text{ cm}^3 \text{ s}^{-1}$ proportional to the metallicity, and also via the standard gas phase sequence $H + e^- \rightarrow H^- + \nu$, $H^- + H^+ \rightarrow H_2 + \nu$. The H^- abundance is limited by photodetachment, mainly by far-red photons, with a cross section that peaks near 8500 Å (Wishart 1979). Detailed

¹³In spherical clouds the ionization rate near the surface of optically thick clouds is proportional to $2\pi J_\nu^*$, whereas near the cloud center the ionization rate is proportional to $4\pi J_\nu^*$ (see eq. [24]). In our plane-parallel computations we adopt an incident flux equal to a value of $2\pi J_\nu^*$, with the recognition that the resulting P_{\min} and P_{\max} as functions of the *ionization rate* are insensitive to the assumed incident flux.

expressions for the various heating and cooling rates, and the basic atomic and molecular data, are given in Wolfire et al. (1995a) with some updates in Kaufman et al. (1999) and Wolfire et al. (2002).

As a specific example we show in Figure 4 our numerical results for a shielding column $N_{\text{HI}} = 5 \times 10^{19} \text{ cm}^{-2}$. This particular shielding column is important since as we will show this is the typical peak HI column density for WM clouds in which the gas becomes multi-phased in the cloud cores. For our assumed representation of the metagalactic field (see Appendix B), and a shielding column of $5 \times 10^{19} \text{ cm}^{-2}$, the primary hydrogen ionization rate is equal to $1.1 \times 10^{-18} \text{ s}^{-1}$.

The resulting P vs. n_{H} phase diagram is shown in Figure 4a for densities ranging from 10^{-3} to 100 cm^{-3} . The thermally unstable region, defined as the zone where $d(\log P)/d(\log n_{\text{H}}) < 0$, is visible between the WNM and CNM branches, and a two-phased medium is possible for pressures between $P_{\text{min}} = 45.0 \text{ cm}^{-3} \text{ K}$, and $P_{\text{max}} = 310 \text{ cm}^{-3} \text{ K}$. The dominant heating and cooling rates per hydrogen nucleus, Γ and $n_{\text{H}}\Lambda$, are displayed in Figure 4b. UV/X-ray ionization dominates the heating of the WNM. The UV/X-ray heating rate decreases from 2×10^{-28} to $2 \times 10^{-29} \text{ ergs s}^{-1} \text{ H}^{-1}$ in the density range 10^{-3} to 100 cm^{-3} . The decline is due to a decrease in the fractional ionization. As x_e decreases an increasing percentage of the UV/X-ray photoelectron energy is lost in atomic excitations and secondary ionizations rather than being deposited as heat. In contrast, the photoelectric heating rate (and efficiency) remains approximately constant, and is equal to $\sim 2 \times 10^{-29} \text{ ergs s}^{-1} \text{ H}^{-1}$, across the entire density range. Consequently, the CNM is heated by a combination of UV/X-ray and photoelectric heating. At the highest densities the molecular formation rate becomes sufficiently large such that H_2 photodissociation heating dominates. The WNM is cooled by $\text{Ly}\alpha$ emission, and the CNM is cooled by [CII] $158\mu\text{m}$ fine structure emission. At high densities carbon remains neutral and [CI] $609\mu\text{m}$ fine-structure line emission dominates the cooling. The computed fractional ionizations and gas temperatures are shown in panels Figures 4c and 4d. In the WNM, $T \sim 10^4 \text{ K}$, and in the CNM, $T = 10 - 100 \text{ K}$.

In Figure 5a we display the P vs. n_{H} phase diagrams for shielding columns ranging from $1.0 \times 10^{18} \text{ cm}^{-2}$ to $1.0 \times 10^{21} \text{ cm}^{-2}$. As the shielding column increases, the ionization and heating rates decrease, and the critical pressures P_{max} and P_{min} both decrease. In Figure 5b we plot P_{min} and P_{max} as functions of the primary ionization rate, and the associated values of the shielding column. For our assumed field the ionization rate ranges from $8.9 \times 10^{-16} \text{ s}^{-1}$ to $9.1 \times 10^{-21} \text{ s}^{-1}$ for shielding columns between $1.0 \times 10^{18} \text{ cm}^{-2}$ and $3.0 \times 10^{21} \text{ cm}^{-2}$. For this range, P_{min}/k varies from 6.4×10^3 to $5.7 \text{ cm}^{-3} \text{ K}$, and P_{max}/k varies from 1.2×10^4 to $11.2 \text{ cm}^{-3} \text{ K}$.

For a fixed heating rate, P_{min} and P_{max} scale approximately as $1/Z$ (where Z is the

metallicity). This is because the fine-structure and metastable metal line cooling rates are proportional to Z , and the metal line cooling dominates at both P_{\min} and P_{\max} (see Fig. 4b).

We use the computations of $P_{\min}(\zeta_p)$ and $P_{\max}(\zeta_p)$ displayed in Figure 5b to determine the HI phase states of the gas within the halo clouds. As we have discussed, we compare the hydrostatic halo cloud pressure P to the values of P_{\min} and P_{\max} both of which vary with the local primary ionization rate within the halo clouds. When $P < P_{\min}$ the gas is WNM, when $P_{\min} < P < P_{\max}$ the gas is multi-phased, and when $P > P_{\max}$ the gas must convert to CNM.

4. Numerical Computations: M_{gas} vs. M_{vir} Diagrams

We have carried out computations of the hydrostatic gas distributions, ionization structures, and HI thermal phase properties, of dark-matter dominated clouds for a wide range of assumed total gas masses and halo masses. We consider both NFW and Burkert potentials, and a range of HIM bounding pressures. The computational results may be used to select models that fit the observed HI distributions and thermal phase properties observed in the Local Group dwarf galaxies and in the CHVCs.

In Figures 6 through 11 we display a variety of computed cloud properties as functions of the total gas mass, M_{WM} , and halo virial mass M_{vir} . We emphasize that the total gas mass M_{WM} refers to “warm gas” only, and includes the WIM and WNM, but excludes CNM. As discussed in §3, in computing the hydrostatic and ionization structures we adopt a metallicity of $0.1 Z_{\odot}$, and we assume that $T = 10^4$ K in both the WNM and the WIM. We assume irradiation by the metagalactic field. We focus on the behavior of median ($\sigma = 0$) Burkert halos and -4σ NFW halos, since as we discuss in §7, for such halos the computed gas scale heights and WNM cloud sizes correspond to those observed in Local Group dwarf galaxies. For each family of halos we display results for HIM bounding pressures, equal to 1, 10, and 100 cm^{-3} K.

The quantities shown in the M_{gas} vs. M_{vir} plots are; (a) the total cloud radius $r_{\text{W/H}}$ (kpc); (b) the total gas to DM mass ratio $M_{\text{WM}}/M_{\text{DM}}$ within $r_{\text{W/H}}$; (c) the radius r_{WNM} (kpc) of the WNM core (if present); (d) the total HI gas mass M_{HI} (M_{\odot}) contained in the WNM and WIM components; (e) the peak HI column density N_{HI} (cm^{-2}) integrated across the entire cloud diameter, and (f) the central gas pressure P_0/k (cm^{-3} K).

We recall (see §2) that for a given DM density profile (NFW or Burkert) and an assumed correlation relation, $x_{\text{vir}}(M_{\text{vir}})$, between the halo concentration $x_{\text{vir}} \equiv r_{\text{vir}}/r_s$ and the virial mass, a choice for M_{vir} uniquely determines the halo structure and scale parameters. We

consider halos with M_{vir} ranging from 10^8 to $10^{10} M_{\odot}$. For median Burkert halos this mass range corresponds to scale velocities from 12 to 50 km s⁻¹. For the -4σ NFW halos this mass range corresponds to v_s ranging from 8 to 40 km s⁻¹.

In Figures 6 through 11 the WM gas masses for which results are shown range from 5×10^6 to $5 \times 10^7 M_{\odot}$. This range was selected such that peak HI columns of 10^{19} to 10^{21} cm⁻², representative of the columns observed in the CHVCs and dwarfs, appear within the displayed M_{WM} vs. M_{vir} plots.

For the purposes of the discussion that follows we refer to halos approaching $\sim 10^8 M_{\odot}$ as “low-mass halos”, and halos approaching $\sim 10^{10} M_{\odot}$ as “high-mass halos”.

The total cloud radius $r_{\text{W/H}}$ is located at the outer edge of the WIM envelope where the cloud pressure equals the bounding pressure P_{HIM} . For fixed P_{HIM} , and a given halo mass M_{vir} , the WM cloud radius increases with increasing cloud mass M_{WM} . In low-mass halos the clouds are pressure-confined, and M_{WM} is proportional to the cloud volume, so that $r_{\text{W/H}} \sim M_{\text{WM}}^{1/3}$. The cloud radius is less sensitive to M_{WM} in high-mass halos as the clouds become gravitationally confined to approximately fixed volumes. For a given halo mass and cloud mass, the cloud radius $r_{\text{W/H}}$ decreases as P_{HIM} is increased and the clouds are pressure confined to smaller volumes.

The vertically running curve in panels b, c, and f of Figures 6 through 11 identify the locus of marginally bound clouds as defined by equation (34). Clouds to the left of this curve are unbound and gas particles with thermal energies gas can escape the halo potential wells. Clouds to the right of this curve satisfy equation (34) and are fully bound. The position of the “bounding” curve shifts towards lower virial masses as P_{HIM} increases and the WM gas is pressure-confined to the inner parts of the potential wells. For example, 10^4 K clouds in median Burkert halos, with $P_{\text{HIM}} = 10$ cm⁻³ K, are bound if $M_{\text{vir}} \gtrsim 1.5 \times 10^8 M_{\odot}$ (or $v_s \gtrsim 15$ km s⁻¹).

We define r_{WNM} as the radius at which the fractional ionization $x_e = 0.5$. This radius effectively marks the location of the ionization fronts (when present) and represents the transition point from the WIM to the WNM. In critical clouds, $r_{\text{WNM}} = 0$. Critical clouds are indicated by the dashed curves in the panels 6c through 11c. For example, for $P_{\text{HIM}} = 10$ cm⁻³ K, and a median $3 \times 10^8 M_{\odot}$ Burkert halo, a critical cloud forms for $M_{\text{WM}} = 2 \times 10^6 M_{\odot}$. Clouds to the left and below the dashed curves are fully ionized, while clouds to the right and above are predominantly neutral. For fixed M_{WM} , the clouds are ionized when M_{vir} is small since the clouds are then extended low-density objects. As M_{vir} is increased the clouds are gravitationally confined to smaller volumes, and become denser. Recombination becomes more effective, and a neutral core forms. For high-mass halos, neutral cores exist

when M_{WM} is large. However, as the WM gas mass is reduced the cloud mass finally becomes too small to maintain an optically thick WIM envelope and the cloud becomes fully ionized. As P_{HIM} is increased the clouds are compressed, and cloud neutralization occurs at smaller virial masses.

We note that gas close to $r_{\text{W/H}}$ will be undetectable since by definition the gas columns fall to zero at the cloud boundaries. The *observed* cloud sizes are better represented by the gas scale height r_{gas} , or the neutral boundary r_{WNM} . Depending on the bounding pressure, r_{gas} and r_{WNM} can be significantly smaller than $r_{\text{W/H}}$. In gravitationally confined clouds r_{WNM} is generally a few times larger than the gas scale height, which may be estimated using the analytic small- x expressions for r_{gas} (see Appendix A). E.g., for median Burkert halos, and assuming $c_{g,\text{WNM}} = 8.2 \text{ km s}^{-1}$, the analytic gas scale-height ranges from 0.3 to 0.5 kpc, for M_{vir} between 10^8 and $10^{10} M_{\odot}$. For -4σ NFW halos, r_{gas} ranges from 0.8 to 0.3 kpc. Our numerical results are consistent with these analytic estimates. In median Burkert halos, and -4σ NFW halos, r_{WNM} ranges from 0.5 to 2 kpc.

The dependence of the peak HI column density and total HI cloud mass on M_{vir} and M_{WM} can now be readily understood. In pressure-confined clouds, the gas densities are approximately constant, and the cloud volumes are proportional to the WM gas mass. Thus, $N_{\text{HI,peak}} \sim M_{\text{WM}}^{1/3}$. The pressure-confined clouds tend to be ionized when P_{HIM} is low, and the HI then exists as a small neutral fraction within the WIM dominated gas. The peak HI column is therefore small ($< 3 \times 10^{18} \text{ cm}^{-2}$) and decreases rapidly as M_{vir} decreases, since the gas then becomes more highly ionized. In ionized clouds, the total HI mass is a small fraction of the total gas mass. For example, for $P_{\text{HIM}} = 1 \text{ cm}^{-3} \text{ K}$, and a $M_{\text{vir}} = 4 \times 10^8 M_{\odot}$ median Burkert halo with $M_{\text{WM}} = 8 \times 10^5 M_{\odot}$, the neutral HI mass $M_{\text{HI}} = 10^3 M_{\odot}$, or $\sim 0.1\%$ of the total WM mass. Neutral clouds in high-mass halos are in the small- x limit with approximately constant volumes. In such clouds the neutral gas dominates the total gas mass, and $N_{\text{HI,peak}}$ is proportional to M_{WM} .

A sharp increase in $N_{\text{HI,peak}}$ is associated with the transition from ionized to neutral clouds as the halo mass increases. For critical clouds, the peak HI column density equals $3 \times 10^{18} \text{ cm}^{-2}$ for both Burkert and NFW halos, independent of M_{vir} or M_{WM} . The fact that the peak HI column density in critical clouds equals a nearly constant value of $3 \times 10^{18} \text{ cm}^{-2}$, independent of M_{vir} , is due to the weak dependence of the critical central densities, $n_{\text{H,0crit}}$, on the halo mass or scale velocity. This is also indicated analytically (see Table 6 in Appendix A). For example, for median Burkert halos, a “universal” central gas density $n_{\text{H,0crit}} \approx 5.5 \times 10^{-3} \text{ cm}^{-3}$ is associated with critical clouds, assuming a WIM sound speed $c_{g,\text{WIM}} = 11.6 \text{ km s}^{-1}$, and $J_3^* = 1$ (see Table 6). This then implies a fixed ionization rate $\zeta_{\text{crit}} = n_{\text{H,0crit}} \alpha_B = 1.4 \times 10^{-15} \text{ s}^{-1}$ at the center of critical clouds [where by definition

$n(e) = n(H)]$. Since for our assumed field the unattenuated ionization rate $\zeta_0 = 4 \times 10^{-14} \text{ s}^{-1}$, a well specified opacity is required to reduce the ionization rate to ζ_{crit} . The neutral fraction then approaches unity for clouds with peak columns exceeding 10^{19} cm^{-2} .

The condition that $M_{\text{WM}}/M_{\text{DM}} < 1$, where M_{DM} is the dark-matter mass within $r_{\text{W/M}}$, must be satisfied for self consistent dark-matter dominated solutions. This condition is met for the entire parameter space displayed in Figures 6 through 11. The ratio $M_{\text{WM}}/M_{\text{DM}}$ is smallest for low mass clouds in high mass halos. In such objects the gas is restricted to the small- x regions where the DM densities are large. A small gas mass then implies $n_{\text{H},0}/n_{\text{ds}} \ll 1$. For fixed M_{vir} , the mass ratio increases with M_{WM} . For a fixed gas mass, $M_{\text{WM}}/M_{\text{DM}}$ increases as M_{vir} becomes small, since the gas clouds then extend to large radii ($x \gg 1$) where the DM density becomes small. Thus, $M_{\text{WM}}/M_{\text{DM}}$ is largest in high-mass clouds in low-mass halos. The bound clouds are also dark-matter dominated for the range of gas masses we consider. Thus, all regions to the right of the bounding curves (indicating the marginally bound clouds) in Figures 6 through 11, represent self-consistent, dark-matter dominated, hydrostatic solutions for the WM cloud structure.

In pressure-confined clouds, the central pressure remains small and is insensitive to M_{WM} because P_0/P_{HIM} is not large in such objects. For example, for low-mass halos, with $v_s \lesssim 15 \text{ km s}^{-1}$, $P_0/k \lesssim 10 \text{ cm}^{-3} \text{ K}$, when $P_{\text{HIM}} = 1 \text{ cm}^{-3} \text{ K}$. In gravitationally confined clouds, where the cloud volumes are approximately constant, P_0 is proportional to M_{WM} and can become very large. E.g., $P_0/k \gtrsim 10^4 \text{ cm}^{-3} \text{ K}$ in high-mass halos ($v_s \gtrsim 30 \text{ km s}^{-1}$) containing $M_{\text{WM}} \gtrsim 5 \times 10^6 M_{\odot}$. In critical clouds, $P_0/k \approx 100 \text{ cm}^{-3} \text{ K}$, consistent with our analytic estimate of $n_{\text{H},0\text{crit}} \approx 5 \times 10^{-3} \text{ cm}^{-3}$, and equation (26) for the gas pressure.

We also show (in Figs. 6f-11f displaying the P_0/k contours) the regions of parameter space where the gas becomes multi-phased at the cloud centers. These regions are indicated by the narrow strip defined by the two dashed curves. On the left curve, $P_0 = P_{\text{min}}(0)$, and multi-phased gas is just possible at $r = 0$. On the right curve, $P_0 = P_{\text{max}}(0)$, and such clouds contain the largest possible multi-phased cores. Since both P_{min} and P_{max} were computed assuming heating by the external field, our results reveal the values of M_{vir} and M_{WM} for which multi-phased behavior is possible in clouds heated by the external field only. It is evident that multi-phased cores occur for values of M_{vir} and M_{WM} that are only slightly larger than those required for the transition from ionized to neutral clouds. Multi-Phased behavior occurs for clouds with peak HI column densities between 2×10^{19} and $1 \times 10^{20} \text{ cm}^{-2}$.

To the right of, or above, the multi-phased strip, we have $P_0 > P_{\text{max}}(0)$. The warm gas in the central regions of such clouds must fully convert to CNM, unless additional internal heating mechanisms are invoked to alter the local values of P_{min} and P_{max} . Thus, for a

given halo mass, the $P_0 = P_{\max}(0)$ contour delineates the maximal mass of warm gas that can exist as thermally supported WNM heated by the external field. Larger WM masses can exist only if internal heat sources drive the gas to the WNM phase. For example, for $P_{\text{HIM}}/k = 10 \text{ cm}^{-3} \text{ K}$, and a median Burkert halo with $M_{\text{vir}} = 2 \times 10^9 M_{\odot}$ the maximal WM mass is $2 \times 10^6 M_{\odot}$ (see Fig. 7f). If the gas mass is increased above this value, the heating rates at the cloud center are decreased due to the increased cloud opacity, and the gas in the core must convert to CNM. This would then drive the total mass of warm gas back to the maximum value of $2 \times 10^6 M_{\odot}$ (leading also to a reduction in the cloud opacity). More generally, if the gas becomes multi-phased, with CNM clouds that are not necessarily at the center, the total gas mass (including the CNM) can increase beyond the maximum WNM mass set by the condition $P_0 = P_{\max}(0)$. The maximal WM masses increase without limit as M_{vir} becomes small, but these clouds are unbound. For example, for *bound* clouds in median Burkert halos, with $P_{\text{HIM}}/k = 10 \text{ cm}^{-3} \text{ K}$, the largest possible WM mass is $1 \times 10^7 M_{\odot}$ (see Fig. 7f).

The region of the M_{vir} vs. M_{WM} plane within the “multi-phased strip”, and to the right of the “bounding line”, represents the region of parameter space within which acceptable models for the CHVCs may be found. In this region the WM clouds are bound to gravitationally dominant dark-matter halos, and contain neutral multi-phased cores. As we discuss further below, a key result is our finding that the location of the multi-phased strip coincides with the range of peak HI column densities observed in the CHVCs.

5. Modelling the Dwarf Galaxies Leo A and Sag DIG

Our main goal is to find halo-cloud models that provide acceptable fits to the HI properties of the CHVCs. However, to validate our approach, we first model the pressure-supported HI structures observed in the dwarf irregular (dIrr) galaxies Leo A and Sag DIG, both of which are well studied members of the Local Group. Modelling the dwarfs is an important auxiliary step because their distances are well determined, so that the true physical sizes (as opposed to just the angular sizes) of the WNM clouds are known. A specific family of halos (e.g. median, -1σ , -2σ etc.) can therefore be selected using the observed gas scale heights. We list the basic optical properties (Mateo 1998) and 21 cm HI properties (Young & Lo 1996; 1997) of Leo A and Sag DIG in Table 1.

For Leo A we adopt the recently revised distance of $690 \pm 60 \text{ kpc}$ determined by Tolstoy et al. (1998). Young & Lo (1996) assumed a much larger distance of 2.2 Mpc to Leo A based on earlier and less certain observations by Hoessel et al. (1994). For Sag DIG we adopt Mateo’s (1998) recommended distance of $1061 \pm 160 \text{ kpc}$ (also assumed by Young & Lo

1997). The total V-band luminosities and half-light core radii are $3.0 \times 10^7 L_{\odot}$ and 0.185 kpc for Leo A, and $6.9 \times 10^7 L_{\odot}$ and 0.125 kpc for Sag DIG (Mateo 1998). Both galaxies appear to have undergone several episodes of star-formation (Tolstoy et al. 1998; Cook 1988). In both Leo A and Sag DIG the measured oxygen abundances are $O/H \approx 2 \times 10^{-5}$, implying low metallicities $Z \approx 0.07Z_{\odot}$ (Skillman, Kennicutt & Hodge 1989; Skillman, Terlevich & Melnick 1989).

Young & Lo (1996) carried out high resolution (15'') interferometric VLA 21 cm observations of Leo A. They found that the optical galaxy is surrounded by a much larger 2.8×1.7 kpc envelope of HI gas. The total VLA 21 cm flux is 65 ± 3 Jy km s⁻¹, just about equal to the single-dish (43-meter Green Bank) flux of 69 ± 3 Jy km s⁻¹, implying that the interferometer detected all of the HI emission. The total HI mass is $7.9 \times 10^6 M_{\odot}$ (for $d = 690$ kpc). The peak HI column density is 2.7×10^{21} cm⁻², and emission was detected down to a minimum HI column of $N_{\text{HI,min}} \sim 2 \times 10^{19}$ cm⁻², at a (mean) radius of $r(N_{\text{HI,min}}) = 1.2$ kpc from the galaxy center. A key finding of the Young & Lo study is that the global line profile can be separated into broad (9.6 ± 0.2 km s⁻¹) and narrow (5.2 ± 0.3 km s⁻¹) components. The broad (WNM) component contains 80% of the flux and is produced throughout the HI image, whereas the narrow (CNM) component is localized near isolated star-forming regions within the optical galaxy. In view of these observations we set $N_{\text{HI,peak}} = 2.2 \times 10^{21}$ cm⁻² for the WNM distribution in Leo A.

In their VLA study of Sag DIG, Young & Lo (1997) discovered a similar 3.3×3.0 kpc HI envelope surrounding the much smaller optical image. The VLA flux is 30.3 ± 1.5 Jy km s⁻¹, close to the single dish flux of 32.6 ± 1.2 Jy km s⁻¹. The total implied HI mass (for $d = 1.1$ Mpc) is $9.3 \times 10^6 M_{\odot}$. The HI structure in Sag DIG is somewhat more complex than in Leo A, and appears as an asymmetric ring with several clumps of high column density gas near the optical galaxy. The peak column density is 1.2×10^{21} cm⁻², and emission was detected down to $N_{\text{HI,min}} = 5 \times 10^{18}$ cm⁻², at $r_{\text{HI,min}} = 1.6$ kpc from the galaxy center. The Sag DIG HI line profile can also be decomposed into extended broad WNM (9-10 km s⁻¹) and localized narrow CNM (4-6 km s⁻¹) components. Young & Lo find that 83% of the total flux is contained in the WNM component. Thus, $N_{\text{HI,peak}} = 1.0 \times 10^{21}$ cm⁻² for the WNM in Sag DIG

Given the interferometric HI maps (Fig. 1 in Young & Lo 1996, and Fig. 3 in Young & Lo 1997) it is possible to determine the (projected) 1/e gas scale heights for Leo A and Sag DIG. In Leo A, averaging over the long and short axes, the *projected* angular scale height is $\theta_{\text{gas}} \approx 160$ arcsec, corresponding to a projected gas scale height of 0.5 kpc for a distance of 690 kpc. Determining a gas scale height for Sag DIG is more complicated due to the inhomogeneities in the HI emission. However, based on the Young & Lo (1997) map we

estimate that $\theta_{\text{gas}} \approx 70$ arcsec, implying a projected scale height ~ 0.4 kpc. It is significant that we find comparable scale heights for Leo A and Sag DIG.

Can a DM halo model be found, that reproduces (a) the total extents of the HI clouds, (b) the observed $1/e$ gas scale heights, and (c) the peak WNM HI column densities, assuming photoionization by the metagalactic field? What is the maximum possible Local Group HIM pressure that is consistent with the dwarf galaxy observations?

For the dwarf galaxies we adopt a representative projected gas scale height of 0.5 kpc, and a WNM velocity dispersion of 9 km s^{-1} . The observed velocity dispersion is consistent with $\sim 10^4$ K gas. Crucially, the observed scale height effectively determines the relative concentration of the DM halo, since as is indicated by our analytic expressions for r_{gas} (see Table 6, and Figs. 16 and 17, in Appendix A) the intrinsic scale height r_{gas} is weakly dependent on the halo scale velocity. Thus, the observed scale height may be used to select an appropriate value of σ for the dwarf galaxy halos. In particular, it is clear that if the dwarfs are embedded in NFW halos, these halos must be significantly underconcentrated, with $\sigma \approx -4$ relative to the (theoretical) Λ CDM $x_{\text{vir}}(M_{\text{vir}})$ relation for median halos as specified by equation (15). In contrast, *median* Burkert halos will produce scale heights very close to those observed in the dwarfs. It is also evident from our M_{vir} vs. M_{WNM} computations (Figs. 6-11) for median Burkert halos and -4σ NFW halos, that $r_{\text{WNM}} \approx 1$ to 2 kpc for HI gas column densities $\sim 10^{21} \text{ cm}^{-2}$, consistent with the observed cloud sizes and peak HI column densities. These results guide the choice of appropriate dwarf DM halo models.

However, a complication arises in that the *optical* galaxies do not appear to be dark-matter dominated. In Leo A and Sag DIG, $(M/L_V)_{\odot} \approx 3.5$ and 1.4 within the optical radii (Mateo 1998). These mass-to-light ratios are within the range expected for evolved stellar systems (e.g. Bruzual & Charlot 1993; Sternberg 1998), and are, for example, much smaller than observed in the dark-matter dominated dwarf-spheroidals Ursa Minor and Draco where $(M/L_V)_{\odot} \sim 80$ (Aaronson 1983; Gallagher 1994).

Thus, in modelling the hydrostatic HI gas distributions in Leo A and Sag DIG we consider the possibility that stars contribute to the gravitational potential. We make the simplifying approximation that the total gravitational potential is the sum

$$\varphi = \varphi_{\text{DM}} + \varphi_{*} \quad (35)$$

of (independent) DM and stellar potentials. For the stellar potential φ_{*} we adopt a Plummer model (see Spitzer 1987). In this model the enclosed stellar mass

$$M_{*}(y) = M_{s*} \frac{y^3}{(1 + y^2)^{3/2}} \equiv M_{s*} f_{M*}(y) \quad , \quad (36)$$

where $y \equiv r/r_{s*}$, and where r_{s*} is the scale radius of the stellar density distribution, and M_{s*} is the total stellar mass. We assume that r_{s*} is equal to the observed (projected) half-light core radius¹⁴, and we fix the total stellar mass assuming $(M/L_V)_\odot = 1$. As representative values for Leo A and Sag DIG we set $r_{s*} = 0.185$ kpc and $M_{s*} = 3 \times 10^6 M_\odot$ (Mateo 1998).

We augment the equation of hydrostatic equilibrium to include the stellar mass. Expression (21) for the gas pressure $P(x)$ becomes

$$P(x) = P_0 \exp \left\{ - \int_0^x \frac{v_s^2}{c_g^2} \left[\frac{f_M(x')}{x'^2} + \frac{M_{s*}}{M_{ds}} \frac{f_{M*}(r_s x'/r_{s*})}{x'^2} \right] dx' \right\} \quad (37)$$

where $x = r/r_s$ is the radius in units of the DM halo scale radius r_s , and M_{ds} is the halo scale mass.

In Figure 12 we show a specific gravitationally confined model for the dwarfs, in which we combine a stellar system (with $r_{s*} = 0.185$ kpc, and $M_{s*} = 3 \times 10^6 M_\odot$) with a median Burkert halo with a scale velocity $v_s = 30.0$ km s⁻¹ corresponding to $M_{\text{vir}} = 2.0 \times 10^9 M_\odot$. We assume a low bounding pressure and set $P_{\text{HIM}} = 1$ cm⁻³ K. A good fit is obtained for a total gas mass $M_{\text{WM}} = 2.2 \times 10^7 M_\odot$. Additional model parameters are listed in Table 2.

In this model the combined stellar and DM mass dominates the enclosed mass at all radii. The stellar component (i.e. the optical galaxy) dominates out to the stellar core radius of 0.2 kpc. At larger radii the DM halo dominates the mass. The WM cloud consists of a WNM core with $r_{\text{WNM}} = 1.4$ kpc, surrounded by a WIM envelope extending to $r_{\text{W/H}} = 4.4$ kpc. The WM cloud satisfies equation (34) and is bound. The total HI mass equals $1.3 \times 10^7 M_\odot$, or 61% of the total hydrogen mass. Virtually all of the HI mass is contained within r_{WNM} . The computed peak HI column density is 1.4×10^{21} cm⁻², consistent with the observed peak WNM column densities. The computed $1/e$ scale height for the projected HI column density distribution is $r_{\text{NHI}} = 0.6$ kpc, in good agreement with the observed scale heights of 0.5 kpc.

The HI column falls sharply near $r_{\text{WNM}} = 1.4$ kpc. The HI column decreases from 2×10^{19} to 1×10^{18} cm⁻², between 1.3 and 1.5 kpc. The sharp decline in the HI column densities that occurs between 10^{19} and 10^{18} cm⁻² is a general feature of the computed gas distributions, for both Burkert and NFW potentials, and is due to the photoionization cut-off of the HI gas density distribution. The cut-off column of $\sim 10^{19}$ cm⁻² is similar to those predicted for flattened, rotationally supported, disk systems (e.g. Corbelli & Salpeter 1993; Maloney 1993). The radius at which this cut-off occurs is insensitive to the intensity of the

¹⁴For many stellar density distributions, including the Plummer model, the projected half-mass radius $r_{hp} = 0.77r_h$, where r_h is the half-mass radius. For the Plummer distribution $r_h = 1.3r_{s*}$. Thus, $r_{s*} \simeq r_{hp}$ (Spitzer 1987).

ionizing radiation field because the ionization front is located at a radius where the total gas density is decreasing exponentially.

For Leo A we are essentially able to reproduce $r_{\text{HImin}} = 1.2$ kpc for $N_{\text{HImin}} = 2 \times 10^{19}$ cm^{-2} as found by Young & Lo in Leo A. In our interpretation this observational cut-off radius is very close to r_{WNM} , and corresponds to the location of the ionization front. However, if in Sag DIG the neutral boundary also occurs near 1.24 kpc, we are unable to account for the column of 5×10^{18} cm^{-2} reported by Young & Lo at the significantly larger radius of 1.6 kpc. In our model we predict a column of only 6×10^{17} cm^{-2} at this radius. As we discuss in §6, we encounter a similar difficulty in fitting the extended low column density distributions in the CHVCs.

In Figure 12d we plot the H α recombination line surface brightness $I_{\text{H}\alpha}$ as a function of cloud radius. The H α emission is produced in the outer WIM envelope, and the computed surface brightness includes the equal contributions from both sides of cloud. At the cloud center $I_{\text{H}\alpha} = 4.3$ mR. The surface brightness rises to 8 mR near r_{WNM} due to limb-brightening, and then declines rapidly as the projected columns of ionized gas become small.

The HI mass in our model clearly exceeds the maximum WNM mass, of about $5 \times 10^5 M_{\odot}$, (see Fig. 6f) that can be maintained by the metagalactic field. This fact is indicated by the P_{min} and P_{max} curves (shown in Fig. 12e) that were computed assuming heating and ionization by the external field. It is evident that $P > P_{\text{max}}$ within 0.9 kpc. The central pressure $P_0/k = 6.0 \times 10^3$ cm^{-3} K (corresponding to a gas density $n_0 = 0.5$ cm^{-3}) is much greater than $P_{\text{max}}(0)/k = 71.5$ cm^{-3} K. Thus, our model for the WNM in the dwarf galaxies implicitly assumes that additional heat sources (presumably associated with the optical components) are available to produce the observed mass of warm HI in these objects. We note that the computed P_{min} and P_{max} are coupled to the ionization rate which declines with increasing cloud opacity. Figure 12f shows that the total hydrogen ionization rate decreases from the unattenuated optically thin value of 4.0×10^{-14} s^{-1} at the cloud edge, to 1.0×10^{-18} s^{-1} in the optically thick core. At $r = 0$ the total ionization rate is 10 times larger than the primary rate, due to the dominating effect of secondary ionizations (which are negligible in the ionized envelopes).

The model displayed in Figure 18 is representative. As is indicated by the parameter-space study presented in §4, acceptable models for the dwarf galaxy halos can be found for other values of M_{vir} , M_{WM} and P_{HIM} , and for (underconcentrated) NFW halos rather than Burkert halos. It is evident from Figures 6e and 9e that for a low bounding pressure ($P_{\text{HIM}}/k = 1$ cm^{-3} K) acceptable solutions require $v_s \gtrsim 25$ km s^{-1} . In such halos, as in our particular model, the WNM and WIM components are gravitationally confined. If larger bounding pressures are assumed (e.g. $P_{\text{HIM}}/k = 100$ cm^{-3}) lower values of v_s are allowed.

We note that for our model, the effect of increasing P_{HIM} is simply to truncate the outer part of the WM cloud at the radius where P_{gas} equals the increased value of P_{HIM} . The inner part remains largely unaffected by the truncation. For example, if the bounding pressure is increased from 1 to $100 \text{ cm}^{-3} \text{ s}^{-1}$, then the WM cloud boundary moves inwards to $r_{\text{W/H}} \approx 1.3$ kpc. Most of the tenuous WIM mass is removed, but the inner neutral core is preserved. However, if P_{HIM} is increased above $\sim 100 \text{ cm}^{-3} \text{ K}$, the neutral core is also truncated, and its size shrinks below the observed values. We conclude that the dwarf galaxy HI structures are consistent with an upper-limit of $P_{\text{HIM}}/k \approx 100 \text{ cm}^{-3} \text{ K}$ for the intergalactic medium in the Local Group.

Our model fit demonstrates that the observed extended neutral HI clouds in Leo A and Sag DIG may be readily interpreted as dark-matter dominated, pressure-supported gas clouds (although we may have difficulty in accounting for extended HI at a level $\lesssim 5 \times 10^{18} \text{ cm}^{-2}$). In our model, the central gas density $n_{\text{H},0} = 0.46 \text{ cm}^{-3}$ is much larger than the central gas density of $n_{\text{H},0\text{crit}} = 5 \times 10^{-3} \text{ cm}^{-3}$ in critical clouds, and is sufficiently large to keep the gas cloud neutral against the metagalactic radiation field out to $\gtrsim 1$ kpc. The characteristic (or central) DM density in our model is $n_{\text{ds}} = 1.24 \text{ cm}^{-3}$ (or $3.1 \times 10^{-2} M_{\odot} \text{ pc}^{-3}$), in excellent agreement with the typical central DM densities of $2.0 \times 10^{-2} M_{\odot} \text{ pc}^{-3}$ found in HI rotation curve studies of rotationally supported dwarfs and low surface brightness galaxies (de Blok & McGaugh 1997; Firmani et al. 2000; de Blok, McGaugh & Rubin 2001). Finally, we note that while both NFW and Burkert halos may be found that fit the dwarf galaxy observations, the Burkert solutions require median halos with “typical” dark-matter concentration parameters (in our model $x_{\text{vir}} = 25.6$). However, NFW solutions are problematic in that they must be extremely underconcentrated, by $\sim -4\sigma$ relative to the $\Lambda\text{CDM } x_{\text{vir}}(M_{\text{vir}})$ relation, to match the observed scale heights in the dwarf galaxies.

6. Modelling the CHVCs

We have demonstrated that mini-halo models can be constructed for the HI distributions in the dwarf galaxies Leo A and Sag DIG. Can similar models be found for the CHVCs? Here, we focus on the HI properties of the CHVCs as most recently probed by the high resolution single dish observations and interferometric observations presented by Braun & Burton (2000) and Burton et al. (2001) (see also Brüns et al. 2001; Putman et al. 2002).

In their Arecibo observations, Burton et al. (2001) were able to resolve the WNM HI gas distributions in a sample of ten CHVCs. They constructed $1^{\circ} \times 1^{\circ}$ sized maps of each object at a spatial resolution of 3.1×3.7 arcmin, and determined the locations of the peak HI flux concentrations. They then carried out deep integration “cross-cut” observations to

study the detailed gas distributions around the central peaks. Burton et al. found that the peak WNM HI column densities range from 2×10^{19} to 2×10^{20} cm^{-2} , and that the projected $1/e$ scale-lengths of the inner parts of the clouds range from 412 to 908 arcsec, with a typical value of 690 arcsec. It is significant that the peak HI columns in the CHVCs are much smaller than those observed in Leo A and Sag DIG. In their cross-cut observations, Burton et al. detected gas down to column densities of $\sim 2 \times 10^{17}$ cm^{-2} (corresponding to the 1σ sensitivity limit). In some cases low column density “wings” extend out to $\sim 1^\circ$ from the cloud centers. In some clouds the HI gas distributions are quite asymmetric, with emission at a level of 10^{18} cm^{-2} persisting out to several gas scale heights on one side of the emission peak, with a more rapid decline on the opposite side. The asymmetries could be due to the presence of head-tail structures as observed by Brüns et al (2001) in CHVC 125+41-207, or to an imprecise positioning of the emission centroids. Burton et al. argued that intrinsically exponential gas density distributions (but observed in projection) provide a reasonable description of the data, although significant departures from this simple density law are clearly present. Burton et al. also found that the velocity gradients across the clouds are relatively small (~ 10 km s^{-1} degree^{-1}) implying that rotation is not dynamically important in supporting the WNM clouds.

CNM cores were detected by Braun & Burton (2000) and de Heij et al. (2002c) in 11 CHVCs (including two that were subsequently observed at Arecibo) in high resolution Westerbork interferometric observations. These observations revealed the presence of high column density (up to $\sim 10^{21}$ cm^{-2}) cores displaying narrow ($2 - 15$ km s^{-1} FWHM) HI line profiles. The narrow linewidth emission clearly traces a CNM component, and typically contributes $\sim 30\%$ of the total CHVC HI luminosity. Rotation may be important in the cores, where velocity gradients are ~ 1 km s^{-1} arcmin^{-1} . The radii of the CNM cores range from 5 to 17 arcmin, with an average value of 10 arcmin. It is significant that the CNM core sizes are comparable to the WNM gas scale heights.

Given these observational results we adopt the following properties as “typical” for an individual CHVC, and which should be reproduced in any successful model for the CHVCs; (1) a peak WNM HI column of 5×10^{19} cm^{-2} , (2) a projected ($1/e$) WNM gas scale height of 690 arcsec for an assumed distance d , (3) HI columns of $\sim 1 \times 10^{18}$ cm^{-2} extending to ~ 3 scale heights, and (4) a multi-phased core region with projected radius equal to or slightly smaller than the gas scale height. Properties (1)-(3) are similar to those that fix the dwarf halos, with the critical difference that the distances to the CHVCs are not known a priori. Property (4) provides an additional constraint, since we wish to construct models in which the multi-phased cores arise in gas heated exclusively by the metagalactic field. We will find that minihalo models can be constructed that readily reproduce properties (1), (2) and (4), while we have difficulty in accounting for property (3).

The total number of CHVCs is also an important constraint. We recall that de Heij et al. (2002b) identified 67 CHVCs within the Leiden-Dwingeloo survey, and that Putman et al. (2002) found an additional 179 CHVCs in their Parkes HI survey, giving a total of 246 objects. If the CHVCs represent “missing satellites” associated with either the Local Group (Blitz et al. 1999), or with the Milky Way (Klypin et al. 1999), then the total number of objects should be related to the typical mass of the CHVC mini-halos. The numerical simulations of halo evolution predict that the number of embedded dark-matter sub-halos contained within any given parent halo increases rapidly with decreasing sub-halo mass (Klypin et al. 1999; Moore et al. 1999). As a guide to this predicted behavior we adopt the results of Klypin et al. for their Λ CDM simulation of the Local Group. In their computations two massive halos are produced, representing the Milky Way and M31. Each massive object contains a large number of embedded sub-halos. Klypin et al. find that the number density of sub-halos is proportional to $v_s^{-2.75}$, where v_s is the sub-halo scale velocity¹⁵. They also find that for a given v_s , the volume density of objects decreases as $\sim 1/d^2$, where d is the distance from the center of the parent halo. We reexpress the results of Klypin et al. (their eq. [3] and [4]) as

$$\mathcal{N}(> v_s, < d) = 1.06 \times 10^3 \left(\frac{M_{\text{vir,p}}}{10^{12} M_\odot} \right) \left(\frac{v_s}{10 \text{ km s}^{-1}} \right)^{-2.75} \left(\frac{d}{1 \text{ Mpc}} \right)^{-2}, \quad (38)$$

where $\mathcal{N}(> v_s, < d)$ is the total number of sub-halos with scale velocities greater than v_s , contained within a distance d from the center of a parent halo with virial mass $M_{\text{vir,p}}$.

With the above observational and theoretical facts in mind, we now consider two basic “scenarios” for the CHVCs. We first consider the CHVCs as “circumgalactic” objects associated with the Milky Way halo. In this scenario the characteristic distance to the CHVCs is ~ 150 kpc. We then consider the possibility that the CHVCs are more distant ($d \gtrsim 750$ kpc) “extragalactic” Local Group objects as proposed by Blitz et al. (1999). As we will show, minihalo models for the CHVCs can be constructed for both scenarios, but our analysis strongly favors the circumgalactic model.

6.1. CHVCs as Circumgalactic Minihalos

Circumgalactic distances for the CHVCs arise naturally if the CHVC halos are drawn from the same family of median Burkert halos (or -4σ NFW halos) that successfully reproduce the dwarf galaxy observations. If the CHVC halos are not significantly over- or

¹⁵We note that Klypin et al. present their results in terms of the maximum circular velocities, v_{max} , of the subhalos. We recall that for NFW and Burkert profiles $v_{\text{max}} = 0.8v_s$.

under-concentrated with respect to the dwarf halos, the gas scale heights in the CHVCs and in the dwarfs must be comparable, since the scale heights are insensitive to the halo mass (see the expressions for r_{gas} in Table 6, and Figures 16 and 17, in Appendix A). If the scale-heights are in fact comparable, then the CHVCs must be significantly closer to the Milky Way than Leo A or Sag DIG. This is because the $1/e$ angular sizes of the dwarfs (160 and 70 arcsec) as observed by Young & Lo are significantly smaller than the angular scale heights (690 arcsec) of the CHVCs as observed by Burton et al. Given the known distances to the dwarfs, the larger CHVC angular scale heights place the CHVCs at distances of 100 to 200 kpc. At $d = 150$ kpc, 690 arcsec corresponds to a linear scale of 0.5 kpc.

The M_{WM} vs. M_{vir} computations displayed in Figures 6 through 11 show that in clouds heated by the metagalactic field, multi-phased cores exist for peak HI column between 2×10^{19} to $1 \times 10^{20} \text{ cm}^{-2}$. The fact that multi-phased cores are predicted for the range of peak WNM column densities observed in the CHVCs strongly suggests that the thermal states of the CHVCs are controlled by the external field. For a distance of 150 kpc the external field may already be dominated by the metagalactic background with a possible (though uncertain) contribution from Galactic stellar Lyc photons (see Appendix B). For those models with multi-phased cores (i.e., those within the “multi-phased strip” in Figs. 6f through 11f) the boundaries of the WNM clouds are predicted to occur at $r_{\text{WNM}} \approx 0.6$ kpc. It is evident that many such halo “solutions” for the CHVC behavior can be found for a wide range of halo masses and bounding pressures. For example, for $P_{\text{HIM}}/k = 10 \text{ cm}^{-3} \text{ K}$, bound cloud models can be constructed for $v_s > 17 \text{ km s}^{-1}$ (see Fig. 7) in Burkert halos. Clearly, however, gravitationally confined solutions in very massive halos (e.g., setting $M_{\text{vir}} = 10^{10} M_{\odot}$, with $M_{\text{WM}} = 10^6 M_{\odot}$) are not relevant, since ~ 200 such objects would exceed the total mass of the Milky Way.

In fact, the large number of CHVCs suggests that they must be pressure-confined in low-mass halos. For example, if half of the CHVCs lie within the characteristic distance d , then it follows from equation (38) that the CHVC halos must be low-mass objects. In particular, for scale velocities $v_s \sim 12 \text{ km s}^{-1}$, $\mathcal{N}(> v_s) = 100$ within $d = 150$ kpc, where we have assumed $M_{\text{vir,p}} = 10^{12} M_{\odot}$ for the Milky Way (see below). Such low scale velocities require large confining HIM pressures to keep the gas both neutral and bound to the halos.

As a specific example of such a pressure-confined solution, we consider a median Burkert halo with $v_s = 12 \text{ km s}^{-1}$. For this choice $M_{\text{vir}} = 1 \times 10^8 M_{\odot}$. We set $P_{\text{HIM}}/k = 50 \text{ cm}^{-3} \text{ K}$, which is the minimum possible bounding pressure that allows 10^4 K WM gas to remain bound to such halos. We fix $M_{\text{WM}} = 1.1 \times 10^6 M_{\odot}$ in order to produce a peak HI column within the range of observed values. For this gas mass, the baryon to DM mass ratio for the mini-halos is $M_{\text{WM}}/M_{\text{vir}} = 1.1 \times 10^{-2}$, and is significantly smaller than the cosmic baryon

fraction $\Omega_b/\Omega_m = 0.09$. The resulting model structure is displayed in Figure 13, and the various model parameters are summarized in Table 3.

The WM cloud consists of a WNM core with $r_{\text{WNM}} = 0.67$ kpc, surrounded by a WIM envelope extending to $r_{\text{W/H}} = 1.3$ kpc. The gas at $r_{\text{W/H}}$ is marginally bound with $\mathcal{W}/\mathcal{T}=1.0$ at the cloud edge (a condition fixed by our choice for P_{HIM}). The central gas density $n_{\text{H},0} = 2.1 \times 10^{-2} \text{ cm}^{-3}$, and is sufficiently large for the formation of a neutral core. The computed HI mass is $2.8 \times 10^5 M_\odot$, or about 20% of the total WM mass.

The computed peak HI column is $5.1 \times 10^{19} \text{ cm}^{-2}$. The HI column falls to $1/e$ of the central value at $r_{\text{NHI}} = 0.50$ kpc. For an angular $1/e$ size of 690 arcsec the implied distance is $d = 150$ kpc. The pressure contrast $P_0/P_{\text{HIM}} = 4.7$, so that $P_0/k = 235 \text{ cm}^{-3} \text{ K}$. The central pressure satisfies the condition $P_{\text{min}}(0) < P_0 < P_{\text{max}}(0)$, where $P_{\text{min}}(0)/k = 95$ and $P_{\text{max}}(0)/k = 730 \text{ cm}^{-3} \text{ K}$. A multi-phased medium is possible out to 0.33 kpc, at which point $P = P_{\text{min}}$. A multi-phased core of this size is also consistent with the observations (again assuming $d \approx 150$ kpc). For radii greater than 0.33 kpc, the local gas pressure P falls below the local values of P_{min} and the neutral gas must be entirely in the WNM phase.

We note that for a distance of 150 kpc, clouds in median $v_s = 12 \text{ km s}^{-1}$ NFW halos (as opposed to Burkert halos) would be much smaller than observed. In such systems the projected scale height is only 0.2 kpc. In the circumgalactic model, $v_s = 12 \text{ km s}^{-1}$ NFW halos would have to be significantly underconcentrated, with $\sigma \approx -2$, to give clouds with projected scale heights of 0.5 kpc.

An important prediction of the model displayed in Figure 13 is the presence of a sharp drop in the HI column at r_{WNM} . As in the case of our dwarf galaxy models, the ionization front is located near the radius where the projected column falls to 10^{19} cm^{-2} . In our CHVC model $N_{\text{HI}} = 5 \times 10^{18} \text{ cm}^{-2}$ at $r_{\text{WNM}} = 0.7$ kpc, and decreases below $1 \times 10^{18} \text{ cm}^{-2}$ at 0.8 kpc. We note that in the CHVC model $r_{\text{WNM}}/r_{\text{gas}} = 1.2$, whereas in our dwarf galaxy model $r_{\text{WNM}}/r_{\text{gas}} = 2.5$. This difference is due to the significantly larger HI gas mass, and associated peak HI column, in the dwarf compared to the CHVC.

At this point we encounter a difficulty in accounting for the extended HI gas “wings” found by Burton et al. (2001), in at least some of the CHVCs that they observed. To illustrate this difficulty, we plot in Figure 13b (as the dashed curve) the projected HI column density distribution assuming that the intrinsic HI gas density profile varies as a pure exponential out to several scale heights. We recall that Burton et al. suggested that such exponentials are representative of the observed gas distributions. We normalize the exponential distribution such that the peak HI column density and the projected $1/e$ scale height are equal to those in our CHVC model. In our model, the HI column density decreases to a value

of 10^{18} cm^{-2} at 1.2 (projected) scale heights, whereas for the pure exponential distribution the HI column falls to 10^{18} cm^{-2} at 4 scale heights. Thus, if an exponential density law represents the observations down to columns of 10^{18} cm^{-2} , then the photoionization feature expected near a column of 10^{19} cm^{-2} would appear to be absent in the data ¹⁶. We caution however, that the exponential forms proposed by Burton et al. are only approximate representations. In fact, in some objects (e.g. in the CHVCs 186-31-206 and 230+61+165; see their Fig. 11) features that resemble our predicted photoionization cutoffs may be present.

As is indicated by Figure 13d the predicted H α surface brightness ranges from 4.3 mR at the cloud center, to a maximum limb-brightened value of 6.6 mR at a projected radius of 0.7 kpc from the cloud center. The predicted H α surface brightnesses of the CHVCs and dwarf galaxies are equal because both cloud systems are optically thick. The predicted surface brightness is proportional to our assumed metagalactic field intensity, and is consistent with the expectation that in optically thick clouds the emission measure along a cloud diameter equals $2\pi J^*/\alpha_B$ (plus an additional contribution due to the secondary ionizations). Direct measurements of the H α fluxes from the population of CHVCs are largely unavailable. However, Weiner et al. (2001) and Tufte et al. (2002) report H α intensities of 20 to 140 mR in five CHVCs. These values are considerably larger than our predicted surface brightnesses. We consider it unlikely that the metagalactic Lyc field is more than ~ 3 times greater than our estimated strength, and additional sources of ionization appear to be required. Galactic radiation could contribute if these particular objects are considerably closer to the Galaxy than 150 kpc. Collisional ionization at the interfaces between the clouds and a dense HIM is another possibility. Further observations are required to determine whether the fluxes found by Weiner et al. and Tufte et al. are typical of the entire population of CHVCs.

For $v_s = 12 \text{ km s}^{-1}$ halos, neutral bound clouds require large bounding pressures, with $P_{\text{HIM}}/k \gtrsim 50 \text{ cm}^{-3} \text{ K}$ at distances of $\sim 150 \text{ kpc}$ from the Galaxy. We now argue that such pressures could plausibly be provided by a hot ($T_{\text{HIM}} \sim 2 \times 10^6 \text{ K}$) Galactic corona. To demonstrate this we construct a simple hydrostatic model for a corona within the Galactic potential. We model the Galactic potential as the combination

$$\varphi_{\text{Gal}} = \varphi_{\text{disk}} + \varphi_{\text{DM}} \tag{39}$$

of a baryonic disk and a dark-matter halo. The coronal HIM pressure at a distance d is then

¹⁶We remark that purely exponential gas density distributions are expected in NFW halos in the small- x limit (see Appendix A). However, this requires massive halos. Furthermore, eliminating the photoionization cutoff to a column below 10^{18} would require reducing our estimate for the metagalactic Lyc flux (for photons between 1 and $\sim 2 \text{ ryd}$) by a factor of at least $\sim 10^3$.

given by

$$P_{\text{HIM}} = P_{\text{mid}} e^{[\varphi_{\text{Gal}}(0) - \varphi_{\text{Gal}}(d)]/c_{\text{HIM}}^2} \quad (40)$$

where P_{mid} is the mid-plane thermal pressure, and $c_{\text{HIM}} = 116T_6^{1/2}$ km s⁻¹ is the HIM sound speed (where $T_6 \equiv T/10^6$ K). For the disk we assume a cylindrical (R, z) Miyamoto-Nagai potential

$$\varphi_{\text{disk}} = -\frac{C_1 v_{\text{circ}}^2}{[R^2 + (a_1 + \sqrt{z^2 + b_1^2})^2]^{1/2}} \quad (41)$$

where we set $C_1 = 8.887$ kpc, $v_{\text{circ}} = 225$ km s⁻¹, $a_1 = 6.5$ kpc, and $b_1 = 0.26$ kpc (Wolfire et al. 1995b). In using this expression we fix R to a constant value of 8.5 kpc. At large distances from the disk, $z/R \gg 1$, and $z \approx d$ where d is the distance from the Galactic center. For the DM halo we adopt a median Burkert halo with $M_{\text{vir}} = 10^{12} M_{\odot}$. The associated halo parameters are $x_{\text{vir}} = 13.9$, $r_s = 18.6$ kpc, $n_{ds} = 0.26$ amu cm⁻³, and $v_s = 200$ km s⁻². The virial radius is $r_{\text{vir}} = 258$ kpc, and the circular velocity at the virial radius $v_{\text{vir}} = 129$ km s⁻¹. Our model for the Galactic DM halo is very similar to the model presented by Moore et al. (2001). It satisfies the requirements (e.g. Navarro & Steinmetz 2000) that (a) the disk mass, $M_{\text{disk}} \lesssim 10^{11} M_{\odot}$, is consistent with the mass of baryons that could have cooled out of the Galactic DM halo, i.e., the requirement that $M_{\text{disk}} \lesssim (\Omega_b/\Omega_m)M_{\text{vir}}$ (where $\Omega_b/\Omega_m = 0.09$), and (b) the dark matter mass within 10 kpc ($1.8 \times 10^{10} M_{\odot}$) is less than the upper limit of $\sim 3 \times 10^{10} M_{\odot}$ inferred from Galaxy mass models (Dehnen & Binney 1998). Following Wolfire et al. (1995b), we fix the mid-plane pressure such that the coronal HIM produces a total X-ray emission measure of 5×10^{-3} cm⁻⁶ pc (Garmire et al. 1992; Kuntz & Snowden 2000). For a coronal HIM temperature of 2×10^6 K (corresponding to $c_{g,\text{HIM}} = 164$ km s⁻¹) we find that $P_{\text{mid}}/k = 2.5 \times 10^3$ cm⁻³ K, consistent with the observed mid-plane thermal pressures. The total mass of hot coronal gas equals $2.5 \times 10^{10} M_{\odot}$, and is a significant fraction of the baryonic mass of the Galaxy. In Figure 14 we display the resulting coronal pressure as a function of the distance d . It is evident that P_{HIM} remains large beyond 100 kpc, and ranges from 99 to 43 cm⁻³ K between 100 and 260 kpc. These pressures are sufficiently large to confine and neutralize the gas contained within a population of low-mass minihalos located in the circumgalactic environment.

We emphasize that the coronal HIM pressure maintains the WM gas within the low-mass halos in neutral form, and therefore visible as 21 cm sources. If, for example, our $v_s = 12.5$ km s⁻¹ mini-halo containing $1.1 \times 10^6 M_{\odot}$ of gas is moved out to larger distances where the enveloping HIM pressure is presumably significantly reduced, the cloud expands and becomes ionized. Thus, if the CHVCs are infalling objects, a picture emerges in which a population of low-mass halos could exist beyond the immediate circumgalactic environment, but would be ionized by the metagalactic field and therefore remain invisible as HI sources. It is possible that such objects could be detected via absorption line studies of ionized gas

tracers (e.g. Sembach et al. 1999). As such objects approach the higher pressure environment of the Galaxy the clouds are compressed and neutralized, and become visible HI sources.

A distance of $d = 150$ kpc is likely well within the virial radius of Galactic DM halo (for our Galaxy model, $r_{\text{vir}} = 260$ kpc). Our model CHVC mini-halo must therefore be tidally truncated at a radius that is smaller than the (original) mini-halo virial radius. What is the tidal truncation radius at 150 kpc? Assuming the CHVC is on a circular orbit at a distance d around the Milky Way, the truncation radius r_t is set by the tidal criterion $3\bar{n}_{\text{MW}}(d) = \bar{n}_{\text{CHVC}}(r_t)$ where $\bar{n}_{\text{MW}}(d)$ is the mean density of the Galaxy within d , and $\bar{n}_{\text{CHVC}}(r_t)$ is the mean DM density of the CHVC halo within r_t . For our Galaxy model, $3\bar{n}_{\text{MW}} = 2.4 \times 10^{-3} \text{ cm}^{-3}$ at 150 kpc. For our $v_s = 12 \text{ km s}^{-1}$ minihalo, the implied tidal radius $r_t = 6.8$ kpc, well within the mini-halo virial radius of 12.0 kpc. However, r_t is still significantly larger than the WM cloud radius $r_{\text{W/H}} = 1.3$ kpc set by the confining HIM pressure. The actual truncation radius will depend on the orbital parameters, and could be significantly smaller than our estimate if the periastron distances are sufficiently small. If the CHVCs come too close to the Galaxy, they will be tidally disrupted. As we now discuss, they may also be destroyed by ram-pressure stripping.

While low-mass halos require a large HIM pressure to keep the gas bound and neutral, if the HIM becomes too dense the CHVC gas will be ram-pressure stripped out of the mini-halos. Stripping occurs when the ram-pressure exceeds the gravitational force per unit area on the gas (Gunn & Gott 1972; Blitz & Robishaw 2000; Mori & Burkert 2000; Quilis & Moore 2001). For neutral clouds moving with orbital velocity v through a hot ionized medium, stripping will occur when

$$\left(\frac{n_{\text{HIM}}}{10^{-4} \text{ cm}^{-3}}\right) \gtrsim 4.4 \left(\frac{\Sigma_{\text{DM}}}{10^7 M_{\odot} \text{ kpc}^{-2}}\right) \left(\frac{N_{\text{HI}}}{10^{20} \text{ cm}^{-2}}\right) \left(\frac{v}{100 \text{ km s}^{-1}}\right)^{-2} \quad (42)$$

where n_{HIM} is the HIM gas density, Σ_{DM} is the dark-matter surface density, and N_{HI} is the HI column density. For our model CHVC the DM surface density within the projected $1/e$ scale height is $\Sigma_{\text{DM}} = 1.0 \times 10^7 M_{\odot} \text{ kpc}^{-2}$. Setting N_{HI} equal to the peak column density of $5.1 \times 10^{19} \text{ cm}^{-2}$, and assuming a typical CHVC velocity of 100 km s^{-1} , it follows that stripping will occur for $n_{\text{HIM}} \gtrsim 2 \times 10^{-4} \text{ cm}^{-3}$. This is much larger than a HIM density of $2.5 \times 10^{-5} \text{ cm}^{-3}$ for a pressure $P_{\text{HIM}}/k = 50 \text{ cm}^{-3} \text{ K}$, and $T_{\text{HIM}} = 2 \times 10^6 \text{ K}$. We conclude that our pressure-confined $v_s = 12 \text{ km s}^{-1}$ mini-halo model clouds (and the cores of the observed clouds) would be stable against rapid stripping by our postulated coronal HIM at 150 kpc. We note, however, that at HIM densities of $2.5 \times 10^{-5} \text{ cm}^{-3}$, the observed (but not predicted) low-column density ($\lesssim 5 \times 10^{18} \text{ cm}^{-2}$) wings, should be stripped off the clouds. Their presence thus poses a challenge to our view of the CHVCs as pressure-confined objects. The cloud wings could conceivably represent stripped gas, but then the question remains as

to why this low column density gas is not photoionized by the background field (and by the additional sources of ionization indicated by the Weiner et al. observations).

We mention one additional problem. If the bounding pressure is reduced sufficiently, not only do the clouds become ionized, they also become unbound. For example, it is clear from Figure 6c that for $P_{\text{HIM}}/k = 1 \text{ cm}^{-3} \text{ K}$, our CHVC model lies in the unbound portion of the M_{WM} vs M_{vir} diagram, indicating that mass-loss from the outer layers of the cloud would occur for such a low HIM pressure. Thus, the question arises as to how the gas was retained by the mini-halos prior to their approach into the circumgalactic environment. This problem can be alleviated if the gravitational potential well is deepened by increasing the mini-halo mass. E.g., increasing v_s to 17 km s^{-1} is sufficient to keep our WM mass of $1.1 \times 10^6 M_{\odot}$ bound (although still ionized) for $P_{\text{HIM}}/k = 1 \text{ cm}^{-3} \text{ K}$ (see Fig. 6c). However, the expected number of objects decreases rapidly as v_s is increased as indicated by equation (38).

6.2. CHVCs as Extragalactic Minihalos

We now consider the possibility that the CHVCs are more distant “extragalactic” objects, and represent sub-structure on the scale of the entire Local Group (LG). This is the basic picture proposed by Blitz et al., who placed the CHVCs at characteristic distances of $\gtrsim 750 \text{ kpc}$. As we will show, models for the CHVCs can be constructed for such distances. However, there are two major difficulties with this picture. First, the mini-halos must be extremely underconcentrated. Second, the reduced central gas pressures suppress the formation of multi-phased cores.

For $d = 750 \text{ kpc}$, the observed CHVC HI gas scale height of 690 arcsec corresponds to a linear scale of 2.5 kpc . Such large values for the gas scale height require extremely underconcentrated halos, for both Burkert and NFW potentials (see Table 6 and Figs. 16 and 17). Such objects must deviate very substantially from the correlation $x_{\text{vir}}(M_{\text{vir}})$ expected for median ΛCDM halos, with $\sigma \lesssim -4$ for Burkert halos, and $\sigma \lesssim -6$ for NFW halos. This is a major problem with the LG hypothesis. At distances $\gtrsim 750 \text{ kpc}$, the CHVC halos would have to be quite different from those found in the CDM collapse simulations (see §2.2). From a more observational perspective, the CHVCs would then represent objects that are quite distinct from the dwarf galaxies. For example, for $r_{\text{gas}} = 2.5 \text{ kpc}$ the required DM scale density in Burkert halos (see Table 6) must be extremely small, with $n_{ds} \approx 5 \times 10^{-2} \text{ cm}^{-3}$. This is much smaller than the characteristic DM densities of $\sim 1 \text{ cm}^{-3}$ that we find for Leo A and Sag DIG, or that have been inferred from the dwarf galaxy rotation curve studies.

As a specific example of a CHVC model for $d \approx 750 \text{ kpc}$, we again consider a pressure-

confined system. We select a -4σ Burkert halo with $v_s = 12 \text{ km s}^{-1}$. The corresponding virial mass is $3 \times 10^8 M_\odot$. We set the confining pressure equal to the minimum possible HIM pressure for bound cloud solutions. For this model the minimum pressure is $P_{\text{HIM}}/k = 20 \text{ cm}^{-3} \text{ K}$. We choose a WM gas mass equal to $M_{\text{WM}} = 5.8 \times 10^7 M_\odot$, to give a total HI column within the observed range. The resulting model structure is displayed in Figure 15, and the model parameters are summarized in Table 4. We note that for this model the concentration parameter $x_{\text{vir}} = 8.1$. This is extremely small for our assumed halo mass. For median halos, such concentrations are expected for masses $\sim 10^{13} M_\odot$ (see eq. [14]), corresponding to the mass scale of an entire galaxy group.

In our extragalactic model, the peak HI column density equals $1.0 \times 10^{20} \text{ cm}^{-2}$. The intrinsic WM gas scale height is $r_{\text{gas}} = 3.0 \text{ kpc}$, and the projected $1/e$ HI gas scale height $r_{\text{NHI}} = 2.6 \text{ kpc}$. For a WNM core size of 690 arcsec, the implied distance is 777 kpc. The pressure contrast $P_0/P_{\text{HIM}} = 4.4$, so that $P_0/k = 88 \text{ cm}^{-3} \text{ K}$. The central pressure satisfies the condition for multi-phased behavior $P_{\text{min}}(0) < P_0 < P_{\text{max}}(0)$ where $P_{\text{min}}(0) = 67$ and $P_{\text{max}}(0) = 523 \text{ cm}^{-3} \text{ K}$. We note that due to the larger distance, the central gas pressure is significantly lower than in our circumgalactic model. Large peak HI column densities are therefore required to provide the opacity necessary to reduce P_{min} and P_{max} to values that allow multi-phased gas in the core. For -4σ Burkert halos we find that multi-phased gas is possible for columns between 9×10^{19} to $3 \times 10^{20} \text{ cm}^{-2}$. In our specific extragalactic model a small multiphase core is just possible out to 1.2 kpc, consistent with the observed presence of CNM cores within the WNM gas scale height. While the required WNM column of $\sim 10^{20} \text{ cm}^{-2}$ is within the range of observed values, most of the CHVCs are not as shielded as this (Burton et al. 2001). At large distances, the multi-phased cores in most objects would vanish.

The WNM component extends to $r_{\text{WNM}} = 3.4 \text{ kpc}$, and is surrounded by a WIM envelope that extends to 7.2 kpc. The total HI mass is $1.4 \times 10^7 M_\odot$. The central gas density $n_{\text{H},0} = 7.6 \times 10^{-3} \text{ cm}^{-3}$ is sufficiently large for the formation of a neutral core (since for $r_{\text{gas}} \approx 2.5 \text{ kpc}$ $n_{\text{H},0\text{crit}} = 2 \times 10^{-3} \text{ cm}^{-3}$). As expected, the ionization front is associated with a projected HI column close to 10^{19} cm^{-2} . At 3.0 kpc from the cloud center, $N_{\text{HI}} = 8 \times 10^{18} \text{ cm}^{-2}$ and decreases below 10^{18} cm^{-2} at 4.0 kpc. Extended low column density wings at a level of $\sim 10^{18} \text{ cm}^{-2}$ are not present.

If the CHVCs are at large distances, and they are pressure-confined objects, their large extents set limits on the intergalactic medium (IGM) pressure within the Local Group. The bounding pressure P_{HIM} cannot exceed $\sim 40 \text{ cm}^{-3} \text{ K}$, since otherwise the clouds would be compressed to radii less than 2.6 kpc. Conversely, for $v_s = 12 \text{ km s}^{-1}$ the bounding pressure cannot be smaller than $20 \text{ cm}^{-3} \text{ K}$, since otherwise the clouds would become unbound. The

lower limit on the pressure can be reduced if more massive halos are considered. If the IGM pressure is close to the required $\sim 20 \text{ cm}^{-3} \text{ K}$ this gas must also be very hot. For a uniform density HIM contained within a sphere of radius d the total HIM mass is

$$M_{\text{HIM}} = 5.0 \times 10^{11} \left(\frac{d}{1 \text{ Mpc}} \right) \left(\frac{P_{\text{HIM}}/k}{10 \text{ cm}^{-3} \text{ K}} \right) \left(\frac{T_{\text{HIM}}}{10^6 \text{ K}} \right)^{-1} M_{\odot} \quad (43)$$

where T_{HIM} is the HIM temperature. Assuming the HIM mass does not exceed a fraction ~ 0.25 of the total baryonic mass $\sim 3 \times 10^{11} M_{\odot}$ of the LG (essentially the Milky Way plus M31) then for $d = 750 \text{ kpc}$, and $P_{\text{HIM}}/k = 20 \text{ cm}^{-3} \text{ K}$, it follows that $T_{\text{HIM}} \gtrsim 10^7 \text{ K}$. It is difficult to see how such hot gas could remain bound to the Local Group.

Finally, another important feature of models for $d \gtrsim 750 \text{ kpc}$ is a much larger WM to DM mass ratio. In our extragalactic model, $M_{\text{WM}}/M_{\text{vir}} = 0.22$ (more than twice the cosmic baryon fraction) as opposed to 0.011 in our circumgalactic model. For $v_s = 12 \text{ km s}^{-1}$, M_{vir} grows by a factor of 3.2 as σ is reduced from 0 to -4. In contrast, $M_{\text{WM}} \simeq \pi m_{\text{H}} N_{\text{H}} r_{\text{gas}}^2$, so that M_{WM} grows by a factor $\gtrsim 50$. The gas-to-DM mass fraction can be reduced if v_s is increased. However, it is clear that as the CHVC halos are placed at larger distances they must become increasingly gas rich. This poses an additional problem for the extragalactic hypothesis, as it is difficult for low-mass halos to retain their gas.

7. Summary

In this paper we examine the hypothesis that the compact high velocity HI clouds (CHVCs) trace sub-structure within the dark-matter halo of the Galaxy, or within the entire Local Group system.

For this purpose we carry out detailed computations of the coupled hydrostatic and ionization structures of pressure supported clouds that are confined by gravitationally dominant dark-matter (DM) “mini-halos”. We focus on low-metallicity systems that are ionized and heated by the metagalactic background field. We provide a fit for this field (from the near-IR to the hard X-ray regime) that is based on a combination of observations and theoretical estimates. We explicitly consider the effects of external bounding pressures on the mini-halo cloud structure. We consider bounding pressures provided by a hot ionized Galactic corona or an intergalactic medium in the Local Group.

We consider dark-matter halos with either cuspy (NFW) or constant density (Burkert) cores. We adopt a Λ CDM cosmological model to parameterize the expected correlations between the various halo scale parameters, as well as the dispersion in the correlations. We focus on low-mass halos with virial masses $\sim 10^8$ to $10^{10} M_{\odot}$, (or halo scale velocities between

~ 10 to 50 km s^{-1}) containing warm (10^4 K) clouds of neutral plus photoionized gas with masses between $\sim 10^4$ and $10^8 M_\odot$.

We determine how the cloud sizes and hydrogen gas distributions, as well as the gas phase-states – ionized (WIM), neutral (WNM), or multi-phased (WNM/CNM) – depend on the halo parameters, gas masses, and bounding pressures. We consider both gravitationally confined systems, where the gas is effectively restricted to within the halo scale radii (or halo cores), as well as pressure-confined clouds in which the gas can extend to large halo radii. We find that gravitationally confined systems are those for which $v_s/c_g \gtrsim 1.5$, where v_s is the halo scale velocity and c_g is the gas sound speed. We determine the conditions required for the transition from ionized to neutral clouds, and for the formation of thermally unstable multi-phased (WNM/CNM) cores within neutral clouds. We also compute the emission measures and $\text{H}\alpha$ recombination line surface brightnesses that are produced in the WIM components of the halo clouds. For optically thick clouds ionized by the metagalactic field, we find that the $\text{H}\alpha$ surface brightness ranges from 4 mR at the cloud centers to 7 mR at the limb-brightened edges.

As a step in our computations we construct pressure vs. density phase diagrams for low metallicity ($Z = 0.1Z_\odot$) gas that is heated by the metagalactic field for a wide range ($10^{18} - 10^{21} \text{ cm}^{-2}$) of assumed HI shielding columns, and we compute the critical phase-transition pressures P_{\min} and P_{\max} as functions of the hydrogen ionization rate. We use the results of these computations to determine the thermal phase states of the neutral gas in our halo cloud models.

We present mini-halo models for the pressure supported HI structures observed in the Local Group dwarf irregular galaxies Leo A and Sag DIG. We include the stellar contribution to the gravitational potentials. We identify the HI cloud boundaries observed in Leo A and Sag DIG with the ionization fronts, and we derive an upper limit of $P_{\text{HIM}}/k \lesssim 100 \text{ cm}^{-3} \text{ K}$ for the ambient pressure of the intergalactic medium in the Local Group. The distances to Leo A and Sag DIG are well established, and the observed HI gas scale heights of 0.5 kpc in these objects imply characteristic DM densities of 1.2 amu cm^{-3} (or $0.03M_\odot \text{ pc}^{-3}$) for the DM halos. These densities are consistent with those previously found via rotation curve studies of rotationally supported dwarfs and low-surface brightness galaxies. Leo A and Sag DIG obey the halo correlations that are expected for typical (“median”) DM halos in a Λ CDM cosmology, provided the halos contain constant density cores. NFW halos would have to be extremely underconcentrated (by -4σ relative to median halos) given the observed gas scale heights.

For the family of median Burkert (or -4σ NFW) halos that obey the scalings and correlations as fixed by the dwarf galaxies, we find that the transition from ionized to neutral

clouds occurs for central WNM HI column densities equal to $3 \times 10^{18} \text{ cm}^{-2}$, independent of the halo virial mass or total gas mass. The gas is fully neutral within projected radii where HI column exceeds 10^{19} cm^{-2} . A photoionization cut-off is predicted near 10^{19} cm^{-2} (similar to what is found for flattened, rotationally supported, disk systems) independent of the halo mass. We find that for clouds heated by the metagalactic field, multi-phased cores occur for peak WNM columns between 2×10^{19} and $2 \times 10^{20} \text{ cm}^{-2}$. The peak WNM columns of $\sim 10^{21} \text{ cm}^{-2}$ observed in the dwarf galaxies require additional (possibly internal) heat sources.

We construct explicit “mini-halo” models for the multi-phased (and low-metallicity) compact high-velocity HI clouds. We consider the CHVCs as either “circumgalactic” objects associated with the Milky Way halo, with implied characteristic distances of 150 kpc, or as more distant $\gtrsim 750$ kpc “extragalactic” Local Group objects. If the CHVC halos are drawn from the same family of halos that successfully reproduce the dwarf galaxy observations, then the CHVCs must be circumgalactic objects. The observed $1/e$ gas scale heights then correspond to sizes of 0.5 kpc (as in the dwarfs). The typical HI mass for an individual CHVC is then $\sim 3 \times 10^5 M_\odot$, and the total HI mass in the entire population of CHVCs is $\sim 6 \times 10^7 M_\odot$. The predicted multi-phased behavior that occurs for peak WNM columns between 2×10^{19} and $2 \times 10^{20} \text{ cm}^{-2}$ is consistent with the observed multi-phased behavior and range of peak WNM columns in the CHVCs. If the large population of CHVCs represent “missing low-mass DM satellites” of the Galaxy, then these HI clouds must be pressure-confined to keep the gas neutral within the weak DM potentials. The observed number of CHVCs imply typical CHVC mini-halo scale velocities of $v_s = 12 \text{ km s}^{-1}$. For such objects the confining pressure must exceed $\sim 50 \text{ cm}^{-3} \text{ K}$ to keep the gas bound. We construct a simple model for a Galactic corona, and show that a hot $2 \times 10^6 \text{ K}$ Galactic corona (in pressure equilibrium with the Galactic disk) could provide the required pressure at 150 kpc.

If the CHVCs are “extragalactic” objects with distances $\gtrsim 750$ kpc, then their associated halos must be very “underconcentrated”, with characteristic DM densities $\lesssim 0.08 \text{ cm}^{-3}$, much smaller than expected for their mass, and significantly smaller than observed in the dwarf galaxies. Multi-Phased cores are possible, but require shielding columns that are generally higher than observed. For $d = 750$ kpc, the typical CHVC HI mass is $\sim 1 \times 10^7 M_\odot$, and the total HI mass in the system of CHVCs is $\sim 2 \times 10^9 M_\odot$.

Our analysis favors the circumgalactic hypothesis for the location of the CHVCs. In this picture, the CHVCs represent pressure-confined clouds that are associated with tidally truncated dark-matter sub-halos that have survived the hierarchical formation process of the Galactic halo. The CHVC mini-halos are visible as neutral 21 cm sources due the compression provided by an ambient Galactic corona.

Our analysis also appears to favor Burkert halos with constant density dark-matter

cores, as opposed to NFW halos with diverging central DM densities. While Burkert halos are consistent with the observed scale heights at circumgalactic distances of 150 kpc, NFW halos would have to be significantly underconcentrated to yield the observed cloud sizes for such distances.

We compute the maximum masses of WNM gas that can be maintained by the metagalactic field within the DM halos. Our analysis suggests that in the mini-halo scenario for the CHVCs, these objects are “failed galaxies” and did not form stars, because most of the neutral gas was always maintained as WNM by the metagalactic field. In contrast the halos associated the dwarf galaxies in the Local Group (and elsewhere) contained sufficiently large masses of gas such that most of the neutral component was converted to CNM, a precondition for star-formation.

Our hydrostatic mini-halo cloud models are able to account for many properties of the CHVCs, including their observed peak HI columns, core sizes, and multi-phased behavior. However, important theoretical and observational difficulties remain. Theoretically, a question remains as to the origin of the gas in the CHVC mini-halos. The gas is unlikely to be purely primordial, since such gas is easily lost from low-mass mini-halos as the bounding pressure becomes low. The presence in some objects of extended low column density HI wings, and H α emission line fluxes in several CHVCs that are significantly larger than expected, represent significant observational challenges to the mini-halo models we have presented in this paper. Additional high resolution HI mapping observations and sensitive H α line measurements are required to determine the possible contributions of gas stripping and perhaps collisional ionization to the CHVC cloud structure. Such observations will help establish, or possibly refute, the hypothesis that the CHVCs trace dark-matter substructure.

We thank Leo Blitz, Stu Bowyer, James Bullock, Butler Burton, Marc Davis, Orly Gnat, David Hollenbach, Tsafir Kollat, and David Spergel for many helpful discussions during the course of this work. We thank James Bullock for providing us with his CDM halo code. We also thank the referee for comments and suggestions that improved this paper. C.F.M. was supported in part by NSF grant AST-0098365. M.G.W. was supported in part by a NASA LTSA grant NAG5-9271, and by NSF grant AST 95-29167.

A. NFW AND BURKERT HALOS AND THE SMALL- x LIMIT

In this appendix we derive some useful analytic formulae for the cloud properties and gas distributions when the clouds are confined to the “small- x ” ($x < 1$) regions of the

dark-matter halos.

We first summarize the basic properties of the NFW (Navarro et al. 1997) and Burkert (1995) dark-matter halos. In Table 5 we list the expressions for the (dimensionless) density profile, f_ρ , the enclosed mass, f_M , and the gravitational potential, f_φ , (as defined in §2.1) for NFW and Burkert halos.

In NFW halos the central densities diverge, with $f_\rho \approx 1/x$ for $x \ll 1$, while the enclosed mass and potential remain finite, with $f_M \approx (3/2)x^2$ and $f_\varphi \approx (3/2)x$. The scale density ρ_{ds} (see §2.1) equals the local DM density at $x = 0.46$. At $x = 1$ the DM density $\rho_d = \rho_{ds}/4$, and the enclosed mass $M_d = 0.58M_{ds}$. The enclosed mass $M_d = M_{ds}$ at $x = 1.6$. For $x \gg 1$, $f_\rho \approx 1/x^3$, f_M diverges logarithmically, and f_φ approaches an asymptotic value of 3. The circular velocity $v = v_s f_v$ reaches a maximum value $v_{\max} = 0.8v_s$ at $x = 2.2$.

Burkert halos are defined such that they contain constant density dark-matter cores. Thus, for $x \ll 1$, $f_\rho \approx 1$, $f_M \approx x^3$, and $f_\varphi \approx x^2/2$. The scale density ρ_{ds} equals the central (core) density $\rho_d(0)$. At $x = 1$ the DM density $\rho_d = \rho_{ds}/4$, and the enclosed mass $M_d = 0.38M_{ds}$. The enclosed mass $M_d = M_{ds}$ at $x = 1.7$. For $x \gg 1$, $f_\rho \approx 1/x^3$, f_M diverges logarithmically, and f_φ approaches an asymptotic value of $3\pi/4$. The circular velocity $v = v_s f_v$ reaches a maximum value $v_{\max} = 0.8v_s$ at $x = 3.3$.

We now consider simplified isothermal clouds with fixed ionization state (e.g., fully ionized or completely neutral) so that the gas is characterized by a constant velocity dispersion c_g . Writing equation (20) as

$$\frac{d\rho}{\rho} = -\frac{1}{c_g^2} d\varphi \tag{A1}$$

it follows that the hydrostatic gas density profile for a dark-matter dominated cloud is

$$f_{\text{gas}}(x) \equiv \frac{n_{\text{H}}}{n_{\text{H},0}} = \exp\left(-\frac{v_s^2}{c_g^2} f_\varphi\right) \tag{A2}$$

where f_φ is the dimensionless halo potential. For a given halo profile (NFW or Burkert) the gas density distribution depends on the single parameter v_s/c_g . In Table A1 we include the resulting analytic solutions for the gas distributions (Makino, Sasaki & Suto 1998; Wu 2000, Wu & Xue 2000) as given by equation (A2).

For $x \ll 1$ the expressions for the gas distributions simplify considerably, and simple analytic formulae for the gas scale heights, column densities, masses, and cloud emission measures may be derived. We list these various formulae in Table 6.

In the small- x limit, the gas density distribution f_{gas} varies exponentially in NFW halos. In Burkert halos the gas distribution is a Gaussian. For both halo types, we define the gas

scale height, $x_{\text{gas}} = r_{\text{gas}}/r_s$, as the radius at which the gas density decreases to a factor $1/e$ times the central value. Expressions for r_{gas} as functions of the DM halo parameters are listed in Table 6. In NFW halos r_{gas} depends on two (correlated) halo scale parameters, e.g. n_{ds} and r_s , or r_s and v_s . In Burkert halos, r_{gas} may be expressed as a function of n_{ds} only, that is, on the value of the uniform dark-matter density in the $x \ll 1$ halo core.

In Figures 16 and 17 we plot the small- x values of r_{gas} as a function of the halo scale velocity, v_s , for median, $+3\sigma$ over-concentrated, and -3σ under-concentrated NFW and Burkert halos. In Figures 16 and 17 we display r_{gas} as a function of M_{vir} . In these plots we assume a (WNM) sound speed of 8.2 km s^{-1} . Analytic expressions for r_{gas} as functions of σ and v_s , or as functions of σ and M_{vir} may be obtained using the scaling relations (18), (19), and (17) for n_{ds} , r_s and M_{vir} (see §2.2). We list these expressions for r_{gas} in Table 6. In both NFW and Burkert halos the scale heights for median ($\sigma = 0$) halos are small. For median NFW halos r_{gas} ranges from 0.1 to 0.04 kpc for v_s between 10 to 50 km s^{-1} , or virial masses between 10^8 and $10^{10} M_{\odot}$. For median Burkert halos r_{gas} ranges from 0.2 to 0.6 kpc for v_s from 10 to 50 km s^{-1} , or M_{vir} between 10^8 and $10^{10} M_{\odot}$. We note that for Burkert halos r_{gas} is a very weak function of M_{vir} . The scale heights may be increased by moving to under-concentrated halos. We illustrate this in Figures 16c, 16d, 17c, and 17d where we display level curves for r_{gas} in the range of 0.5 to 2.5 kpc, in σ vs. v_s , and σ vs. M_{vir} diagrams. It is apparent that large scale heights require extremely underconcentrated halos.

In the small- x limit the total gas mass remains finite as $x_{\text{W/H}}$ becomes arbitrarily large (i.e. as the bounding pressure is reduced to zero). Similarly, the gas column densities at all impact parameters $b \equiv r_p/r_{\text{gas}}$ (where r_p is the projected radius) remain finite. Small- x expressions for the cloud masses and columns are listed in Table 6. In NFW halos the column densities are proportional to $bK_1(b)$ where K_1 is the first-order modified Bessel function. The product $bK_1(0) = 1$ for $b = 0$, and declines by a factor of $1/e$ at $b = 1.65$. Thus, for NFW halos the projected $1/e$ scale height is 1.65 times larger than the intrinsic gas scale height. In Burkert halos the column density distribution is a Gaussian, and the projected $1/e$ scale height is equal to the intrinsic scale height.

Analytic conditions for the transition from ionized to neutral clouds may be derived based on the behavior of the cloud emission measure with varying optical depth. The emission measure depends on the fraction of the incident flux, πJ^* , of Lyman continuum photons that are absorbed by the cloud. In optically thick clouds, the entire Ly α flux is absorbed in a thin shell, and $EM(x = 0) = 2\pi J^*/\alpha_B$. In the opposite limit, EM must vanish in optically thin clouds as the cloud mass becomes sufficiently small. Our radiative transfer computations show that EM always reaches a maximum value of

$$EM_{\text{max}}(x = 0) \approx 4\pi J^*/\alpha_B \quad , \quad (\text{A3})$$

in *critical clouds* where the fractional ionization $x_e = 0.5$ at the cloud center. Indeed, it is straightforward to show analytically that for spherical clouds (and with the neglect of secondary ionizations) the emission measure must satisfy the upper and lower bounds, $8\pi J^*/\alpha_B \geq EM \geq 2\pi J^*f/\alpha_B$, where f is the fraction of the incident radiation that is absorbed. Our radiative transfer computations are consistent with these limits. We find that EM vanishes when the cloud is optically thin and f is small. The emission measure then rises to a maximum value of close to $4\pi J^*/\alpha_B$ in critical clouds, and then declines to $EM = 2\pi J^*/\alpha_B$ in optically thick ($f = 1$) clouds.

The emission measures for fully ionized clouds are listed in Table 6. Crucially, these emission measures cannot exceed EM_{\max} . It follows that to remain fully ionized the gas scale height must satisfy an upper bound, with

$$r_{\text{gas}} \leq \frac{4\pi J^* f}{\alpha_B n_{\text{H},0}^2} = 1.24 J_3^* f \left(\frac{n_{\text{H},0}}{10^{-3} \text{ cm}^{-3}} \right)^{-2} \quad (\text{A4})$$

where $f = 1$ for NFW halos, $f = \sqrt{2/\pi}$ for Burkert halos, and $J_3^* \equiv J^*/10^3$ photons $\text{cm}^{-2} \text{ s}^{-1} \text{ sr}^{-1}$ (for our assumed field $J_3^* = 1.02$). Neutral cores must form when r_{gas} exceeds this limit. We identify critical clouds as those for which equality holds in equation (A4). Given our formulae for r_{gas} equation (A4) implies a critical central gas density, $n_{\text{H},0\text{crit}}$ above which neutral cores must form. The resulting expressions for $n_{\text{H},0\text{crit}}$, as functions of v_s or M_{vir} , are listed in Table 6. We note that in evaluating these critical densities, a WIM sound speed should be adopted since critical clouds are WIM dominated. It is evident that for NFW halos the critical density is a weakly increasing function of the halo scale velocity or mass, whereas in Burkert halos the critical density is a very weakly decreasing function of the scale velocity or mass.

For what values of v_s/c_g is the small- x approximation valid? It follows from the analytic expressions for f_{gas} listed in Table 5 that for $v_s/c_g \gtrsim 2$ the gas densities become vanishingly small for $x \gtrsim 1$, while for $v_s/c_g \lesssim 2$ the gas densities remain relatively large out to large halo radii. Given the analytic expressions for f_{gas} listed in Table 5 we have numerically integrated the total gas mass, $M_{\text{WM}}/4\pi r_s^3 n_{\text{H},0}$, peak gas column, $N_{\text{WMpeak}}/2n_{\text{H},0} r_s$, and emission measure $EM/2n_{\text{H},0}^2 r_s$ (assuming fully ionized clouds) as functions of v_s/c_g . We then compared the results of the numerical integrations to the values as given by the small- x formulae. We find that for $v_s/c_g > 1.5$ the small- x expressions for the gas column (and therefore also the gas scale height r_{gas}), and the emission measure, are good to better than a factor of 2, for both NFW and Burkert profiles. For $v_s/c_g > 2$ the accuracy is better than a few percent. The total gas mass diverges rapidly at small v_s/c_g , and the small- x expressions for the total gas mass become accurate only for $v_s/c_g > 3$. For such large values of v_s/c_g the gas mass is effectively independent of the bounding pressure as P_{HIM} becomes arbitrarily small.

B. METAGALACTIC RADIATION FIELD

In this paper we construct models assuming the ($z = 0$) metagalactic field is the dominant source of radiation impinging on the mini-halo clouds.

The external field, J_ν (ergs cm⁻² s⁻¹ Hz⁻¹ sr⁻¹, hereafter cgs units), is a critical quantity controlling the overall cloud structure. For a given total gas mass, the Lyc flux determines the fractions contained in the WIM vs. the shielded WNM components. The radiation field also determines the thermal phase state of the HI gas (see §3.2), since hard ultraviolet (EUV) and X-ray photons can penetrate into the shielded cores and heat the HI gas via photoionization. Non-ionizing radiation is also important. Far-ultraviolet (FUV) grain photoelectric emission is a heat source, while FUV photons produce the C⁺ ions which dominate the cooling of the CNM. Molecular hydrogen (H₂) is photodissociated by the FUV field, and the abundance of H⁻, a key intermediary in the gas phase production of H₂, is limited by optical and infrared photodetachment.

In view of the above processes the metagalactic field must be specified from X-ray energies ~ 1 keV, above which clouds with the largest HI columns we consider ($\sim 10^{22}$ cm⁻²) become optically thin, down to to the near-infrared H⁻ photodetachment threshold at 1.64 μ m. We adopt a representation for the metagalactic field that is based on a combination of observational constraints and theoretical estimates. We then estimate the distance from the Galactic disk at which the metagalactic field dominates. We first consider the ionizing radiation, and then the FUV through IR components.

The metagalactic Lyc flux is generally believed to be produced by quasars with an additional possible contribution from star-forming galaxies. The background field is directly observable at X-ray wavelengths (Gendreau et al. 1995; Chen, Fabian & Gendreau 1997; Miyaji et al. 1998; Hasinger 2000), but is unobservable near the Lyman limit due to efficient absorption by Galactic HI.

The unobservable flux at $z = 0$ can be constrained via H α recombination line measurements from (starless) intergalactic HI clouds (Vogel et al. 1995; Weiner et al. 2001), or via measurements of the HI “truncation column densities” at the edges of galaxy disks (Sunyaev 1969; Silk 1971; Maloney 1993). Vogel et al. (1995) determined a (2σ) upper limit of 20 mR for the H α surface brightness in the intergalactic Giovanelli & Haynes cloud. This measurement sets an upper limit on $4\pi J^*$ (eq.[25]). For opaque spherical clouds, $4\pi J^* = \alpha_B \langle EM \rangle$ where $\langle EM \rangle$ is the emission measure averaged over the projected surface area. We conclude that $4\pi J^* < 4.5 \times 10^4$ photons cm⁻² s⁻¹ in the local IGM.

Theoretical calculations of the metagalactic ionizing radiation field at low redshifts have been presented by Haardt & Madau (1996), Okoshi & Ikeuchi (1996), and Shull et al. (1999)

with similar results. At $z = 0$ Haardt & Madau estimate that $J_{\nu_0} = 2.0 \times 10^{-23}$ cgs at the Lyman limit, while Shull et al. find $J_{\nu_0} = 1.3 \times 10^{-23}$ cgs. The Lyc intensity drops sharply (as an approximate power-law) to a value of $\sim 3 \times 10^{-25}$ cgs at the HeII edge (4 ryd), and flattens at higher energies where the IGM becomes less opaque.

In estimating the background field below 4 ryd to the Lyman limit we rely on on the Haardt & Madau calculations. At energies greater than 4 ryd including EUV and X-ray wavelengths we rely on observations. Chen et al. (1997) (see also Gendreau et al. 1995) find that between 1 and 7 keV the X-ray background (as observed by ROSAT and ASCA) is well fit by a simple power-law, $AE_{\text{keV}}^{-\Gamma}$, where E_{keV} is the photon energy in keV, $A = 10.5 \pm 0.3$ photons $\text{s}^{-1} \text{cm}^{-2} \text{keV}^{-1} \text{sr}^{-1}$, and the photon index $\Gamma = 1.46 \pm 0.06$. A very similar result was found by Miyaji et al. (1998). At soft X-ray energies ($\lesssim 1\text{keV}$) it becomes difficult to disentangle the background from thermal emission produced in the (distant) Galactic halo and (nearby) Local Bubble of hot gas. However, in an analysis of soft X-ray “shadows” (i.e. anticorrelations on the sky between soft X-ray flux and absorbing HI column density) Snowden et al. (2000) argue that the Chen et al. power-law plausibly extends down to 1/4 keV, where additional flux (of distant origin) at 1/4 keV is due to a thermal $10^{6.4}$ K Galactic component.

We note that the Chen et al. power-law gives $J_{\nu} = 2.7 \times 10^{-25}$ cgs at the HeII edge (0.054 keV). This is only slightly smaller than the theoretical Haardt & Madau value of 3.2×10^{-25} cgs at 4 ryd. We therefore assume that the Chen et al. power-law extends down to 4 ryd. For lower energies we adopt a second power-law that matches Chen et al. at 4 ryd, and Haardt & Madau at the Lyman limit. This gives,

$$J_{\nu} = J_{\nu_0} \left(\frac{\nu}{\nu_0} \right)^{-3.13} \quad (\text{B1})$$

for $1 < \nu/\nu_0 < 4$, and

$$J_{\nu} = 2.512 \times 10^{-2} J_{\nu_0} \left(\frac{\nu}{\nu_0} \right)^{-0.46} \quad (\text{B2})$$

for $\nu/\nu_0 > 4$, where $J_{\nu_0} = 2.0 \times 10^{-23}$ cgs and ν_0 is the Lyman limit frequency. Most of the ionizing energy is emitted near the Lyman limit, although it is evident that the total energy in the Chen et al. field (with $\nu J_{\nu} \sim \nu^{0.54}$) increases with photon energy (see Fig. 5). The Chen et al. field is truncated at a turn-over energy near 100 keV (see Hasinger 2000).

Assuming the Vogel et al. (1995) $\text{H}\alpha$ limit, and assuming that the ionizing field varies with frequency as given by equations (B1) and (B2), we derive an upper limit of $J_{\nu_0} < 7.0 \times 10^{-23}$ cgs for the metagalactic field intensity at the Lyman limit. The upper limit (shown in Fig. 8) is 3.5 times larger than the value computed by Haardt and Madau.

We now consider the FUV and optical extragalactic background. This background is generally believed to be produced by the integrated light of faint and distant galaxies. Martin and Bowyer (1989) and Martin, Hurwitz, & Bowyer (1991) carried out sounding rocket and space-shuttle observations, and detected a 1600 Å background flux $F_{1600}^* = 40 \pm 10$ photons $\text{cm}^{-2} \text{s}^{-1} \text{Å}^{-1} \text{sr}^{-1}$, corresponding to $J_\nu = 4.2 \pm 1.1 \times 10^{-22}$ cgs at 1600 Å. Armand, Milliard & Deharveng (1994) found that at 2000 Å J_ν lies in the range of 5.3×10^{-22} to 1.7×10^{-21} cgs, consistent with the Martin & Bowyer observations.

Bernstein (1999) (see also Bernstein, Freedman & Madore 2002) has recently reported the first (HST) detections of the extragalactic background light at optical wavelengths. She finds that J_ν equals $1.2 \pm 0.57 \times 10^{-20}$, $2.8 \pm 0.8 \times 10^{-20}$, and $4.9 \pm 1.3 \times 10^{-20}$ cgs, at 3000, 5500, and 8000 Å respectively. The measured fluxes are consistent with the upper limit of 1.2×10^{-19} cgs at 4000 Å previously set by Matilla (1989).

We fit the FUV and optical measurements with a two-piece power-law expression

$$J_\nu = J_{\nu_0} \left(\frac{\nu}{\nu_0} \right)^{-5.41} \quad (\text{B3})$$

for $1 > \nu/\nu_0 > 0.3$ (i.e. from 912 to 3000 Å), and

$$J_\nu = 1.051 \times 10^2 J_{\nu_0} \left(\frac{\nu}{\nu_0} \right)^{-1.5} \quad (\text{B4})$$

for $\nu/\nu_0 < 0.3$, where again $J_{\nu_0} = 2 \times 10^{-23}$ cgs. This fit is consistent with the FUV and optical observations within the errors, (see Fig. 5). At 1.25 μm equation (B4) gives 1.1×10^{-19} cgs, consistent with the (COBE) upper limit of 2.8×10^{-19} cgs found by Dwek & Arendt (1998) at 1.25 μm . We assume that equation (B4) remains valid down to the H^- threshold at 1.65 μm .

For our fit to the metagalactic field the mean intensity in the 6-13.6 eV FUV range is 6.7×10^{-6} ergs $\text{cm}^{-2} \text{s}^{-1}$. This is 0.42% of the mean FUV intensity in the solar neighborhood as estimated by Habing (1968).

At what distance from the Galaxy does the metagalactic background dominate the radiation field? The Galaxy produces Lyc photons (mainly in OB associations) at a rate of $Q_{\text{Gal}} \sim 2.6 \times 10^{53}$ photons s^{-1} . A small but uncertain fraction, $f_{\text{esc}} \sim 5\%$, of this radiation may escape the optically thick disk (Dove & Shull 1994; Bland-Hawthorn & Maloney 1999; Dove, Shull & Ferrara 2000). For $f_{\text{esc}} = 5\%$, the Galactic Lyc flux at the surface of an opaque spherical cloud (on the side facing the Galaxy), $Q_{\text{Gal}} f_{\text{esc}} / 4\pi d^2$, equals the metagalactic Lyc flux of $\pi J^* = 3.2 \times 10^3$ photons $\text{cm}^{-2} \text{s}^{-1}$ at a distance $d = 180$ kpc. The Galaxy may also be a source of soft X-rays emitted by cooling hot gas in supernova remnants (Slavin, McKee

& Hollenbach 2000). These authors estimate that for photon energies greater than 100 eV a soft X-ray luminosity of 2.2×10^{39} erg s⁻¹ escapes the Galaxy. This implies that the Galactic and metagalactic X-ray fluxes (between 0.1 and 1 keV) are equal at $d = 16$ kpc. It is most straightforward to estimate the non-ionizing (IR through UV) luminosity of the Galaxy via direct observations of an analogous galaxy. For example, Kennicutt (2001) has noted that the SBbc galaxy NGC 3992 is very similar to the Galaxy in size, shape, luminosity, and star-formation properties. The distance to NGC 3992 is 15 Mpc, and its IR ($1.65\mu\text{m}$), optical (5500 \AA), and FUV (1600 \AA) luminosities are equal to 2.2×10^{29} , 1.5×10^{29} and 2.0×10^{27} erg s⁻¹ Hz⁻¹ respectively (data from the NED database¹⁷). Assuming these values for the Milky Way, the non-ionizing Galactic and metagalactic fluxes are equal at ~ 100 kpc. Given the above estimates we conclude that the metagalactic field begins to dominate the ionization and heating of the clouds at a distance of 100 to 200 kpc from the Galaxy.

¹⁷nedwww.ipac.caltech.edu

References

- Aaronson, M. 1983, *ApJ*, 266, L11
- Armand, C., Milliard, B., & Deharveng, J.M. 1994, *AA*, 284, 12
- Bahcall, N., Ostriker, J.P., Perlmutter, S., & Steinhardt, P.J. 1999, *Science*, 284, 1481
- Bajaja, E., Morras, R., & Poppel, W.G.L. 1987, *Pub. Astr. Inst. Czech. Ac. Sci.*, 69, 237
- Bakes, E.L.O., & Tielens, A.G.G.M. 1994, *ApJ*, 427, 822
- Ballantyne, D.R., Ferland, G.J., & Martin, P.G. 2000, *ApJ*, 536, 773
- Balucinska-Church, M., & McCammon, D. 1992, *ApJ*, 400, 699
- Barkana, R., & Loeb, A. 1999, *ApJ*, 523, 54
- Bernstein, R.A. 1999, in *The Hy Redshift Universe*, ASP Conf. vol. 193, eds. A. J. Bunker and W. J. M. van Breugel (ASP: San Francisco), 48
- Bernstein, R.A., Freedman, W.L., & Madore, B.F. 2002, *ApJ* in press
- Blais-Ouellette, S., Amram, P., & Carignan, C. 2001, *AJ*, 121, 1952
- Bland-Hawthorn, J., Veilleux, S., Cecil, G.N., Putman, M.E., Gibson, B.K., & Maloney, P.R. 1998, *MNRAS*, 299, 611
- Bland-Hawthorn, J., & Maloney, P.R. 1999, *ApJ*, 510, L33
- Blitz, L., Spergel, D., Teuben, P., Hartmann, D., & Burton, W.B. 1999, *ApJ*, 514, 818
- Blitz, L., & Robishaw, T. 2000, *ApJ*, 541, 675
- Blumenthal, G.R., Faber, S.M., Primack, J.R., & Rees, M.J. 1984, *Nature*, 311, 517
- Bowen, D.V., & Blades, J.C. 1993, *ApJ*, 403, L55
- Braun, R., & Burton, W.B., 2000, 354, 853
- Bregman, J. 1996, in *The Interplay between Massive Star Formation, Galaxy Evolution, and the ISM*, D. Kunth et al. eds., 11th IAP Astrophysics meeting, Institut d’Astrophysique, Paris, Gif-Sur-Yvette, Editions Frontieres, 211.
- Brüns, C., Kerp, J., Kalberla, P.M.W., & Mebold, U. 2000, *AA*, 357, 120
- Brüns, C., Kerp, J., & Pagels, A. 2001, *AA* 370, L26
- Bruzual, G., & Charlot, S. 1993, *ApJ*, 466, 254

- Bullock, J.S., Kollat, T.S., Sigad, Y., Somerville, R.S., Kravtsov, A.V., Klypin, A.A., Primack, J.R., & Dekel, A. 2001, MNRAS, 321, 559
- Bullock, J.S., Kravtsov, A.V., & Weinberg, D.H. 2000, ApJ, 539
- Burkert, A. 1995, ApJ, 447, L25
- Burton, W.B., Braun, R., & Chengalur, J.N. 2001, AA 369, 316
- Cardelli, J.A., Meyer, D.M., Jura, M., Savage, B.D. 1996, ApJ, 467, 334
- Chen, L.-W., Fabian, A.C., & Gendreau, K.C. 1997, MNRAS, 285, 449
- Cook, K.H. 1988, BAAS, 20, 742
- Corbelli, E. & Salpeter, E.E. 1993, ApJ, 419, 104
- Dalal, N., & Kochanek, C. 2002, ApJ in press
- Danly, L., Albert, C.E., & Kuntz, K.D. 1993, ApJ, 416, L29
- de Blok, W.J.G., & McGaugh, S.S. 1997, MNRAS, 290, 533
- de Blok, W.J.G., McGaugh, S.S., & Rubin, V. 2001, AJ, 122, 2396
- Dehnen, W., & Binney, J.J, 1998, MNRAS, 298, 387
- de Jong, T. 1977, AA, 55, 137
- de Heij, V., Braun, R., & Burton, W.B. 2002a, AA in press, astro-ph/0206306
- de Heij, V., Braun, R., & Burton, W.B. 2002b, AA in press, astro-ph/0201249
- de Heij, V., Braun, R., & Burton, W.B. 2002c, AA in press, astro-ph/0206333
- Dekel, A., & Silk, J. 1986, ApJ 303, 39
- Dove, J.B., & Shull, J.M. 1994, 430, 222
- Dove, J.B., Shull, J.M., & Ferrara, A. 2000, ApJ 531, 846
- Draine, B.T. 1978, ApJS, 36, 595
- Dwek, E., & Arendt, R. G. 1998, ApJ, 508, L9
- Eichler, D. 1976, ApJ, 208, 694
- Einasto, J., Saar, E., Kaasik, A., & Chernin, A.D. 1974, Nature, 252, 111
- Efstathiou, G. 1992, MNRAS, 256, 43P

- Eke, V. R., Navarro, J.F., & Steinmetz, M. 2001, *ApJ*, 554, 114
- Ferland, G.J., Korista, K.T., Verner, D.A., Ferguson, J.W., Kingdon, J.B., & Verner E.M. 1998, *PASP*, 110, 761
- Ferrara, A., & Field, G. 1994, *ApJ*, 423, 665
- Ferriere, K.M., Zweibel, E.G., & Shull, J.M. 1988, *ApJ*, 332, 984
- Field, G.B., 1975, in “Atomic and Molecular Physics and the Interstellar Medium”, Les Houches lectures, eds. R. Balian, P. Encrenaz, J. Lequeux, (North Holland Publishing), 467
- Field, G.B., Goldsmith, D.W., & Habing, H.J. 1969, *ApJL*, 155, L149
- Firmani, C., D’Onghia, E., Avila-Reese, V., Chincarini, G., & Hernandez, X. 2000, *MNRAS*, 321, 713
- Gallagher III, J.S. 1994, *PASP*, 106, 1225
- Gardiner, L.T., & Noguchi, M. 1996, *MNRAS*, 278, 191
- Gendreau, K. et al. 1995, *PASJ*, 47, L5
- Gibson, B.K., Giroux, M.L., Stocke, J.T., & Shull, J.M. 2000, in *Gas & Galaxy Evolution*, ASP conference series, Hibbard et al. eds.
- Gibson, B.K., Fenner, Y., Maddison, S.T., Kawata, D. 2002 ASP Conference proceedings, eds. J.S. Mulchaey and J. Stocke, 254, p. 225
- Giovanelli, R. 1981, *AJ*, 86, 1468
- Gunn, J., & Gott, R. 1972, *ApJ*, 176, 1
- Haardt, F. & Madau, P. 1996, *ApJ* 461, 20
- Hartmann, D., & Burton, W.B. 1997, *Atlas of Galactic Neutral Hydrogen*, (Cambridge: Cambridge Univ. Press)
- Hasinger, G. 2000, in *ISO Surveys of a Dusty Universe*, eds. D. Lemke, M. Stickel, and K. Wilke (Springer) astro-ph/0001360
- Hoessel, J.G., Saha, A., Krist, J., & Danielson, G.E. 1994, *AJ*, 108, 654
- Hulsbosch, A.N.M., & Wakker, B.P. 1988, *AAS*, 75, 191
- Jenkins, E.B., Jura, M., & Loewenstein, M. 1983, 270. 88
- Garmire, G.P., Nousek, J.A., Apparao, K.M.V., Burrows, D.N., Fink, R.L., & Kraft, R.P. 1992,

- ApJ, 399, 694
- Kaufman, M.J., Wolfire, M.G., Hollenbach, D.J., & Luhman, M.L. 1999, ApJ, 527, 795
- Kennicutt, R.C. 2001, in Galactic Structure, Stars, & the Interstellar Medium C.E. Woodward, M.D. Bica, and J.M. Shull eds., ASP Conference Series, Vol. 231, 2
- Kepner, J.V., Babul, A., & Spergel, D. 1997, ApJ, 487, 61
- Kitayama, T., & Ikeuchi, S. 2000, ApJ, 529, 615
- Klypin, A.A., Kravtsov, A.V., Valenzuela, O. & Prada, F. 1999, ApJ, 522, 82
- Kulkarni, S.R., & Heiles, C. 1987, in Interstellar Processes, ed. D. Hollenbach, & H.A. Thronson, Jr. (Dordrecht, Reidel), 87
- Kulkarni, S.R., & Heiles, C. 1988, in Galactic and Extragalactic Radio Astronomy, ed. G.L. Verschuur, & K.I. Kellermann (New York: Springer) 95
- Kuntz, K.D., & Snowden, S.L. 2000, ApJ, 543, 195
- Lockman, F.J., Murphy, E.M., Petty-Powell, S., & Urick, V.J. 2002, ApJS, 140, 331
- Lu, L., Savage, B.D., Sembach, K.R., Wakker, B.P., Sargent, W.L.W., & Oosterloo, T.A. 1998, AJ, 115, 162
- Madsen, G.J., Reynolds, R.J., Haffner, L.M., Tufte, S.L., & Maloney, P.R. 2001, ApJ, 560, L135
- Makino, N. Sasaki, S., & Suto, Y. 1998, ApJ, 497, 555
- Maloney, P.R. 1993, ApJ, 414, 41
- Martin, C., & Bowyer, S. 1989, ApJ, 338, 667
- Martin, C., Hurwitz, M., & Bowyer, S. 1991, ApJ, 379, 549
- Mateo, M. 1998, ARAA, 36, 435
- Mattila, K. 1990, in Galactic and Extragalactic Background Radiation, IAU Symp No. 139, eds. S. Bowyer and Ch. Leinert (Kluwer: Dordrecht), 257
- Mao, S., & Schneider, P. 1998, MNRAS, 295, 587
- McKee, C.F., & Ostriker, J.P. 1977, ApJ, 218, 148
- Metcalfe, R.B., & Madau, P. 2001, ApJ, 563, L9
- Meyer, D.M., Jura, M., & Cardelli, J.A. 1998, ApJ 493, 222

- Miralda-Escude, J., & Rees, M.J. 1993, MNRAS, 260, 617
- Miyaji, T., Ishisaki, Y., Ogasaka, Y., Freyberg, M.J., Hasinger, G., & Tanaka, Y. 1998, AA, 334, L13
- Moore, B. 1994, Nature, 370, 629
- Moore, B., & Davis, M. 1994, MNRAS, 270, 209
- Moore, B., Ghigna, S., Governato, G., Lake, G., Quinn, T., Stadel, J., & Tozzi, P. 1999, ApJ, 524, 19
- Moore, B., & Putman, M.E. 2001, astro-ph/0110417
- Mori, M., & Burkert, A. 2000, 538, 559
- Morrison, R., & McCammon, D. 1983, ApJ 270, 119
- Muller, C.A., Oort, J.H., & Raimond, E. 1963, C.R. Acad. Sci. Paris, 257, 1661
- Murakami, I., & Ikeuchi, S. 1990, PASJ, 42, L11
- Murphy, E.M., et al. 2000, ApJ, 538, 35
- Navarro, J.F., Frenk, C.S., & White, S.D.M. 1996, ApJ, 462, 563
- Navarro, J.F., Frenk, C.S., & White, S.D.M. 1997, ApJ, 490, 493
- Navarro, J.F., & Steinmetz 2000, ApJ, 528, 607
- Okoshi, K., & Ikeuchi, S. 1996, PASJ, 48, 441
- Olive, K.A., & Steigman, G. 1995, ApJS, 97, 49
- Oort, J. 1966, Bull. Astr. Inst. Netherlands, 18, 421
- Oort, J. 1970, AA, 7, 381
- Peebles, P.J.E. 1982, ApJ, 263, L1
- Press, W.H., & Schechter, P. 1974, ApJ, 187, 425
- Putman, M.E., et al. 2002, AJ, 123, 873
- Quilis, V., & Moore, B. 2001, ApJ 555, L95
- Rees, M.J. 1986, MNRAS, 218, 25P
- Roberge, W.G., Dalgarno, A., & Flannery, B.P. 1981, ApJ, 245, 817

- Rosenberg, J.L., & Schneider, S.E. 2002, ApJ 567 247
- Sembach, K.R. 2002, in Extragalactic Gas at Low Redshift, ASP Conference proceedings, eds. J.S. Mulchaey and J. Stocke, 254, p. 283
- Sembach, K.R., Savage, B.D., Lu, L., & Murphy, E.M. 1999, ApJ, 515, 108
- Sembach, K.R., et al. 2000, ApJ, 538, L31
- Shapiro, P.R., & Field, G.B. 1976, ApJ 205, 762
- Shull, J.M., Roberts, D., Giroux, M.L., Penton, S.V., & Fardal, M.A. 1999, AJ, 118, 1450
- Shull, J.M., & van Steenberg, M.E. 1985, ApJ 298, 268
- Silk, J., & Sunyaev, R.A. 1976, Nature, 260, 508
- Skillman, E.D., Kennicutt, R.C., & Hodge, P.W. 1989, ApJ, 347, 875
- Skillman, E.D., Terlevich, R., & Melnick, J. 1989, MNRAS, 240, 563
- Slavin, J.D., McKee, C.F., & Hollenbach, D.J. 2000, ApJ, 541, 218
- Snowden, S.L., Freyberg, M.J., Kuntz, K.D., & Sanders, W.T. 2000, ApJS, 128, 171
- Spitzer, L. 1987, in Dynamical Evolution of Globular Clusters (Princeton University Press, Princeton) 13.
- Sternberg, A. 1998, ApJ, 506, 721
- Sunyaev, R.A., 1969, ApL, 3, 33
- Tegmark, M., Silk, J., & Evrard, A. 1993, AJ, 417, 54
- Thoul, A.A., & Weinberg, D. 1996, ApJ, 465, 608
- Tielens, A.G.G.M., Hony, S., van Kerckhoven, C. & Peeters, E. 1999, in The Universe as Seen by ISO, eds. P. Cox and M.F. Kessler, ESA-SP 427, (Noordwijk: ESA), 579
- Tolstoy, E. et al. 1998, AJ, 116, 1244
- Tufte, S.L., Reynolds, R.J., & Haffner, L.M. 1998, ApJ, 504, 773
- Tufte, S.L., Wilson, J.D., Madsen, G.J., Haffner, L.M., & Reynolds, R.J. 2002, ApJL, in press (astro-ph/0206198)
- van den Bergh, S. 1999, AAR, 9, 273
- van den Bosch, F.C., Robertson, B.E., Dalcanton, J.J., & de Blok, W.J.G. 2000, ApJ, 119, 1579

- van den Bosch, F.C., & Swaters, R.A. 2001 MNRAS, 325, 101
- van Woerden, H., Schwarz, U.J., Peletier, R., Wakker, B.P. & Kalbera, P.M.W. 1999, Nature 400, 138
- Verschuur, G.L. 1969, ApJ, 156, 771
- Vogel, S.N., Weymann, R. Rauch, M., & Hamilton, T. 1995, ApJ, 441, 162
- Wakker, B.P., & Boulanger, F. 1986, AA, 170, 84
- Wakker, B.P., & Schwarz, U.J. 1991, AA, 250, 484
- Wakker, B.P., & van Woerden, H. 1991, AA, 250, 509
- Wakker, B.P., & van Woerden, H. 1997, ARA&A, 35, 217 in Stromlo Workshop on High-Velocity Clouds, eds. Gibson, B.K. and Putman, M.E., ASP conference series, 166, 311
- Wakker, B.P., van Woerden, H., & Gibson, B.K. 1999, in Stromlo Workshop on High Velocity Clouds, eds. B.K. Gibson, and M.E. Putman, ASP Conference series, 166, p. 311
- Wakker, B.P., et al. 1999, Nature, 402, 388
- Weiner, B.J., & Williams, T.B. 1996, AJ, 111, 1156
- Weiner, B.J., Vogel, S.N., & Williams, T.B. 2001, in Gas & Galaxy Evolution, eds. J.E. Hibbard, M.P. Rupen and J.H. van Gorkom, ASP Conference series, San Francisco, Astronomical Society of the Pacific, 515
- Weymann, R.J., Vogel, S.N., Veilleux, S., & Epps, H.W. 2001, ApJ, 561, 559
- White, S.D.M., & Rees, M.J., 1978, MNRAS, 183, 341
- Wishart, A.W. 1979, MNRAS, 187, 59
- Wolfire, M.G., Hollenbach, D., McKee, C.F., Tielens, A.G.G.M., & Bakes, E.L.O. 1995a, ApJ, 443, 152
- Wolfire, M.G., McKee, C.F., Hollenbach, D., & Tielens, A.G.G.M. 1995b, ApJ, 453, 673
- Wolfire, M.G., McKee, C.F., Hollenbach, D., & Tielens, A.G.G.M. 2002, ApJ submitted
- Wu, X.-P., & Xue, Y.-J. 2000, ApJ, 542, 578
- Wu, X.-P. 2000, MNRAS, 316, 299
- Young, L.M., & Lo, K.Y. 1996, ApJ, 462, 203
- Young, L.M., & Lo, K.Y. 1997, ApJ, 490, 710

Zeldovich, Y.B., & Pilkelner, S.B. 1969, Soviet Physics JETP, 29, 170

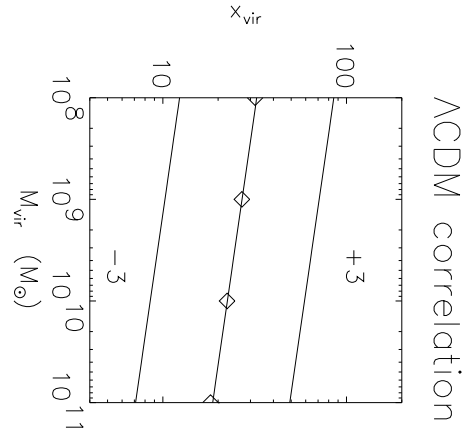
Zwaan, M., & Briggs, F.H. 2000, ApJ, 530, L61

List of Figures

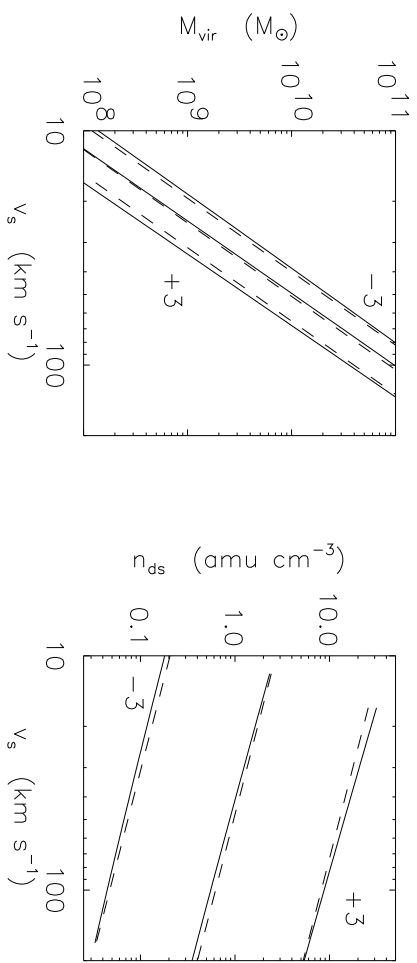
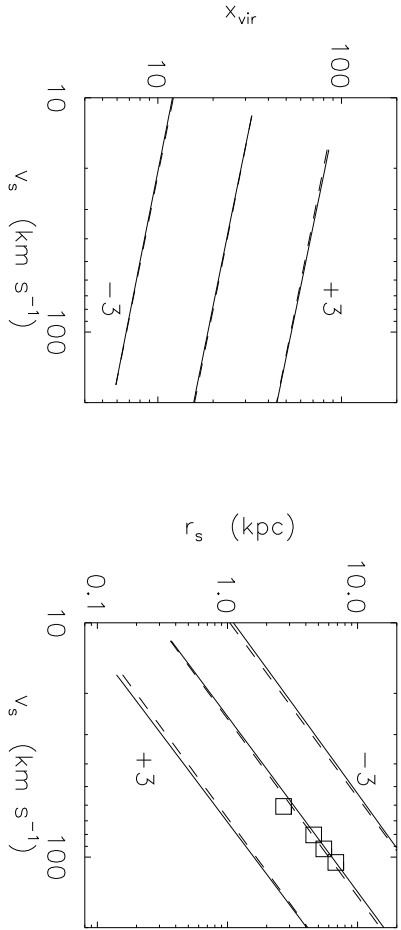
1	The Λ CDM correlation relation, $x_{\text{vir}}(M_{\text{vir}})$, between the halo concentration and virial mass for low-mass halos. The square symbols indicate the values computed using the Bullock et al. (2001) model. The solid lines are our fits (as given by eq. [15]) for median, $+3\sigma$ over-concentrated, and -3σ under-concentrated, halos.	67
2	Λ CDM scalings for NFW and Burkert halos. The halo parameters, for median $+3\sigma$ and -3σ halos, are displayed as function of the scale velocity v_s : (a) concentration parameter x_{vir} , (b) virial mass M_{vir} , (c) scale radius r_s , and (d) characteristic density n_{ds} . The dashed lines show the analytic scalings given by equations (16), (17), (18) and (19). The square symbols in panel (c) show the observed correlation between r_s and v_s for the dwarf galaxies DDO 154, DDO 179, NGC 3109, and DDO 105 (Burkert 1995).	68
3	Metagalactic radiation field from $1.6\mu\text{m}$ to 3 keV. See Appendix B for a discussion of this fit.	69
4	Thermal properties of low metallicity ($Z = 0.1Z_{\odot}$) HI gas heated by a radiative flux equal to $2\pi J_{\nu}$, where J_{ν} is the metagalactic radiation intensity (see Appendix B). The assumed HI shielding column is $N_{\text{HI}} = 5 \times 10^{19} \text{ cm}^{-2}$, and the thermal properties are displayed as functions of the hydrogen gas density n_{H} : (a) pressure vs. density phase diagram indicating the WNM and CNM branches, and the critical pressures, P_{min} and P_{max} , within which thermal instability and multi-phased behavior occurs, (b) gas heating rates (dashed) and cooling rates (solid), (c) fractional ionization, and (d) HI gas temperature. 70	70
5	The HI thermal phase properties as functions of the shielding column N_{HI} : (a) phase diagrams for N_{HI} between 10^{18} and 10^{21} cm^{-2} , (b) the critical pressures P_{min} and P_{max} as functions of the primary ionization rate ζ_p (s^{-1}). The upper axis in panel (b) indicates the associated HI shielding columns (cm^{-2}) for a plane-parallel geometry.	71

6	<p>M_{WM} vs. M_{vir} diagrams for 10^4 K WM clouds in median ($\sigma = 0$) Burkert halos, and a bounding pressure $P_{\text{HIM}} = 1 \text{ cm}^{-3} \text{ K}$: (a) total cloud radius $r_{\text{W/H}}$, (b) the ratio, $M_{\text{WM}}/M_{\text{DM}}$, of the WM cloud mass and enclosed DM mass, (c) WNM radius r_{WNM}, (d) total HI gas mass, (e) peak HI column density, (f) central pressure. The dotted curves in panels (c) and (e) indicate the locus of critical clouds. The thick solid curves in panels (b), (c) and (f) indicate marginally bound clouds. The dashed curves in panel (f) indicate the “multi-phased strip” within which multi-phased behavior is possible in the cloud cores.</p>	72
7	<p>M_{WM} vs. M_{vir} diagrams for median ($\sigma = 0$) Burkert halos, and $P_{\text{HIM}} = 10 \text{ cm}^{-3} \text{ K}$.</p>	73
8	<p>M_{WM} vs. M_{vir} diagrams for median ($\sigma = 0$) Burkert halos, and $P_{\text{HIM}} = 100 \text{ cm}^{-3} \text{ K}$.</p>	74
9	<p>M_{WM} vs. M_{vir} diagrams for -4σ NFW halos, and $P_{\text{HIM}} = 1 \text{ cm}^{-3} \text{ K}$.</p>	75
10	<p>M_{WM} vs. M_{vir} diagrams for -4σ NFW halos, and a bounding pressure $P_{\text{HIM}} = 10 \text{ cm}^{-3} \text{ K}$.</p>	76
11	<p>M_{WM} vs. M_{vir} diagrams for -4σ NFW halos, and $P_{\text{HIM}} = 100 \text{ cm}^{-3} \text{ K}$.</p>	77
12	<p>Median $M_{\text{vir}} = 2 \times 10^9 M_{\odot}$ (or $v_s = 30 \text{ km s}^{-1}$) Burkert halo model for the dwarf galaxies Leo A and Sag DIG: (a) WM and HI gas densities (solid curves), and the sum of the DM and stellar densities (dashed curve) as functions of the cloud radius r, (b) projected HI column density N_{HI}, and the average HI column, $\langle N_{\text{HI}} \rangle$, within r, (c) enclosed WM and HI gas masses (solid), and enclosed DM plus stellar masses (dashed), (d) $\text{H}\alpha$ recombination line surface brightness, and (e) WM gas pressure, P_{WM}, and the critical pressures P_{min} and P_{max}, and (f) total (solid) and primary (dashed) hydrogen ionization rates.</p>	78
13	<p>Circumgalactic CHVC model. Median Burkert halo, with $M_{\text{vir}} = 1 \times 10^8 M_{\odot}$ (or $v_s = 12 \text{ km s}^{-1}$), and $P_{\text{HIM}}/k = 50 \text{ cm}^{-3} \text{ K}$. (a) WM and HI gas densities (solid curves), and the DM density (dashed curve) as functions of the cloud radius r, (b) projected HI column density N_{HI}, and the average HI column within r, the dotted curve is the HI column density for an exponential HI gas density distribution (see text), (c) enclosed WM and HI gas masses (solid), and DM mass (dashed), (d) $\text{H}\alpha$ recombination line surface brightness, (e) WM gas pressure, P_{WM}, and the critical pressures P_{min} and P_{max}, and (f) total (solid) and primary (dashed) hydrogen ionization rates.</p>	79
14	<p>Galactic HIM pressure for a $T_{\text{HIM}} = 2 \times 10^6 \text{ K}$ corona.</p>	80

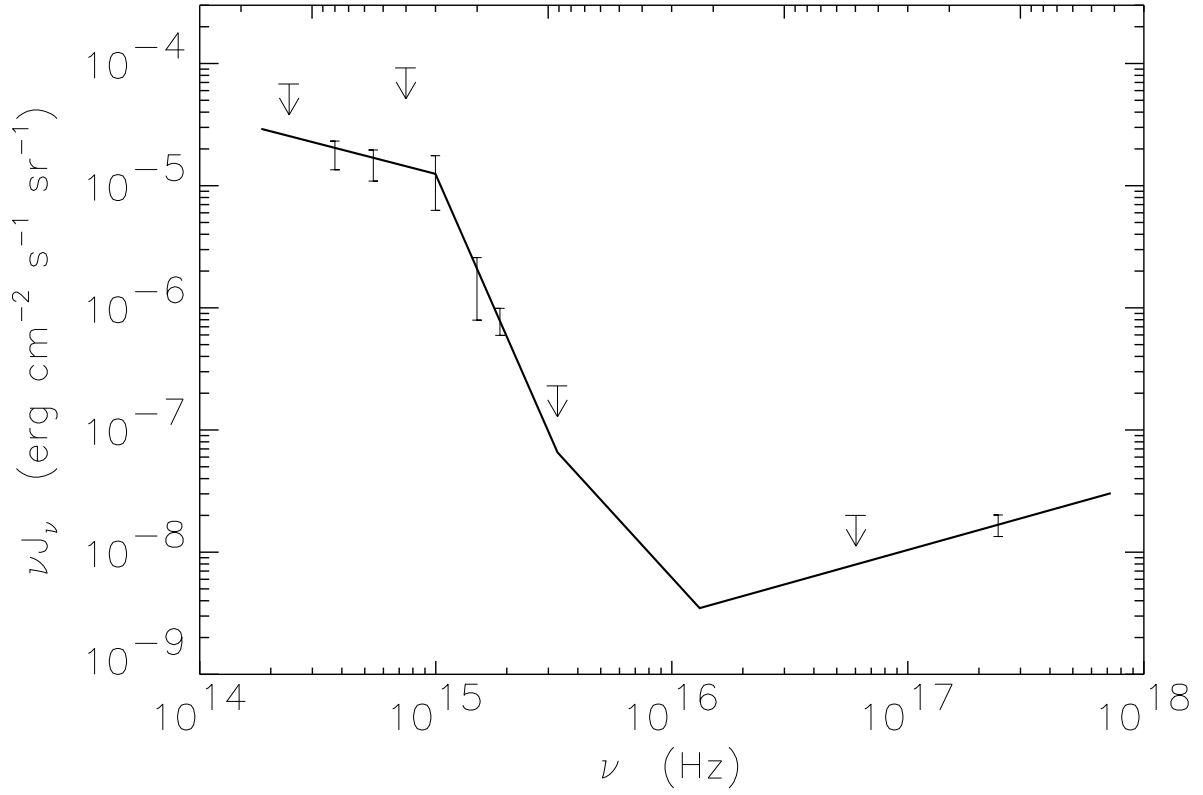
- 15 Extragalactic CHVC model. -4σ Burkert halo, with $M_{\text{vir}} = 1 \times 10^8 M_{\odot}$ (or $v_s = 12 \text{ km s}^{-1}$), and $P_{\text{HIM}}/k = 20 \text{ cm}^{-3} \text{ K}$. (a) WM and HI gas density distributions (solid curves), and the DM densities (dashed curve), (b) projected HI column density N_{HI} , and the average HI column within r , the dotted curve is the HI column density for an exponential HI gas density distribution (see text), (c) enclosed WM and HI gas masses (solid), and enclosed DM plus stellar masses (dashed), (d) $\text{H}\alpha$ recombination line surface brightness, (e) WM gas pressure, P_{WM} , and the critical pressures P_{min} and P_{max} , and (f) total (solid) and primary (dashed) hydrogen ionization rates. 81
- 16 The small- x $1/e$ gas scale height r_{gas} for a 10^4 K WNM in NFW halos: (a) r_{gas} for median, $+3\sigma$, and -3σ halos as a function of v_s , (b) r_{gas} as a function of M_{vir} , (c) level curves for r_{gas} as a function of σ and v_s , and (d) level curves for r_{gas} as a function of σ and M_{vir} . The dashed curves in panels (a) and (b) display the scale height as given by the analytic expressions in Table 6. . . . 82
- 17 The small- x $1/e$ gas scale height r_{gas} for a 10^4 K WNM in Burkert halos: (a) r_{gas} for median, $+3\sigma$, and -3σ halos as a function of v_s , (b) r_{gas} as a function of M_{vir} , (c) level curves for r_{gas} as a function of σ and v_s , and (d) level curves for r_{gas} as a function of σ and M_{vir} . The dashed curves in panels (a) and (b) display the scale height as given by the analytic expressions in Table 6. . . . 83

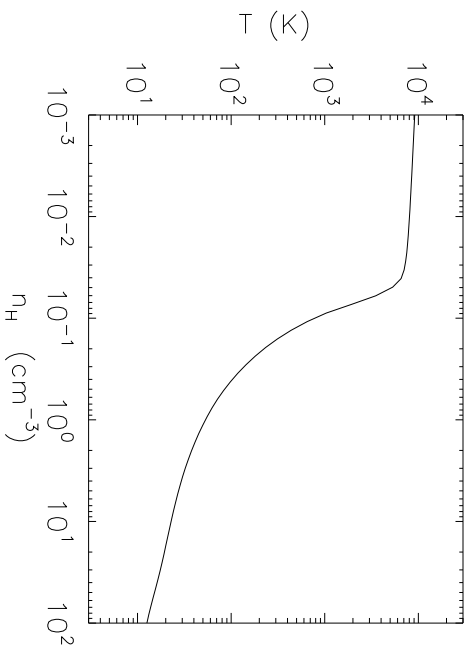
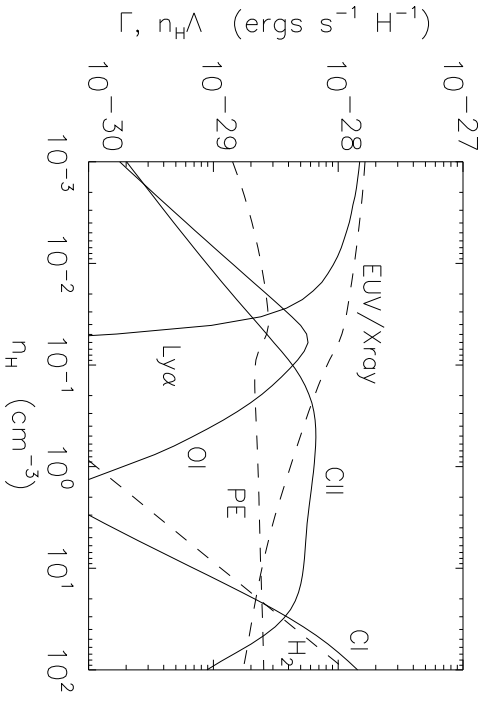
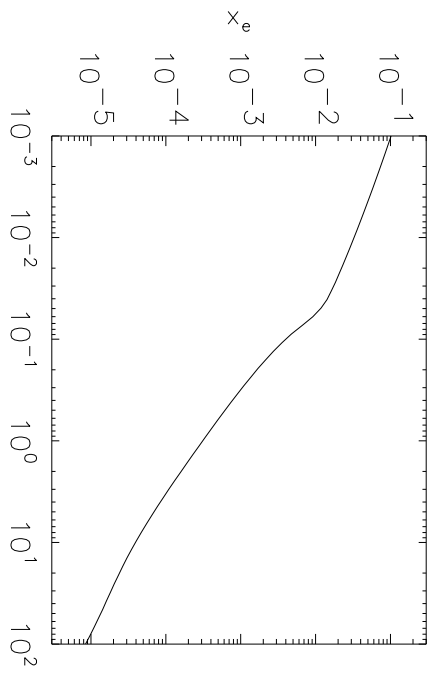
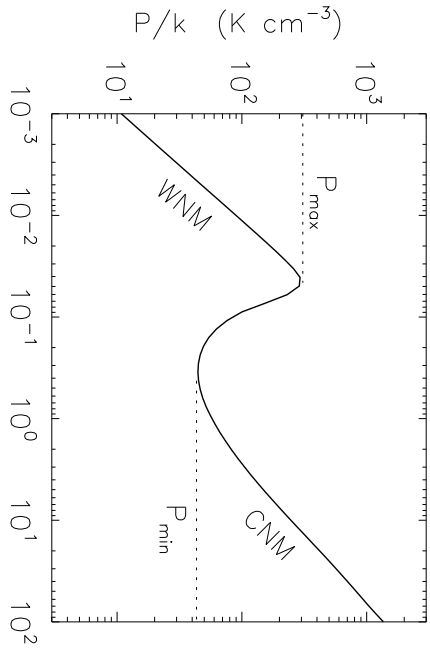


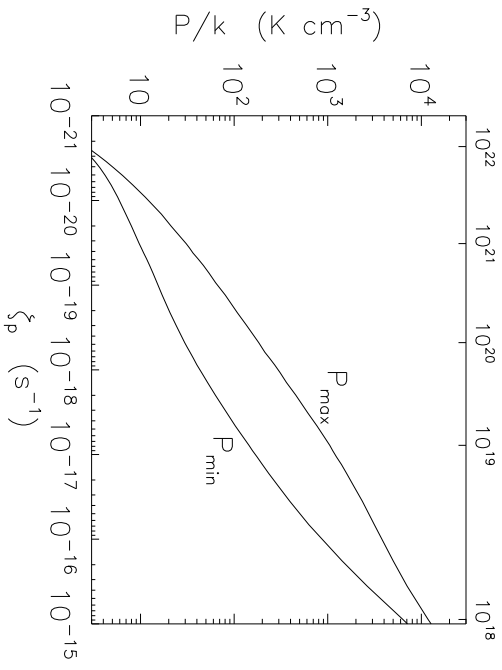
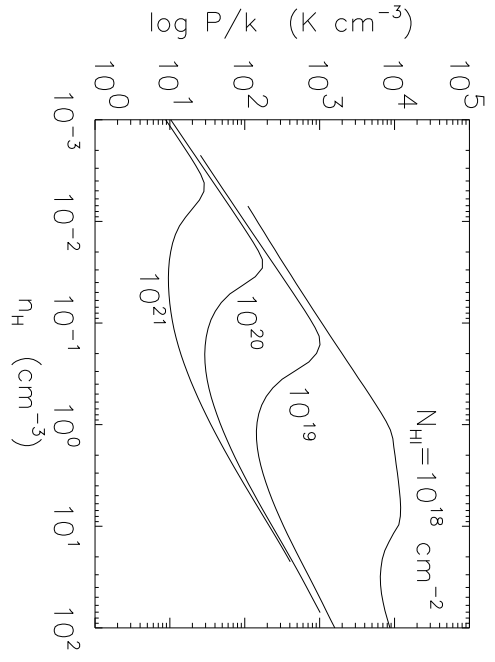
NFW & Burkert halo scaling relations



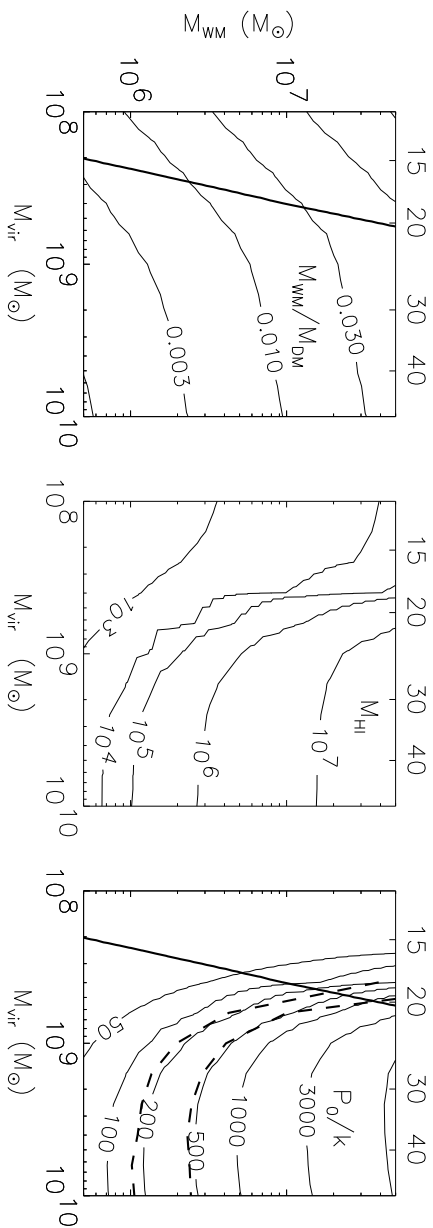
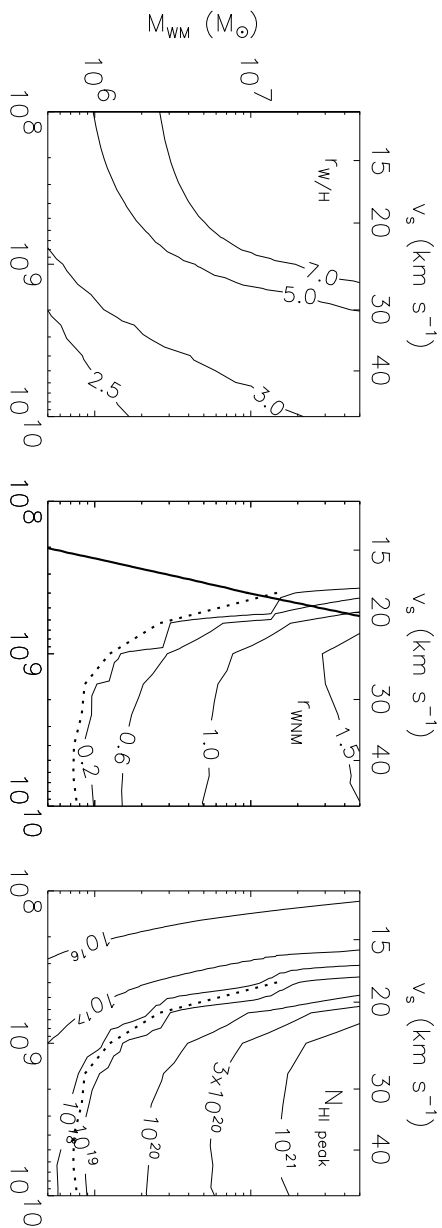
Metagalactic field from $1.6 \mu\text{m}$ to 3 keV
 $1 \mu\text{m}$ 1000 \AA 100 \AA 10 \AA



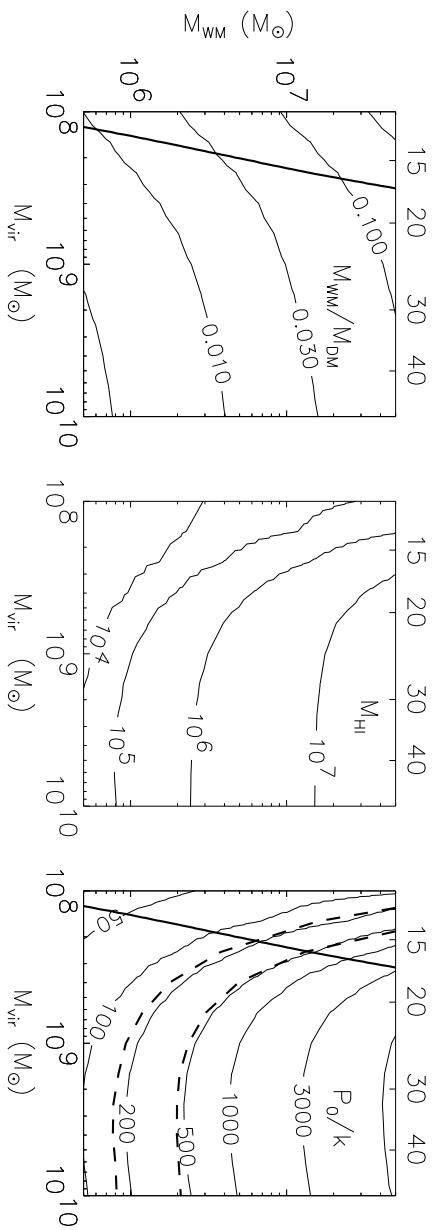
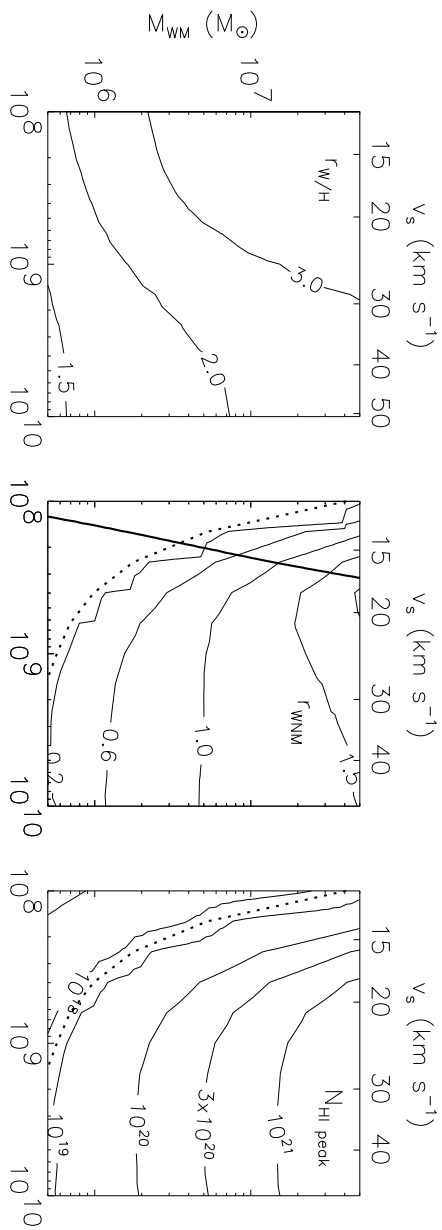




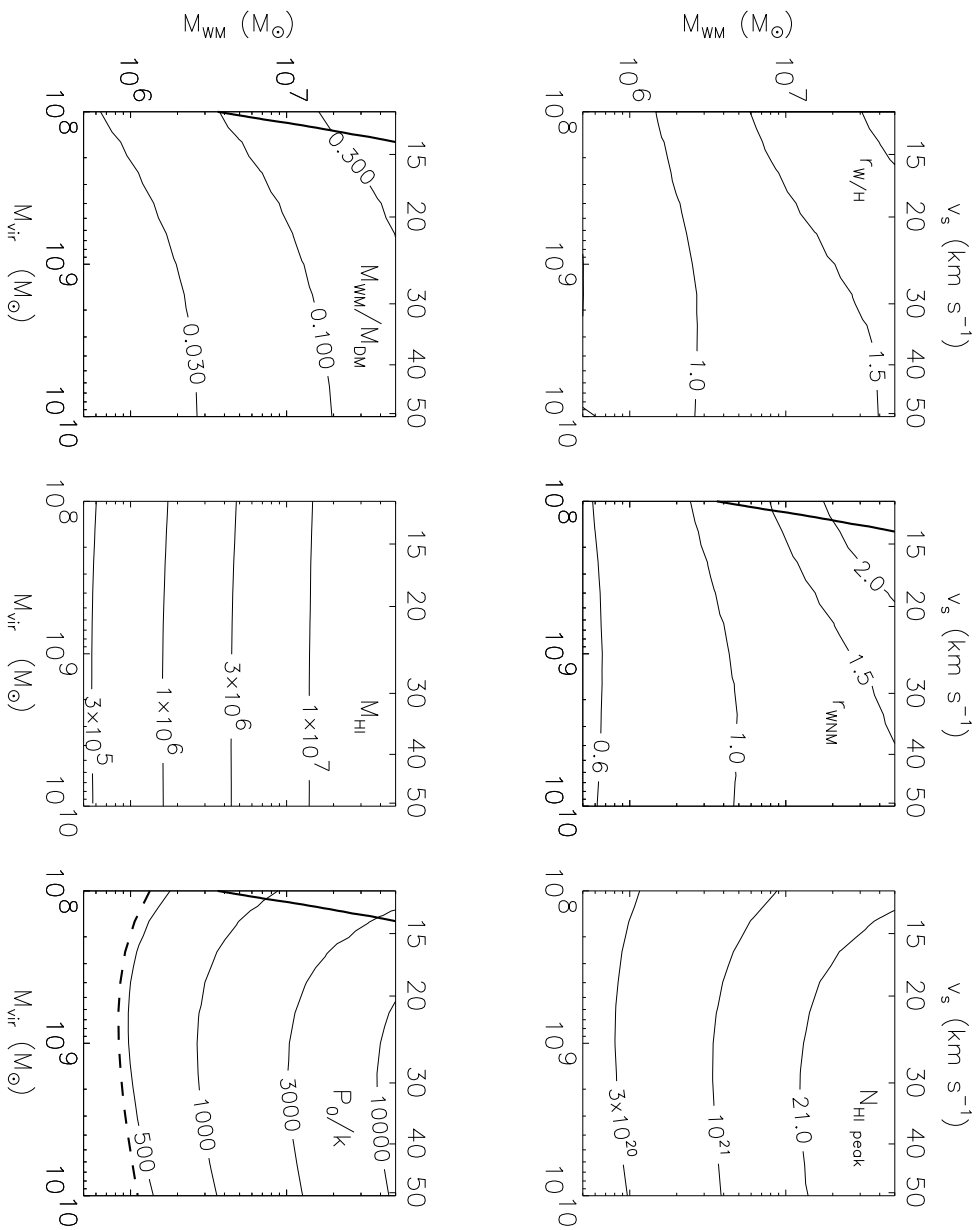
$P_{\text{HI}}/k=1 \text{ cm}^{-3} \text{ K}$ median Burkert halos



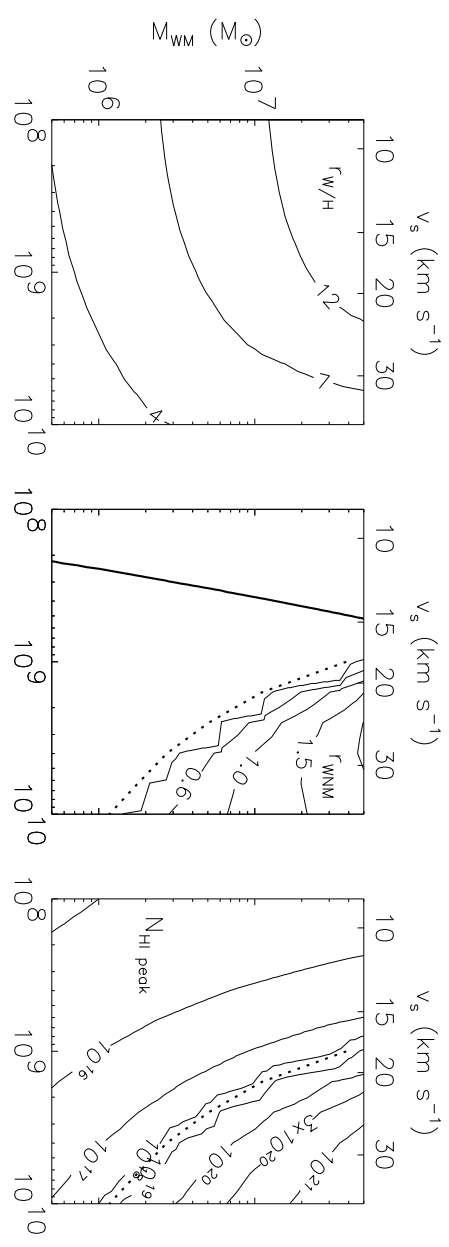
$P_{\text{HIW}}/k=10 \text{ cm}^{-3} \text{ K}$ median Burkert halos



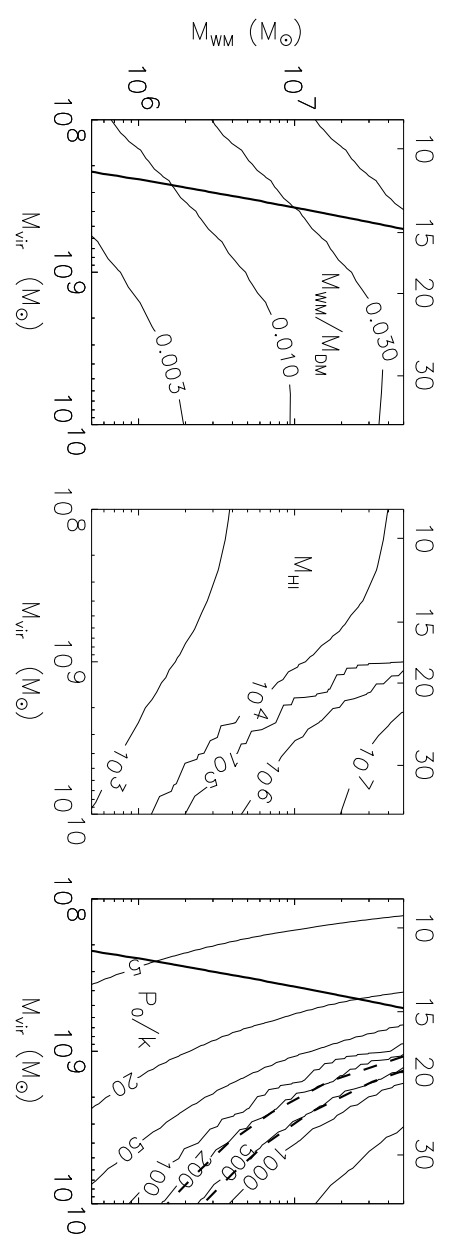
$P_{\text{HIW}}/k=100 \text{ cm}^{-3} \text{ K}$ median Burkert halos



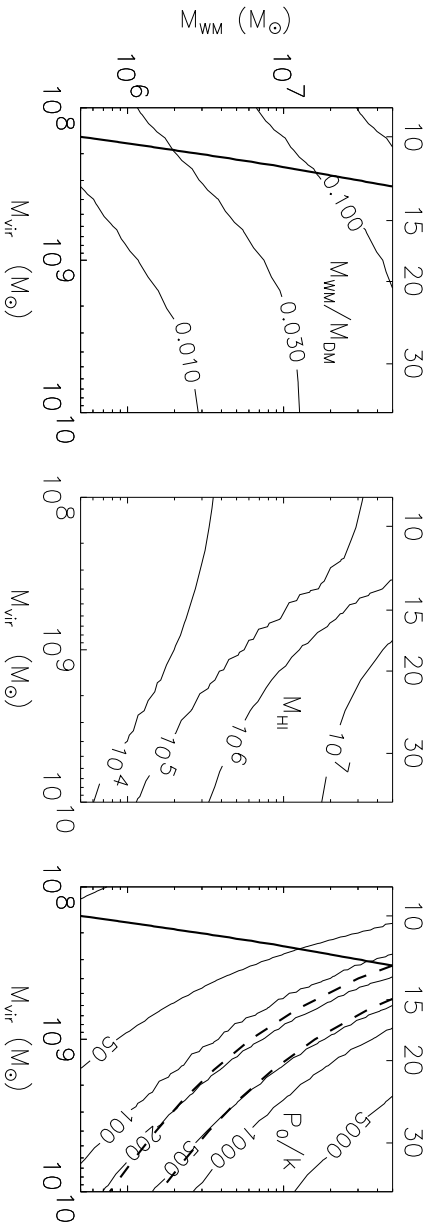
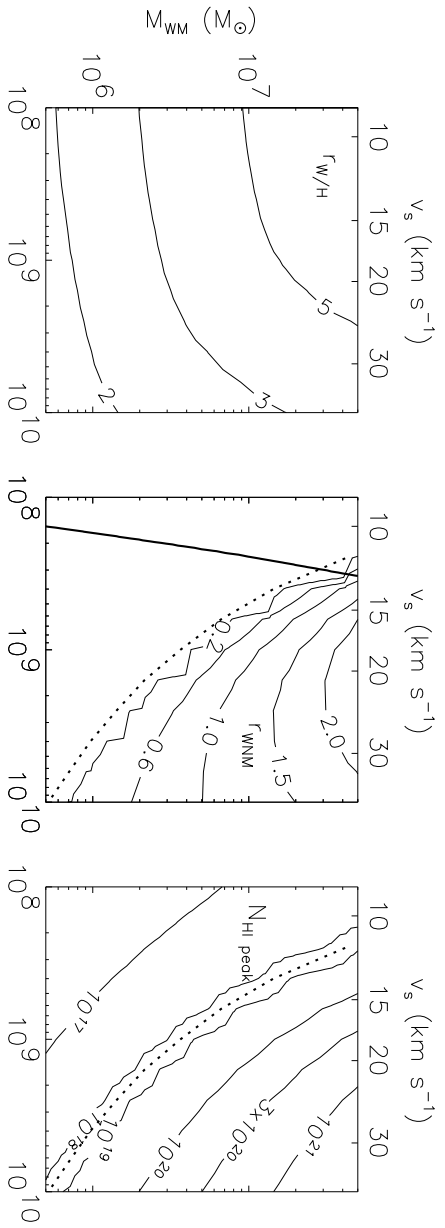
$P_{\text{HII}}/k=1 \text{ cm}^{-3} \text{ K}^{-1}$ -4σ NFW halos



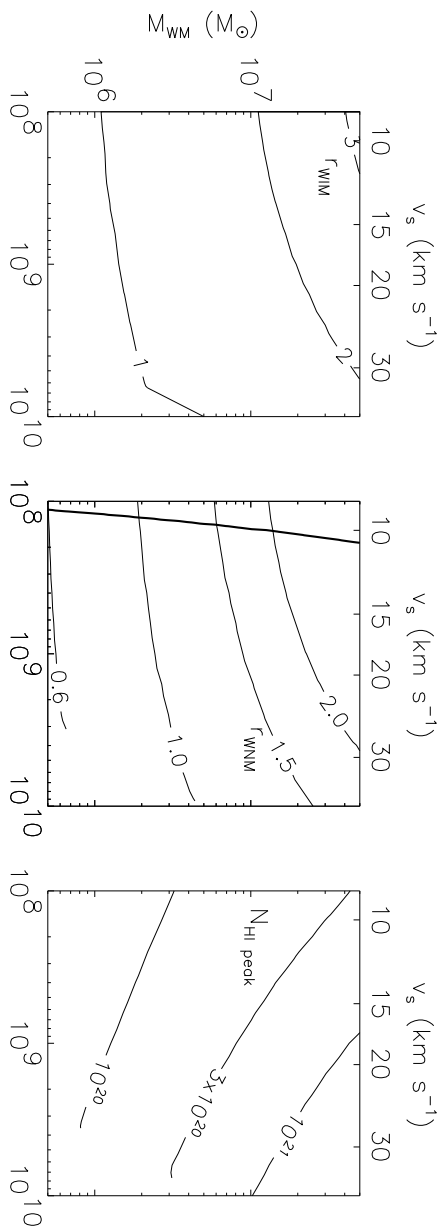
- 75 -



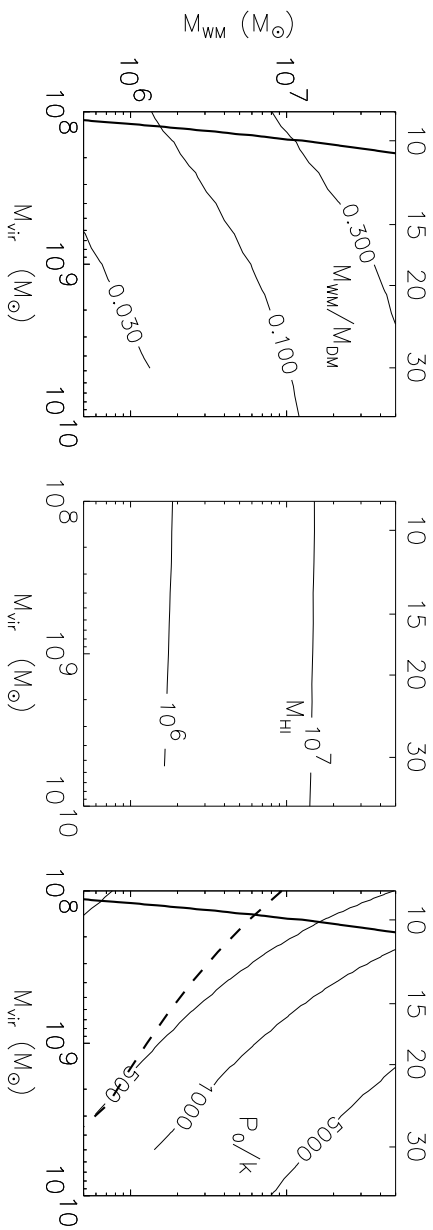
$P_{\text{HII}}/k=10 \text{ cm}^{-3} \text{ K}^{-4\sigma}$ NFW halos



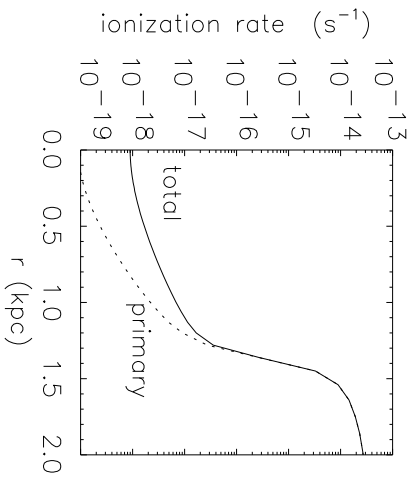
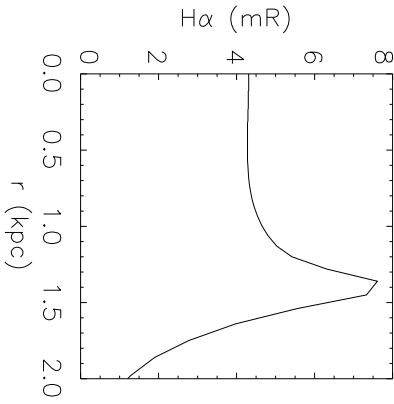
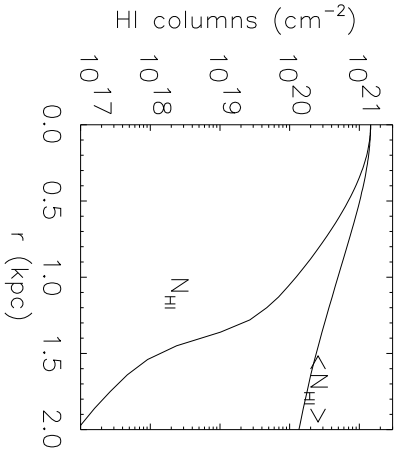
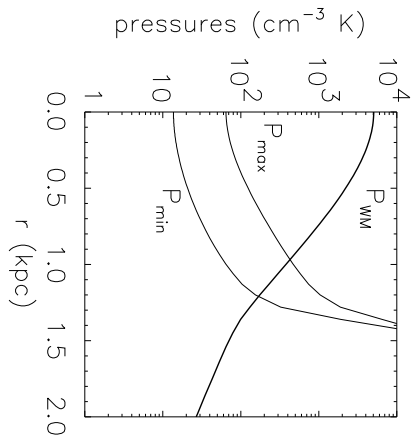
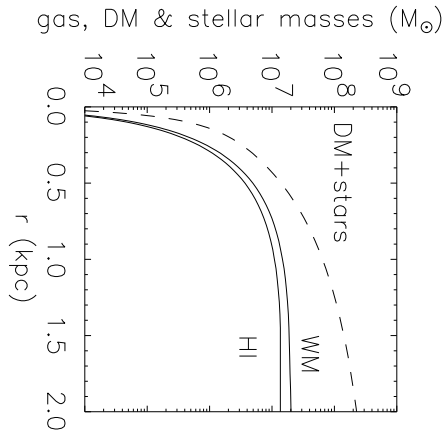
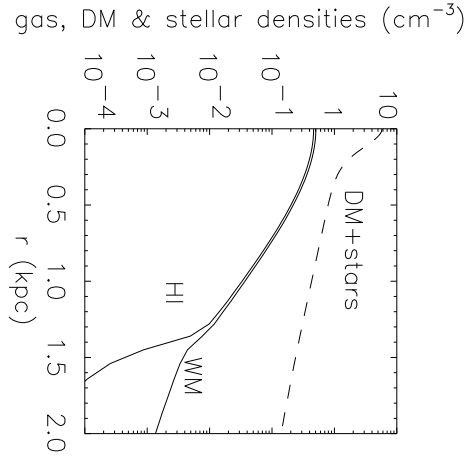
$P_{\text{HIM}}/k=100 \text{ cm}^{-3} \text{ K} \quad -4\sigma \text{ NFW halos}$



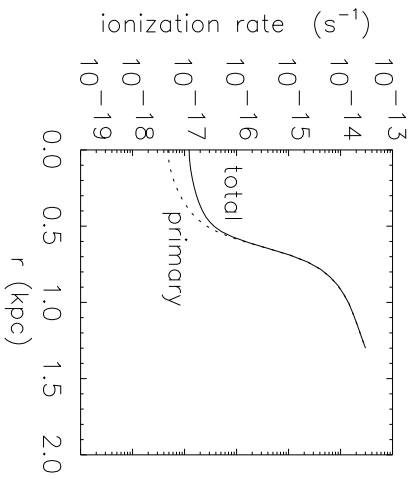
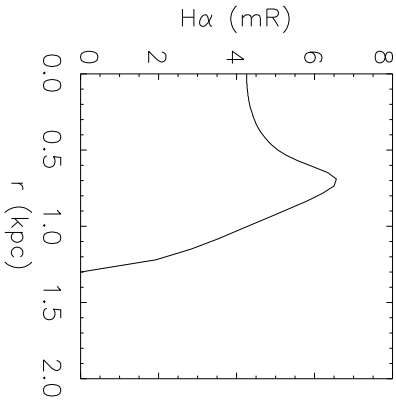
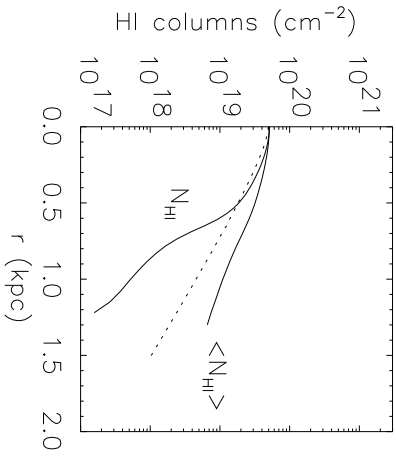
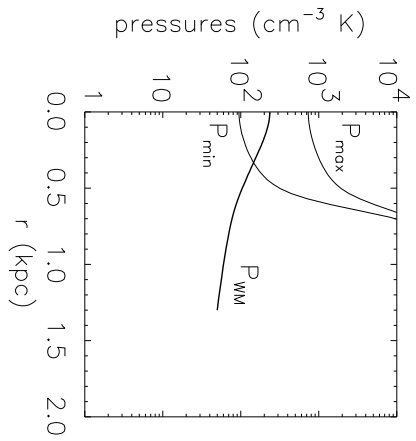
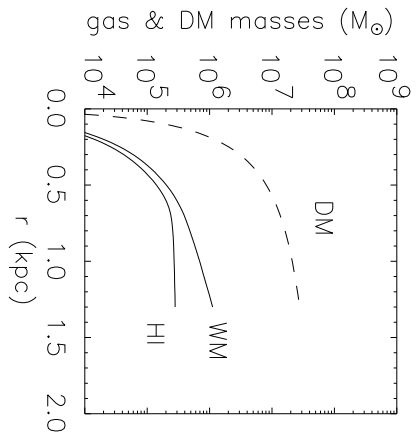
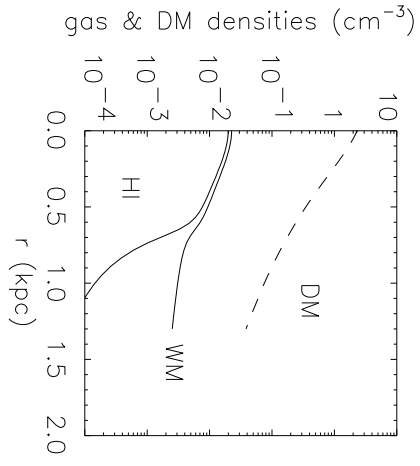
- 77 -

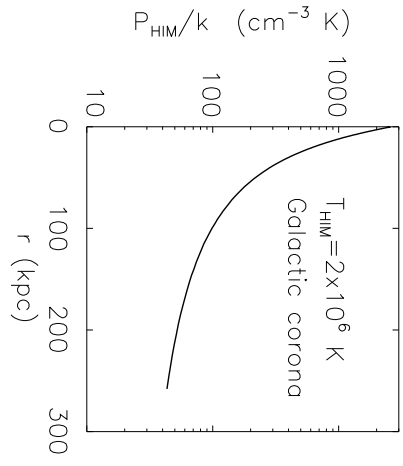


median Burkert Dwarf: $M_{\text{vir}}=2.0 \times 10^9 M_{\odot}$ $v_s=30.0 \text{ km s}^{-1}$ $M_{\text{WM}}=2.2 \times 10^7 M_{\odot}$ $P_{\text{HIM}}=1 \text{ cm}^{-3} \text{ K}$

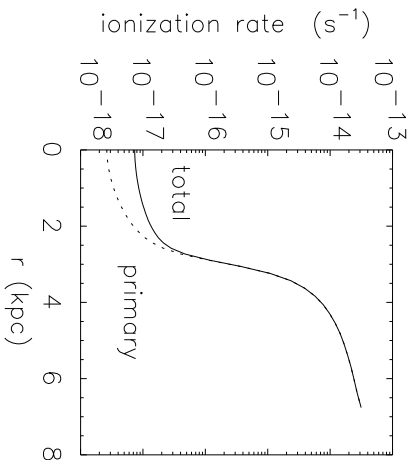
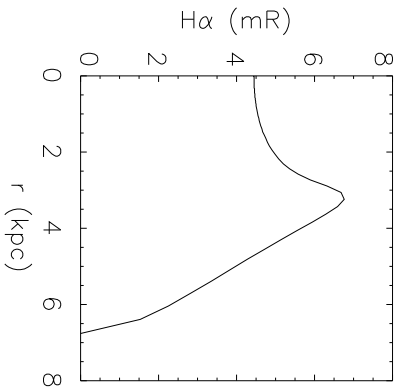
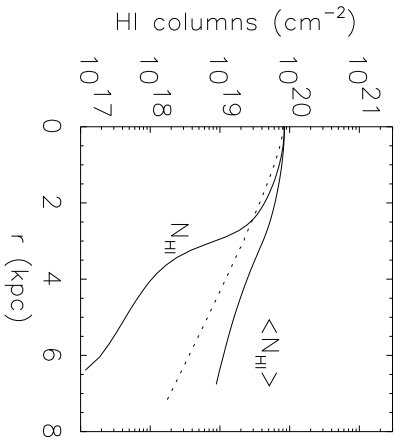
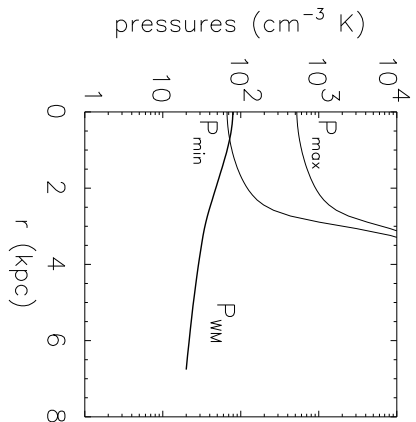
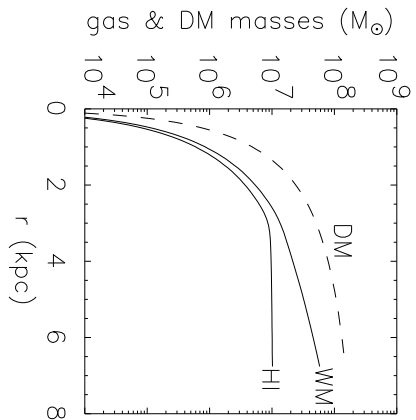
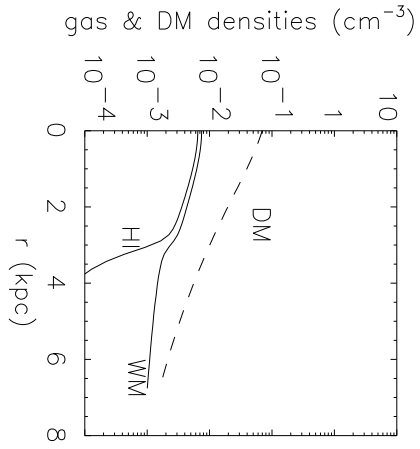


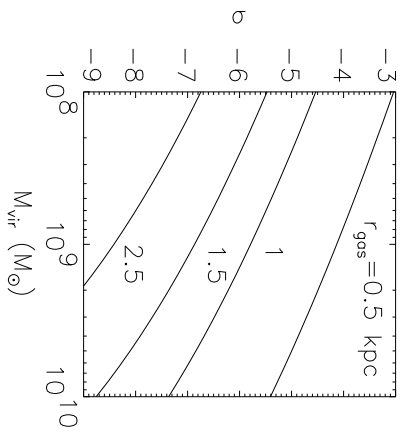
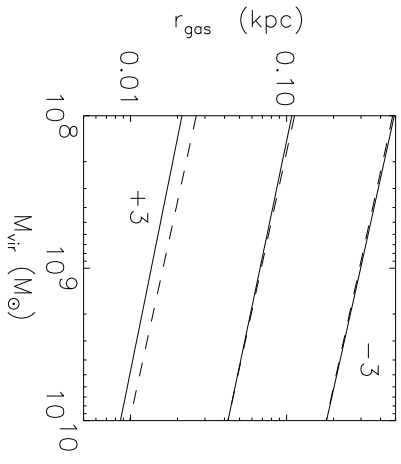
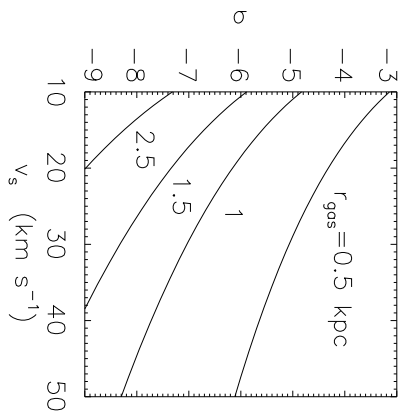
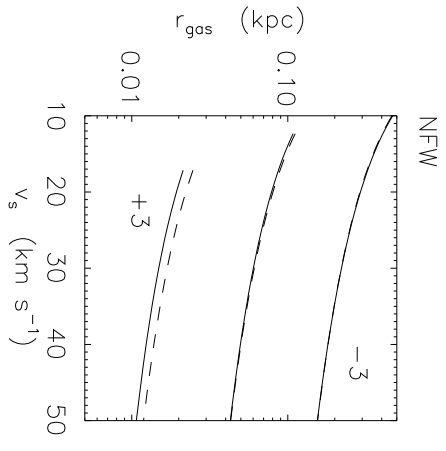
HVC model: median Burkert halo $M_{vir}=1 \times 10^8 M_{\odot}$ $M_{WM}=1.1 \times 10^6 M_{\odot}$ $P_{HI}=50 \text{ cm}^{-3} \text{ K}$
 $x_{vir}=32.5$ $v_s=11.9 \text{ km s}^{-1}$ $r_s=0.37 \text{ kpc}$ $n_s=2.3 \text{ amu cm}^{-3}$
 $r_{WM}=1.3 \text{ kpc}$ $M_{DM}=2.8 \times 10^7 M_{\odot}$





HVC model: -4σ Burkert halo $M_{\text{vir}}=3 \times 10^8 M_{\odot}$ $M_{\text{WM}}=5.8 \times 10^7 M_{\odot}$ $P_{\text{HIM}}=20 \text{ cm}^{-3} \text{ K}$
 $x_{\text{vir}}=8.15$ $v_s=12.1 \text{ km s}^{-1}$ $r_s=2.17 \text{ kpc}$ $n_s=0.070 \text{ amu cm}^{-3}$
 $r_{\text{WM}}=6.8 \text{ kpc}$ $M_{\text{DM}}=1.5 \times 10^8 M_{\odot}$





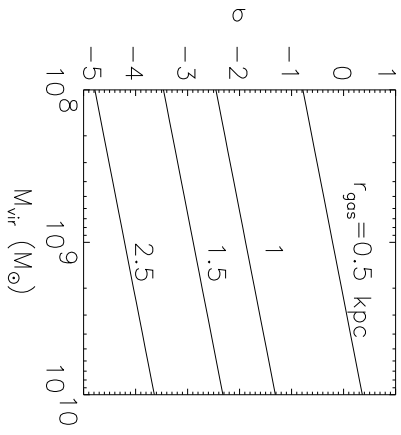
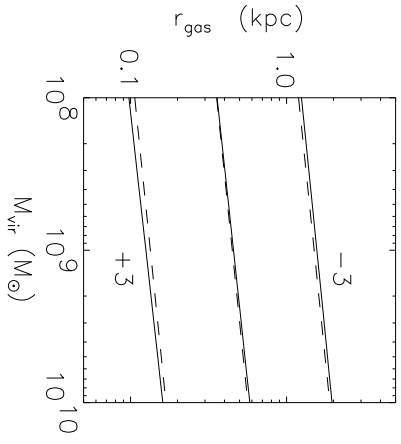
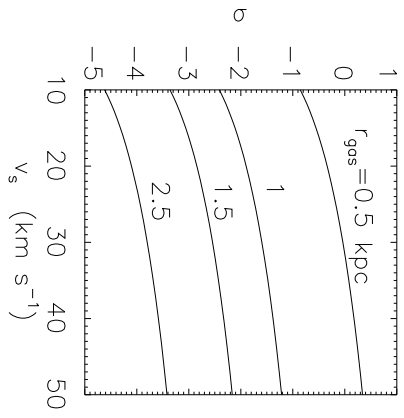
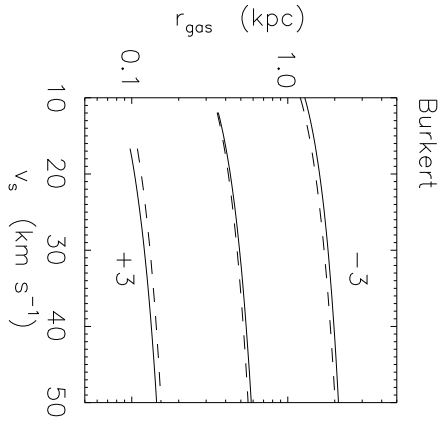


Table 1. Dwarf Galaxies: Observations

	unit	Leo A	Sag DIG
distance	kpc	690	1061
optical core radius	kpc	0.185	0.125
L_V	$10^7 L_\odot$	3.0	6.9
single dish 21 cm flux	Jy km s ⁻¹	69	33
VLA 21 cm flux	Jy km s ⁻¹	65	30
WNM velocity dispersion	km s ⁻¹	9.0	9.5
WNM mass fraction		0.80	0.83
N_{HIpeak} (WNM)	cm ⁻²	2.2×10^{21}	1.0×10^{21}
θ_{gas} (projected)	arcsec	160	70
r_{NHI}	kpc	0.5	0.4
N_{HImin}	cm ⁻²	2×10^{19}	5×10^{18}
r_{HImin}	kpc	1.1	1.6

Table 2. Dwarf Model: median Burkert halo

Halo Parameters		
x_{vir}		25.6
M_{vir}	M_{\odot}	2.0×10^9
r_{vir}	kpc	32.5
n_{ds}	amu cm^{-3}	1.24
r_s	kpc	1.27
v_s	km s^{-1}	30.0
M_{ds}	M_{\odot}	2.67×10^8
$r_{\text{gas}} (\text{small-}x)$	kpc	0.49
Gas Input Parameters		
P_{HIM}/k	$\text{cm}^{-3} \text{ K}$	1.0
M_{WM}	M_{\odot}	2.2×10^7
$M_{\text{WM}}/M_{\text{vir}}$		1.1×10^{-2}
Gas Output Parameters		
$r_{\text{W/H}}$	kpc	4.44
$r_{\text{gas}} (\text{numerical})$	kpc	0.56
r_{NHI}	kpc	0.59
r_{WNM}	kpc	1.39
N_{HIpeak}	cm^{-2}	1.42×10^{21}
M_{HI}	M_{\odot}	1.34×10^7
\mathcal{W}/\mathcal{T}		4.4
P_0/P_{HIM}		4.97×10^3
$n_{\text{H},0}$	cm^{-3}	0.46

Table 3. CHVC Circumgalactic median Burkert halo

Halo Parameters		
x_{vir}		32.5
M_{vir}	M_{\odot}	1.0×10^8
r_{vir}	kpc	12.0
n_{ds}	amu cm^{-3}	2.33
r_s	kpc	0.37
v_s	km s^{-1}	11.9
M_{ds}	M_{\odot}	1.22×10^7
$r_{\text{gas}} (\text{small-}x)$	kpc	0.36
Gas Input Parameters		
P_{HIM}/k	$\text{cm}^{-3} \text{ K}$	50.0
M_{WM}	M_{\odot}	1.1×10^6
$M_{\text{WM}}/M_{\text{vir}}$		1.1×10^{-2}
Gas Output Parameters		
$r_{\text{W/H}}$	kpc	1.30
$r_{\text{gas}} (\text{numerical})$	kpc	0.55
r_{NHI}	kpc	0.50
r_{WNM}	kpc	0.67
r_{CNM}	kpc	0.33
N_{HIpeak}	cm^{-2}	5.10×10^{19}
M_{HI}	M_{\odot}	2.81×10^5
\mathcal{W}/\mathcal{T}		1.0
P_0/P_{HIM}		4.7
$n_{\text{H},0}$	cm^{-3}	2.08×10^{-2}

Table 4. CHVC extragalactic Model: -4σ Burkert halo

Halo Parameters		
x_{vir}		8.1
M_{vir}	M_{\odot}	3.2×10^8
r_{vir}	kpc	17.7
n_{ds}	amu cm^{-3}	7.0×10^{-2}
r_s	kpc	2.17
v_s	km s^{-1}	12.1
M_{ds}	M_{\odot}	7.43×10^7
r_{gas} (small- x)	kpc	2.1
Gas Input Parameters		
P_{HIM}/k	$\text{cm}^{-3} \text{ K}$	20.0
M_{WM}	M_{\odot}	7.1×10^7
$M_{\text{WM}}/M_{\text{vir}}$		0.22
Gas Output Parameters		
$r_{\text{W/H}}$	kpc	7.15
r_{gas} (numerical)	kpc	3.07
r_{NHI}	kpc	2.63
r_{WNM}	kpc	3.40
$r_{\text{WNM/CNM}}$	kpc	1.16
N_{HIpeak}	cm^{-2}	9.99×10^{19}
M_{HI}	M_{\odot}	1.44×10^7
\mathcal{W}/\mathcal{T}		1.0
P_0/P_{HIM}		4.4
$n_{\text{H},0}$	cm^{-3}	7.65×10^{-3}

Table 5: Halo Profiles

NFW
$f_\rho = \frac{1}{x(1+x)^2}$
$f_M = 3 \left[\ln(1+x) - \frac{x}{1+x} \right]$
$f_\varphi = 3 \left[1 - \frac{\ln(1+x)}{x} \right]$
$f_{\text{gas}} = e^{-3(v_s/c_g)^2} (1+x)^{(v_s/c_g)^2/x}$
Burkert
$f_\rho = \frac{1}{(1+x)(1+x^2)}$
$f_M = \frac{3}{2} \left[\frac{\ln(1+x^2)}{2} + \ln(1+x) - \tan^{-1}x \right]$
$f_\varphi = \frac{3}{2} \left\{ \tan^{-1}x \left(1 + \frac{1}{x}\right) - [\ln(1+x)] \left(1 + \frac{1}{x}\right) + \frac{1}{2} [\ln(1+x^2)] \left(1 - \frac{1}{x}\right) \right\}$
$f_{\text{gas}} = \left[e^{-(1+1/x)\tan^{-1}x} (1+x)^{(1+1/x)} (1+x^2)^{(1/2)(1/x-1)} \right]^{(3/2)(v_s/c_g)^2}$

Table 6: Small- x Formulae

NFW	Burkert
$f_{\text{gas}} = \exp\left(-\frac{3}{2} \frac{v_s^2}{c_g^2} x\right)$	$f_{\text{gas}} = \exp\left(-\frac{1}{2} \frac{v_s^2}{c_g^2} x^2\right)$
$x_{\text{gas}} \equiv \frac{r_{\text{gas}}}{r_s} = \frac{2}{3} \frac{c_g^2}{v_s^2}$	$x_{\text{gas}} \equiv \sqrt{2} \frac{c_g}{v_s} = \frac{r_{\text{gas}}}{r_s}$
$r_{\text{gas}} = \frac{2}{3} \frac{c_g^2}{v_s^2} r_s = \frac{c_g^2}{2\pi G m_{\text{H}} n_{d_s} r_s}$	$r_{\text{gas}} = \sqrt{2} c_g \frac{r_s}{v_s} = \left[\frac{3c_g^2}{2\pi G m_{\text{H}} n_{d_s}}\right]^{1/2}$
$r_{\text{gas}} = 0.19 \times 10^{-0.186\sigma} c_{g6}^2 v_{s6}^{-0.681} \text{ kpc}$	$r_{\text{gas}} = 0.41 \times 10^{-0.186\sigma} c_{g6} v_{s6}^{0.319} \text{ kpc}$
$r_{\text{gas}} = 0.17 \times 10^{-0.210\sigma} c_{g6}^2 M_{\text{vir},8}^{-0.213} \text{ kpc}$	$r_{\text{gas}} = 0.44 \times 10^{-0.175\sigma} c_{g6} M_{\text{vir},8}^{0.100} \text{ kpc}$
$M_{\text{WM}} = 4\pi n_{\text{H},0} m_{\text{H}} r_{\text{gas}}^3 \int_0^\infty y^2 e^{-y} dy = 8\pi n_{\text{H},0} m_{\text{H}} r_{\text{gas}}^3$	$M_{\text{WM}} = 4\pi n_{\text{H},0} m_{\text{H}} r_{\text{gas}}^3 \int_0^\infty y^2 e^{-y^2} dy = \pi^{3/2} n_{\text{H},0} m_{\text{H}} r_{\text{gas}}^3$
$N_{\text{WM}}(b) = 2n_{\text{H},0} r_{\text{gas}} \int_0^\infty e^{-\sqrt{(b^2+y^2)}} dy = 2n_{\text{H},0} r_{\text{gas}} b K_1(b)$	$N_{\text{WM}}(b) = 2n_{\text{H},0} r_{\text{gas}} \int_0^\infty e^{-(b^2+y^2)} dy = 2n_{\text{H},0} r_{\text{gas}} e^{-b^2}$
$N_{\text{WM,peak}} = N(0) = 2n_{\text{H},0} r_{\text{gas}}$	$N_{\text{WM,peak}} = N(0) = \sqrt{\pi} n_{\text{H},0} r_{\text{gas}}$
$EM = 2n_{\text{H},0}^2 r_{\text{gas}} \int_0^\infty e^{-2y} dy = n_{\text{H},0}^2 r_{\text{gas}}$	$EM = 2n_{\text{H},0}^2 r_{\text{gas}} \int_0^\infty e^{-2y^2} dy = \sqrt{\frac{\pi}{2}} n_{\text{H},0}^2 r_{\text{gas}}$
$n_{\text{H},0\text{crit}} = 9.06 \times 10^{-3} \times 10^{0.093\sigma} J_3^{*1/2} c_{g6}^{-1} v_{s6}^{0.341} \text{ cm}^{-3}$	$n_{\text{H},0\text{crit}} = 5.51 \times 10^{-3} \times 10^{0.093\sigma} J_3^{*1/2} c_{g6}^{-1/2} v_{s6}^{-0.156} \text{ cm}^{-3}$
$n_{\text{H},0\text{crit}} = 9.58 \times 10^{-3} \times 10^{0.105\sigma} J_3^{*1/2} c_{g6}^{-1} M_{\text{vir},8}^{0.105} \text{ cm}^{-3}$	$n_{\text{H},0\text{crit}} = 5.32^{-3} \times 10^{0.088\sigma} J_3^{*1/2} c_{g6}^{-1/2} M_{\text{vir},8}^{-0.050} \text{ cm}^{-3}$

Note. — In these expressions, v_s , r_s , and n_{d_s} are the halo scale parameters (see §2.1), and c_g is the gas sound speed. $v_{s6} = v_s/10 \text{ km s}^{-1}$, $c_{g6} = c_g/10 \text{ km s}^{-1}$, $M_{\text{vir},8} = M_{\text{vir}}/10^8 M_\odot$, and $J_3^* = J^*/10^3 \text{ photons cm}^{-2} \text{ s}^{-1} \text{ sr}^{-1}$. K_1 is the first order modified Bessel function.